UNIVERSITY OF OKLAHOMA GRADUATE COLLEGE

PULSED LASER DEPOSITION AND CHARACTERIZATION OF LANTHANUM-DOPED CALCIUM STANNATE EPITAXIAL THIN FILMS FOR ULTRA-WIDE BANDGAP OXIDE SEMICONDUCTOR APPLICATIONS

A THESIS

SUBMITTED TO THE GRADUATE FACULTY

in partial fulfillment of the requirements for the

Degree of

MASTER OF SCIENCE

By SEN SEYMOUR

Norman, Oklahoma

2025

Downloaded from SHAREOK. Persistent Handle URL: https://hdl.handle.net/11244/341222

PULSED LASER DEPOSITION AND CHARACTERIZATION OF LANTHANUM-DOPED CALCIUM STANNATE EPITAXIAL THIN FILMS FOR ULTRA-WIDE BANDGAP OXIDE SEMICONDUCTOR APPLICATIONS

A THESIS APPROVED FOR THE
SCHOOL OF ELECTRICAL AND COMPUTER ENGINEERING

BY THE COMMITTEE CONSISTING OF

Dr. Hanjong Paik, Chair

Dr. Zhisheng Shi

Dr. Thirumalai Venkatesan

© Copyright by SEN SEYMOUR 2025
All Rights Reserved.

Acknowledgements

First and foremost, I would like to give my profound thanks to my advisor, Dr. Hanjong Paik for being my mentor and supporter throughout this process. His patience with me in learning this deep subject is greatly appreciated, and I cannot thank him enough for this wonderful opportunity to learn even more about the nature of our world.

I would also like to thank Dr. Zhisheng Shi and Dr. Thirumalai Venkatesan for serving on my thesis committee. You have my deepest thanks in your guidance in both the subjects of semiconductors and material science, whether it was through class or in passing discussion.

There were many instruments to work with during this thesis, and some of the results could not have been achieved without the help of Dr. Hanping Ding's lab for their use of their high-temperature furnace, and Dr. Bayram Saparov's lab for allowing me to use their UV-vis spectrometer. Additionally, a special thank you to Dr. Andy Madden and Dr. Preston Larson at the Samuel Roberts Noble Microscopy Lab. The kindness and help you've supplied for the use of the x-ray diffractometer cannot be emphasized enough. To you all, your assistance and kindness have not gone unnoticed.

I would like to thank Dr. Sumit Goswami, Dr. Pralay Paul, Sreehari Puthan Purayil, Dhiman Biswas, Casey Kerr, Benjamin Summers, and Sujoy Bhattacharjee for being wonderful friends and supporters in the PLD lab, as well as faithfully answering my questions about the research in general.

I cannot continue without mentioning my incredible partner, Adam Goldberg, for being there every step of the way in this monumental and extraordinary journey. His drive and work

ethic have inspired me throughout this entire process, and I cannot even begin to express the impact he has had on me as both a student and person.

Last, and certainly not least, thank you to my friends, loved ones, and family, for always being there for me when I needed it, and for providing me the opportunity to continue my education. I am eternally grateful, and I hope you find this story to be a testament to your hard work and a fitting milestone to our journey together.

Abstract

$CaSnO_3$ exists as an ultra-wide bandgap (UWBG) semiconductor with a bandgap of 4.1eV-4.4eV, which, when engineered correctly, can be advantageously used as a material for transparent thin film transistors (TFTs) or for high-power electronic applications. $CaSnO_3$ has been regarded as an "undopable" material, due to the challenges of incorporating dopants in its perovskite structure, and the complex mechanisms that can govern the doping behavior. While there have been improvements made regarding its thin film synthesis with molecular beam epitaxy (MBE), the literature for doped thin films of $CaSnO_3$ deposited by pulsed laser deposition (PLD) is limited and attempts to properly dope the compound have been unsuccessful. In this study, the ability to dope and grow epitaxial thin films via PLD is challenged by undertaking an extensive investigation of powder preparation routes, sintering methodologies, and thin film growth condition optimization. While no semiconducting behavior was apparent, multiple doping levels were examined, evaluating phase purity, structure deviation from bulk references, and dopant incorporation. Epitaxial thin films were deposited under varying background oxygen pressures and substrate temperatures to optimize crystalline quality. Analysis using x-ray diffraction demonstrated promise in the potential of PLD as a viable route for fabricating doped UWBG $CaSnO_3$.

Table of Contents

Acknowledgements ..... *iv*

Abstract ..... *vi*

List of Figures ..... *ix*

List of Tables ..... *xv*

Chapter 1: Introduction *1*

1.1 The Utility of Perovskites **1**

1.1.1 Comparison to Other UWBG Materials 4

1.2 Challenging a Doping Problem **5**

Chapter 2: Literature Survey *8*

2.1 Current Literature on $CaSnO_3$ **8**

2.2 PLD Parameter Survey **9**

2.3.1 Similar Stannate Systems 9

2.3.2 Other Oxide Material Systems 13

2.3 Powder Fabrication Analysis **13**

2.5.1 Fabricating Powders with Incorporated Dopants 14

2.5.2 Doping $BaSnO_3$ and $SrSnO_3$ 16

Chapter 3: Experiment *17*

3.1 Powder Synthesis **17**

3.1.1 Undoped $CaSnO_3$ Powder Preparation 17

3.1.2 8% La-doped $CaSnO_3$ Powder Preparation 18

3.1.3 Varied La-doped $CaSnO_3$ Powder Preparation 18

3.2 Pulsed Laser Deposition 19

3.3 Characterization - X-Ray Diffraction 24

3.4 Characterization – UV-Vis Spectroscopy 25

Chapter 4: Discussion 26

4.1 Optimized Parameters 26

4.2 Lattice Constant Mismatch and Crystalline Quality 29

4.3 Phase Field and Fluence 34

4.4 UV-vis Measurements 37

4.5 Powder Refinement 38

Chapter 5: Conclusion 42

List of Figures

Figure 1: A figure indicating the bandgaps of the various stannates: $BaSnO_3$, $SrSnO_3$, and $CaSnO_3$. The varying bandgaps give rise to the possible utility from combining these materials into heterostructure devices. This visual was derived from data taken from Refs. [14, 15] 4

Figure 2: Deposition parameters of Temperature vs. Pressure (top) and Fluence vs. Repetition Rate (bottom) for $SrSnO_3$. Data from Refs.[8, 12, 20-31] 10

Figure 3: Deposition parameters of temperature vs. pressure (top) and fluence vs. repetition rate (bottom) for $BaSnO_3$ grown in literature. Data from Refs.[32-69] 12

Figure 4: An illustration of the PLD chamber. 21

Figure 5: 2θ scan of $CaSnO_3$ film grown at 100mTorr at 850C, indicating epitaxial growth on $SrTiO_3$ (100) substrate. 27

Figure 6: Rocking curve scan of $CaSnO_3$ film (red) and $SrTiO_3$ substrate (blue) with FWHM, thickness, and orientation as insets. The $CaSnO_3$ film indicates relaxation back into orthorhombic phase, giving evidence of strained cubic growth when not relaxed. 27

Figure 7: Reciprocal space map (RSM) aligned to the (103) direction. The $SrTiO_3$ substrate can be seen as the bright spot in the middle, while the relaxed phases of $CaSnO_3$ can be seen both in the middle and bottom portions of the map. Estimated in-plane and out-of-plane lattice parameters were calculated to be 3.922 Å and 3.958 Å, respectively. 28

Figure 8: X-ray reflectivity plot of the 7,500 shot CaSnO3 film grown on SrTiO3. The estimated thickness is ~75 nm, which estimates the thicker films grown in this study to be ~300 nm. 29

Figure 9: Graphs of comparing the bulk pseudocubic lattice constant against the films grown in the study. Undoped films grown at 750°C (first three), then 850°C (last two) on LAO (top), doped

films at 750°C (first three) then 850°C (last three) on LAO (middle), and the series of three films grown on STO (bottom). 31

Figure 10: XRD plots comparing thin film of $CaSnO_3$ vs. bulk powder diffraction patterns. Showcased are the orthorhombic planes 110 and 220 of the bulk powder aligning with the undoped thin film planes on LAO (100mTorr @ 850C) of 100 and 200. 34

Figure 11: Fluence phase field of undoped growths of $CaSnO_3$. Growths taken place at 650°C would not form. Fluences between 1.55 – 2.4 J/cm^2 could grow films at 100 and 150 mTorr, but 200mTorr requires a higher fluence to grow. 35

Figure 12: Fluence phase field of doped growths of $CaSnO_3$. Growths taken place at 650°C would not form. Fluences between 1.88 – 2.53 J/cm^2 grew films. 36

Figure 13: Tauc plots showing estimated indirect bandgap for LAO and STO substrates (top) and estimated direct bandgap for CaSnO3 films grown at 100mTorr at 850C (bottom). 38

Figure 14: 8% La-$CaSnO_3$ powder diffraction pattern (red) overlayed with $La_2Sn_2O_7$ reference (blue), indicating impurity phase. 39

Figure 15: XRD diffraction patterns of the doping trials, with reference[88] $CaSnO_3$ powder (black), indicating that a shift has occurred in the various trials. Possible pyrochlore impurity phase is indicated by (*). 40

Figure 16: Zoomed in view on the 020 (leftmost), 112 (middle), 220 (rightmost) peaks of diffraction for the doping series. A trend can be seen within the trials, disregarding the reference (bottom line). However, interestingly, each of the series falls right of the reference, instead of the expected leftward shifting due to La-incorporation. This suggests that either the La dopant was not properly incorporated, or other phenomena are at work. 41

Figure A17: XRD 2θ plot of undoped CSO sample grown at 100mTorr and 650C on LAO. 59

Figure A18: XRD 2θ plot of undoped CSO sample grown at 150mTorr and 650C on LAO..... 59

Figure A19: XRD 2θ plot of undoped CSO sample grown at 200mTorr and 650C on LAO..... 60

Figure A20: XRD 2θ plot of undoped CSO sample grown at 100mTorr and 750C on LAO..... 60

Figure A21: ω rocking curve of substrate (top) and film (bottom) of undoped CSO sample grown at 100mTorr and 750C on LAO. $FWHM_{film} = 2.34°$ 61

Figure A22: XRD 2θ plot of undoped CSO sample grown at 150mTorr and 750C on LAO..... 62

Figure A23: ω rocking curve of substrate (top) and film (bottom) of undoped CSO sample grown at 150mTorr and 750C on LAO. $FWHM_{film} = 1.559°$ 63

Figure A24: XRD 2θ plot of undoped CSO sample grown at 200mTorr and 750C on LAO..... 63

Figure A25: ω rocking curve of substrate (top) and film (bottom) of undoped CSO sample grown at 200mTorr and 750C on LAO. $FWHM_{film} = 1.66°$ 64

Figure A26: XRD 2θ plot of undoped CSO sample grown at 100mTorr and 850C on LAO..... 65

Figure A27: ω rocking curve of substrate (top) and film (bottom) of undoped CSO sample grown at 100mTorr and 850C on LAO. $FWHM_{film} = 0.732°$ 66

Figure A28: XRD 2θ plot of undoped CSO sample grown at 150mTorr and 850C on LAO..... 66

Figure A29: ω rocking curve of substrate (top) and film (bottom) of undoped CSO sample grown at 150mTorr and 850C on LAO. $FWHM_{film} = 0.719°$ 67

Figure A30: XRD 2θ plot of undoped CSO sample grown at 200mTorr and 850C on LAO..... 68

Figure A31: XRD 2θ plot of undoped CSO sample grown at 200mTorr and 850C on LAO..... 68

Figure A32: XRD 2θ plot of doped CSO sample grown at 100mTorr and 650C on LAO..... 69

Figure A33: XRD 2θ plot of doped CSO sample grown at 150mTorr and 650C on LAO..... 69

Figure A34: XRD 2θ plot of doped CSO sample grown at 200mTorr and 650C on LAO..... 70

Figure A35: XRD 2θ plot of doped CSO sample grown at 100mTorr and 750C on LAO..... 70

Figure A36: ω rocking curve of substrate (top) and film (bottom) of doped CSO sample grown at 100mTorr and 750C on LAO. $FWHM_{film}$ = 1.904° 71

Figure A37: XRD 2θ plot of doped CSO sample grown at 150mTorr and 750C on LAO..... 72

Figure A38: ω rocking curve of substrate (top) and film (bottom) of doped CSO sample grown at 150mTorr and 750C on LAO. $FWHM_{film}$ = 0.698° 73

Figure A39: XRD 2θ plot of doped CSO sample grown at 200mTorr and 750C on LAO..... 73

Figure 40: XRD 2θ plot of doped CSO sample grown at 100mTorr and 850C on LAO. 74

Figure A41: ω rocking curve of substrate (top) and film (bottom) of doped CSO sample grown at 100mTorr and 850C on LAO. $FWHM_{film}$ = 0.538° 75

Figure A42: XRD 2θ plot of doped CSO sample grown at 150mTorr and 850C on LAO..... 75

Figure A43: XRD 2θ plot of doped CSO sample grown at 200mTorr and 850C on LAO..... 76

Figure A44: ω rocking curve of substrate (top) and film (bottom) of doped CSO sample grown at 200mTorr and 850C on LAO. $FWHM_{film}$ = 0.650° 77

Figure A45: XRD 2θ plot of undoped CSO sample grown at 200mTorr and 850C on LAO (unsuccessful). 78

Figure A46: XRD 2θ plot of doped CSO sample grown at 150mTorr and 850C on LAO..... 78

Figure A47: ω rocking curve of substrate (top) and film (bottom) of doped CSO sample grown at 150mTorr and 850C on LAO. $FWHM_{film}$ = 1.432° 79

Figure A48: XRD 2θ plot of doped CSO sample grown at 200mTorr and 750C on LAO..... 80

Figure A49: ω rocking curve of substrate (top) and film (bottom) of doped CSO sample grown at 200mTorr and 750C on LAO. $FWHM_{film}$ = 0.670° 81

Figure A50: XRD 2θ plot of undoped CSO sample grown at 100mTorr and 850C on STO. 81

Figure A51: ω rocking curve of substrate (top) and film (bottom) of doped CSO sample grown at 100mTorr and 850C on STO. $FWHM_{film}$ = 0.536° 82
Figure A52: XRD 2θ plot of doped CSO sample grown at 100mTorr and 850C on STO. 83
Figure A53: ω rocking curve of substrate (top) and film (bottom) of doped CSO sample grown at 100mTorr and 850C on STO. $FWHM_{film}$ = 2.628° 84
Figure A54: XRD 2θ plot of thin doped CSO sample grown at 100mTorr and 850C on STO. ... 84
Figure A55: ω rocking curve of substrate (top) and film (bottom) of thin doped CSO sample grown at 100mTorr and 850C on STO. $FWHM_{film}$ = 0.559° 85
Figure A56: Deposition parameters of pressure vs. temperature of the various oxide systems found in Refs. [89-184] 86
Figure A57: Deposition parameters of repetition rate vs. fluence of the various oxide systems found in Refs. [89-184] 87
Figure A58: Lattice parameter plotted against Nelson-Riley function for the undoped $CaSnO_3$ film grown on LAO, indicating a lattice parameter of 3.9635 Å. The bulk constant 3.9635 Å is shown as the dotted magenta line. 87
Figure A59: Lattice parameter plotted against Nelson-Riley function for the doped $CaSnO_3$ film grown on LAO, indicating a lattice parameter of 3.9594 Å. The bulk constant 3.9635 Å is shown as the dotted magenta line. 88
Figure A60: Lattice parameter plotted against Nelson-Riley function for the undoped $CaSnO_3$ film grown on STO, indicating a lattice parameter of 3.9578 Å. The bulk constant 3.9635 Å is shown as the dotted magenta line. 89

Figure A61: Lattice parameter plotted against Nelson-Riley function for the doped $CaSnO_3$ film grown on STO, indicating a lattice parameter of 3.9640 Å. The bulk constant 3.9635 Å is shown as the dotted magenta line. 90

List of Tables

Table 1: Table of constituent amounts of powder for subsequent powder experiment. 19

Table 2: Table of Deposition Parameters for $CaSnO_3$ and La-$CaSnO_3$ films. 22

Table 3: Table showcasing the 2θ values in which the 002 diffraction peak occurs for the CSO thin film, both doped and undoped on LAO and STO substrates. 33

Chapter 1: Introduction

1.1 The Utility of Perovskites

Transparent conducting devices are utilized in a large variety of today's technology. By utilizing transparent conducting oxides as materials, such as the popular indium-tin oxide (ITO), things such as displays, solar cells, and other opto-electronic devices have been created. However, indium is an increasingly expensive and rare resource, and other materials are being investigated to reproduce transparent devices. Indium supply amount is reported as parts per million, while barium and strontium are measured as tons, and calcium (e.g., from limestone) is readily abundant.[1] Finding material solutions to transparent devices has been an advancing frontier of material science, and in particular, perovskite oxides have been a promising candidate for such devices.

$CaRuO_3$ and $SrRuO_3$ are conducting oxides, exhibiting metallic behavior. Both have been studied for their unique properties, including $SrRuO_3$'s ferromagnetism,[2] and $CaRuO_3$'s metal-insulator transitions due to chemical substitutions.[3] Their use in heterostructures gives utility in condensed matter physics research, however, their metallic behavior limits their ability for carrier modulation. $YB_2C_3O_7$ (YBCO) is another perovskite oxide that is well known and utilized for extensive study with superconductivity, though, this focus has overshadowed experimentation in its utilization in industrial devices.

The perovskites of $SrTiO_3$ (STO) and $BaTiO_3$ (BTO) have also been extensively studied, with STO being a common substrate for pulsed laser deposition experiments today. STO has been refined for realizing lower defect concentrations, as well as investigating its unconventional

superconductivity, among other property enhancements.[4] BTO has been utilized mostly in semiconductor devices for ferroelectric memory and piezoelectric devices.[5]

$SrSnO_3$ (SSO) and $BaSnO_3$ (BSO) are two other materials that have been studied as ultra-wide bandgap semiconductors for use in electronic devices. These materials, like many others, are also the subject of doping experiments. Lanthanum doped SSO has been studied to improve carrier mobility, as well as be implemented in semiconductor devices like MESFETs.[6] Truttmann et al.[7] have made 12nm thin films of La-SSO with a room temperature mobility of 70 $cm^2 V^{-1} s^{-1}$ at 1E20 cm^{-3}. Changanti et al.[6] have made La-SSO based depletion-mode metal-semiconductor FET (MESFET), exhibiting a breakthrough in growing epitaxial films with doping control for use in devices. Recently, Seo et al.[8] have produced a thin film transistor (TFT) with La-SSO used as the gate, drain and source, and channel layers. This device exhibited an on/off ratio above 10^6, while having a mobility of 24 $cm^2 V^{-1} s^{-1}$.

BSO has been extensively studied, with thin film mobility being reported[9] as high as 183 $cm^2 V^{-1} s^{-1}$ for a carrier concentration $n = 1.2 \times 10^{20}$ cm^{-3}. Paik et al. have also reported mobilities between $n = 10^{18}$ to 3×10^{20} cm^{-3}, though, there is a drop-off in mobility at $n = 10^{18}$ cm^{-3}. There has also been transparent TFT devices fabricated with La-BSO as well, exhibiting a high on/off ratio of 1.5×10^8. The manipulation of these materials is paramount to continuing the development of next-generation devices, especially in the context of diminishing resources. However, these stannate systems have even more interesting outlooks when introducing a cousin system.

$CaSnO_3$ (CSO) is another perovskite oxide that has an even wider bandgap than BSO and SSO. CSO has an ultra-wide band gap (UWBG) of 4.2eV to 4.6eV, depending on strain states and dopant.[10, 11, 12] In comparison, SSO has a bandgap of around 3.7-4.1eV[13, 6, 8] and BSO is around 2.8eV-3.6eV.[14, 12] The pseudocubic lattice parameters of CSO and SSO are 3.95 Å and 4.04 Å,

respectively, which are both orthorhombic crystal structures.[14] In contrast, BSO adopts a cubic crystal structure, and has a larger lattice parameter of 4.12 Å. Despite these structural differences, these materials are viable candidates for semiconductor devices, especially when placed in the context of the formation of two-dimensional electron gas (2DEG) systems and modulation doping.

Considering their relatively wide bandgaps, they offer great thermal stability and enable robust electronic behavior. This behavior includes the suppression of thermally activated carriers, which serves to be advantageous for controlling the carrier concentration in device channels, as well as reducing off-state leakage during operation. While wide bandgaps can support insulative behavior for certain use cases like gate dielectrics or barriers, these oxide perovskites can exhibit n-type conductivity with appropriate doping or defect engineering, making them suitable for active layers in oxide-based field-effect transistors. Regarding heterostructures, the band alignment between these different oxides can be engineered to produce conduction band offsets conducive to the formation of a 2DEG. Such a configuration opens new gateways to exploring modulation doping strategies, which can assist in spatially separating mobile electrons from ionized dopants, significantly reducing scattering effects and enabling higher mobilities to be realized. These attributes make CSO, SSO, and BSO promising candidates for integration within oxide heterostructures which are designed for transparent, high-performance, and ultra-wide bandgap (UWBG) electronics.

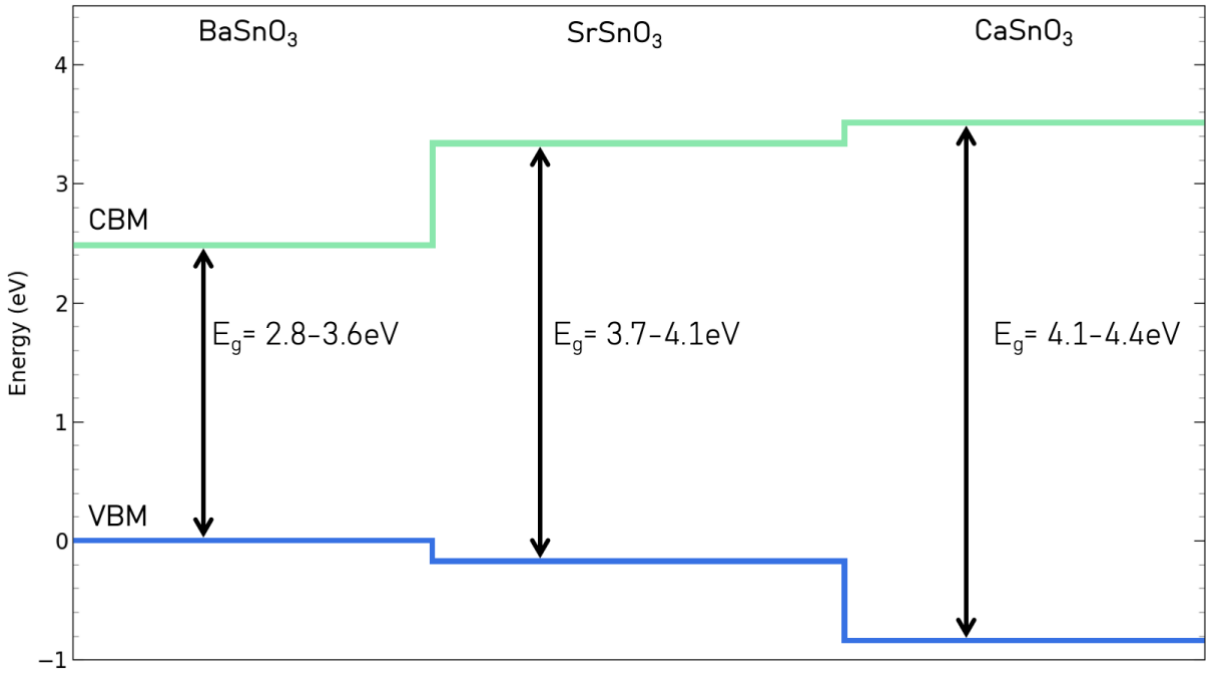

Figure 1: A figure indicating the bandgaps of the various stannates: $BaSnO_3$, $SrSnO_3$, and $CaSnO_3$. The varying bandgaps give rise to the possible utility from combining these materials into heterostructure devices. This visual was derived from data taken from Refs. [14, 15]

1.1.1 Comparison to Other UWBG Materials

There are other materials that are leading the field, such as gallium nitride (GaN) and silicon carbide (SiC), which exhibit bandgaps of ~3.4eV and ~3.2eV, respectively.[15, 16] GaN is widely used for its optoelectronic properties in LEDs and high-frequency devices, while SiC is used in high-power applications in electric vehicles. Gallium oxide (Ga_2O_3) is also an emerging UWBG semiconductor with a bandgap of 4.5eV – 4.9eV, however, its thermal conductivity is low and poses a challenge in engineering reliable high-power devices.[17] The motivation of enhancing $CaSnO_3$ lies in addressing these deficiencies with the aforementioned material systems. $CaSnO_3$ has a wider bandgap than GaN and SiC, which, if promoted to a semiconductor, could enhance its utility in high-power applications. Its oxide structure gives it stability and helps maintain its phase under high pressures and temperatures, making it a desirable material to use in intense environments. There is evidence suggesting it being a direct bandgap material,[11] which could open

the avenues for optoelectronic devices in the future. Its thermal conductivity may pose as another challenge, but the incorporation of heatsinks and other materials with higher thermal conductivities can supplement this to join Ga_2O_3 in creating new devices. Lastly, $CaSnO_3$ is transparent, which opens opportunities for applications in solar panels, transparent electronics, and thin film transistors.

Despite the advantageous wide bandgap and similarity to the other stannates, CSO has been proven difficult to dope effectively, especially when considering deposition techniques like pulsed laser deposition (PLD). While molecular beam epitaxy (MBE) has demonstrated the successful incorporation of dopants such as La^{3+}, which has broken a previous notion of it being "impossible" to dope,[14] this level of control has not yet been translated to PLD-grown films. This work challenges the viability of CSO as a functional semiconductor, focusing on its ability to be extrinsically doped through its powder form, and exhibit measurable electronic properties when synthesized by PLD. By introducing La as an aliovalent dopant on the Ca site, the goal is to evaluate whether CSO can be driven to a conductive regime using an accessible, scalable growth method. This approach not only tests the flexibility of CSO within its broader family of perovskite stannates, but also pushes against the current boundaries of what has been demonstrated in the literature. If successful, CSO can not only be used in heterostructures with BSO and SSO but can also find advanced application within ultraviolet (UV) detection, TFTs, and high-voltage operation for power electronics. The following sections reviews the existing body of work on CSO, with particular attention to its doping mechanisms, growth parameters, and transport properties.

1.2 Challenging a Doping Problem

The potential of $CaSnO_3$ (CSO) as a wide-bandgap semiconductor is clear, particularly due to its perovskite structure which can be engineered in a variety of ways, and its electronic

configuration dominated by Sn 5s orbitals, which contribute to a low effective mass, enhancing carrier movement. However, while such properties make these stannates appealing, n-type doping of CSO has proven significantly more difficult than its counterparts BSO and SSO.

Calculations by Weston et al.[14] provide further insights into the inherent doping behaviors among stannates. They show that La^{3+} dopants intended to occupy the A-site (Ca^{2+} and Sr^{2+}) are often compensated by native acceptor-type defects such as cation vacancies in orthorhombic systems such as SSO and CSO. In contrast, BSO has a higher symmetry cubic structure, which exhibits less severe compensation, making it more readily doped. This behavior is closely tied with the formation energies of the intrinsic defects, which can vary with both symmetry and growth conditions, especially chemical potentials during thin film deposition.

Weston et al. further explores how the chemical environment of the system affects the dopant incorporation. In oxygen poor conditions, formation of the La_{Ca}-type defects (La incorporated at the Ca site) becomes more favorable for CSO. Though, even under these conditions, their calculated concentrations of these defects remain lower for CSO compared to BSO or SSO for their A-site defect counterparts. Moreover, they indicate that achieving substantial La incorporation requires exceedingly Sn-rich and oxygen-poor growth environments – where being Sn-rich can be difficult to control in the powder fabrication process. The growth conditions of Paik et al.'s La-BSO exhibit an exploitation of these environmental parameters.[9] A-site vacancies are also found to have a lower formation energy in oxygen-rich environments, further reducing the likelihood of La incorporation at the Ca site. This is due to the compensating nature of the vacancy.

Weston et al.'s findings underscore that properly incorporating n-type dopants in CSO is not just a matter of choosing the right dopant but is a complex thermodynamic and kinetic problem

influenced by crystal structure, defect chemistry, and precise control of the growth environment.[14] These insights frame the core question of this work: Can thin films of La-doped CSO be epitaxially grown for UWBG semiconductor applications via pulsed laser deposition? By revisiting this doping challenge and optimizing the growth parameters of the thin films, this study aims to spearhead whether CSO can be grown epitaxially while overcoming its doping limitations.

Chapter 2: Literature Survey

2.1 Current Literature on $CaSnO_3$

The literature available for $CaSnO_3$ thin films at the time of writing this paper was limited. There were efforts to grow CSO by PLD, though, no enhanced electrical characteristics were realized. Liu et al. investigated structural and optical properties, where they grew CSO films at 780C with a background pressure of 225mTorr on an LAO substrate. Their target was sintered at a final temperature of 1580°C, with constituent compounds CaO and SnO_2.[15] Another study grew 3% La-doped CSO on LAO, but their film was also insulative.[12] This film was grown at 750°C at 150mTorr, with a fluence of 2 J/cm^2 and a repetition rate of 10Hz.

A $CaSnO_3$ thin film was fabricated by hybrid molecular beam epitaxy (hMBE) while successfully incorporating lanthanum as a dopant.[11] They had recorded a room-temperature mobility of 42 cm^2 V^{-1} s^{-1} with a 3D carrier concentration of n = 3.3 x 10^{19}cm^{-3}. Though not PLD parameters, their substrate temperature was set to 950°C, and their oxygen background pressure was 5E-6 Torr. The report suggested a doping limit of around 1.6E20 cm^{-3} for CSO, in which anything above that will begin to form the pyrochlore $La_2Sn_2O_7$. They had also reported an undoped direct band gap of 4.64eV, while the doped direct band gap was 6.68eV. They had expressed that the use of LAO as a substrate and the nature of PLD makes it difficult to grow an n-doped CSO film that has minimal defects.

Another study investigated the optical, electrical, and physical properties of CSO fabricated by a spin-coating method.[10] This study utilized CSO nanoparticles and fabricated a p-i-n photodiode to investigate how CSO can be used as a deep ultraviolet (DUV) photodetector. Their resulting device exhibited fast response times and a detectivity of 1.56E10 Jones. Additionally,

there are, of course, other papers investigating CSO in other ways other than thin films but are considered out of scope for this study.

2.2 PLD Parameter Survey

2.3.1 Similar Stannate Systems

An extensive survey of similar stannate systems grown by PLD, namely $SrSnO_3$ (SRO) and $BaSnO_3$ (BSO), was conducted to determine the best parameters to grow at for $CaSnO_3$. For SSO, there were no reported growths over 800°C for what was readily available at the time. The highest deposition temperature found was 790°C,[12] and the lowest was 600°C.[15] The highest deposition pressure reported was 225 mTorr[16, 17, 18] and the lowest was 0.015 mTorr.[19, 20] The fluence was varied between 1.3 J/cm^2 to 2.5 J/cm^2, however, it should be noted that some papers did not include this value, but the energy at which the laser was shot (e.g. 200mJ per pulse).[21, 22] These per pulse values were not plotted. When repetition rate was mentioned, the values indicated were 2, 3, 4, 5, or 10Hz. The substrates that spanned these papers were R-sapphire, LAO, STO, MgO, and $NdScO_3$. The dopants that spanned these papers were lanthanum, niobium, antimony, cobalt, lead, and vanadium. Shown below is a figure of the various parameters that were used for the SSO depositions. The values shown were filtered from what the reports indicated were the optimal values, which, for example, explains why 600°C is not seen in the plot.

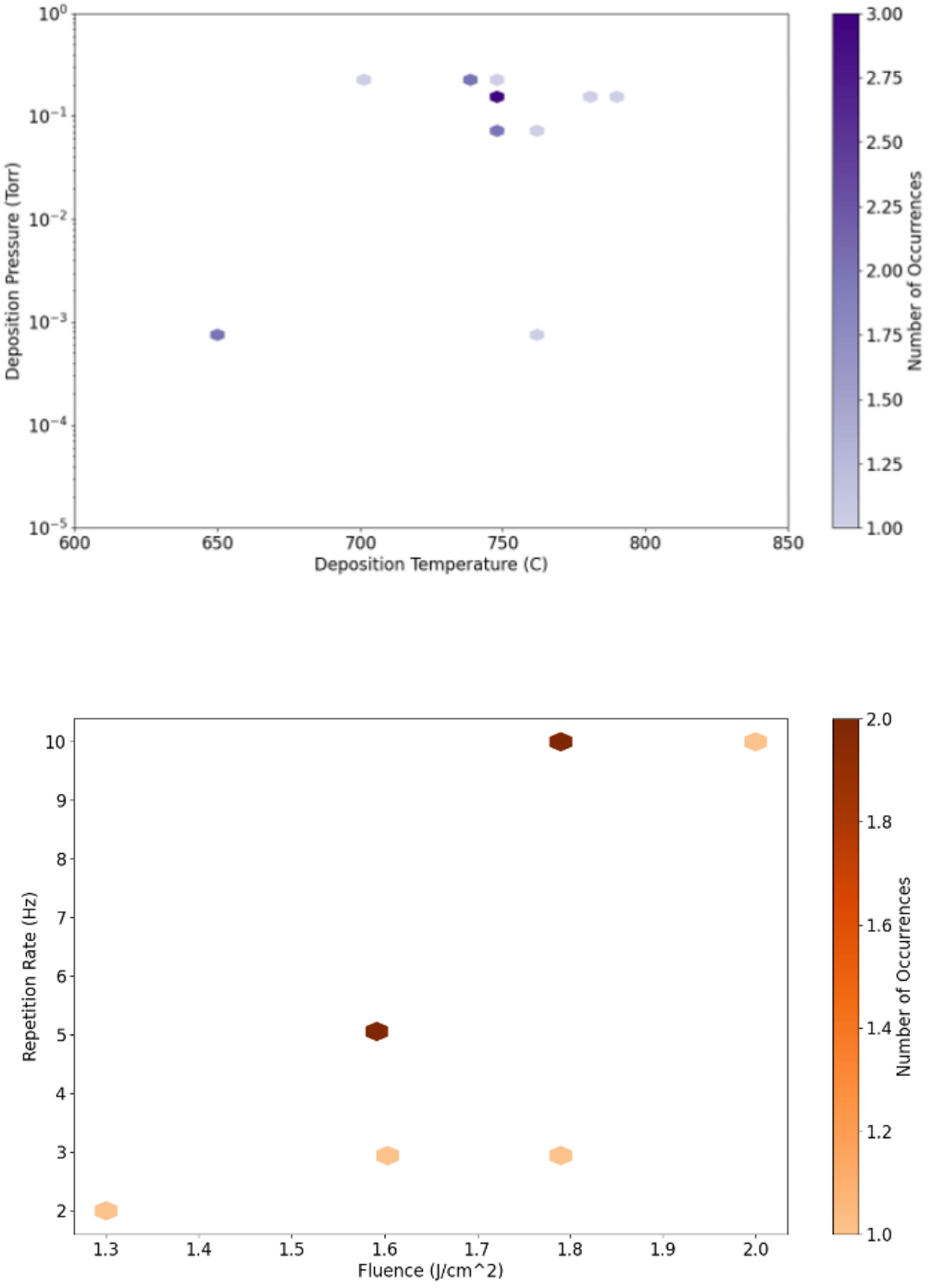

Figure 2: Deposition parameters of Temperature vs. Pressure (top) and Fluence vs. Repetition Rate (bottom) for $SrSnO_3$. Data from Refs.[8, 12, 20-31]

The most common deposition temperature and pressure for the SSO systems was 750°C at 150mTorr, with the temperature staying relatively in the range between 700°C and 790°C. Despite the low sample count for the group, 1.6 J/cm^2 and 1.8 J/cm^2 were the common fluences, while the repetition rates 5 or 10Hz were favored.

More references for the BSO system were found in comparison to SSO. The highest deposition temperature was 850°C.[28, 29, 30, 31, 32] The lowest was at room temperature (~20°C) as an outlier,[33] but 600°C was the next highest from that.[34, 35, 36] For pressure, 30 Torr was the highest,[37] while 0.375 mTorr was the lowest.[38] 0.3 J/cm^2 was the lowest reported fluence,[29] while 2.7 J/cm^2 was the highest reported.[37] Various dopants were also incorporated across these studies, which included La, Gd, Pr, Nd, Fe, Co, Ni, Sr, Ti, and Hf. Shown below are graphs indicating what deposition parameters were used for the BSO system, which were again filtered to only include optimal values listed.

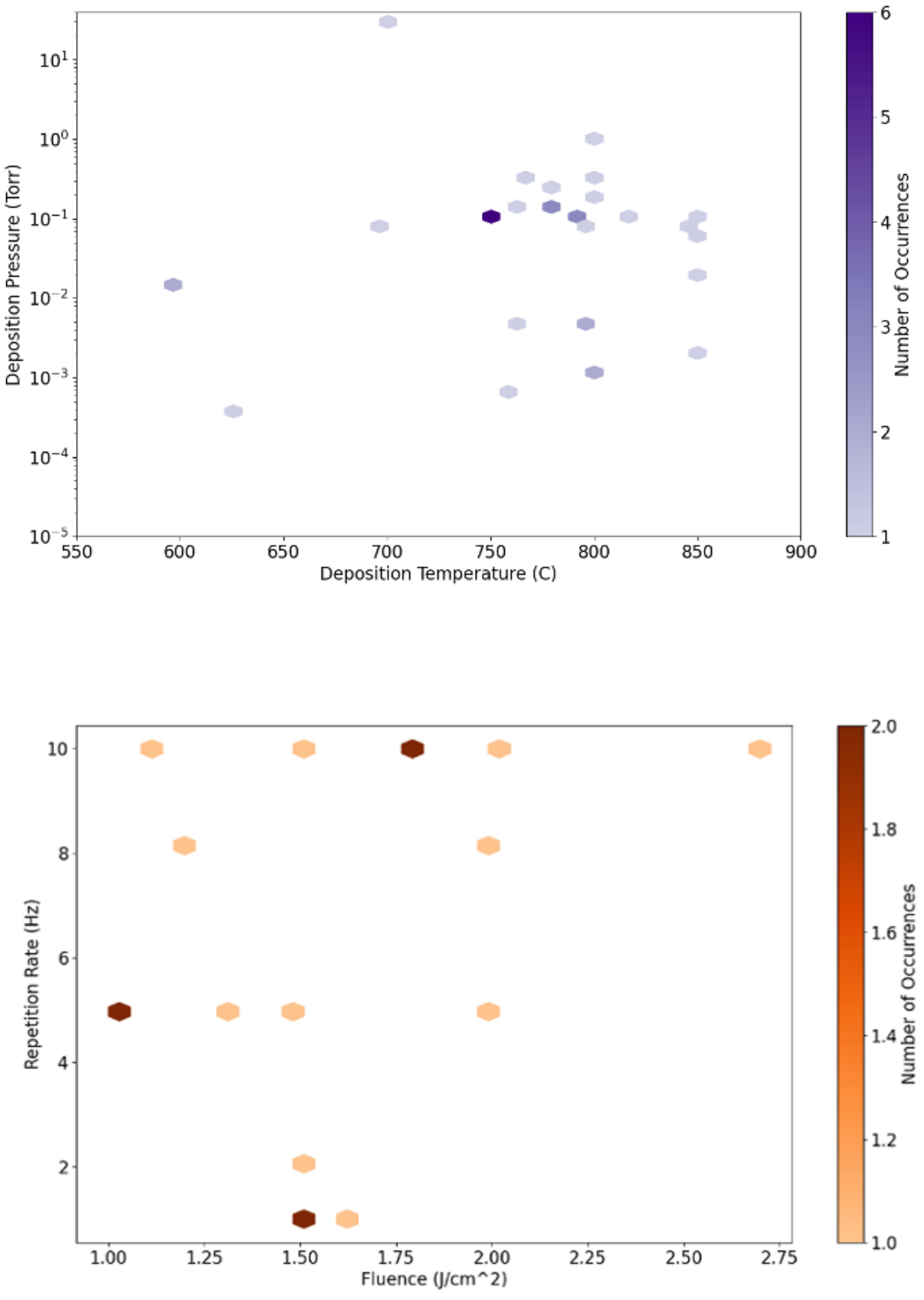

Figure 3: Deposition parameters of temperature vs. pressure (top) and fluence vs. repetition rate (bottom) for $BaSnO_3$ grown in literature. Data from Refs.[32-69]

For BSO, the common deposition temperature and pressure was 750°C at 100mTorr. Some depositions were done at 600°C, though, the main spread was concentrated between 750C and 850°C. By visual inspection, both stannate systems trend in the same areas for temperature and pressure, showcasing intensified patterns near 750°C and areas around the 100mTorr range. For fluence, the values were particularly spread out, and instead of looking at the number of occurrences, it is worthy to analyze across the axes. Fluences were more focused around 1.5 and 2 J/cm^2. Repetition rates were more concentrated at 1, 5, and 10Hz.

2.3.2 Other Oxide Material Systems

During the course of this study, several other oxide systems were studied to determine the general regime of parameters that generates epitaxial film growth. There was a generalist survey based off oxide films mostly grown on STO. There were additional surveys on the growth of $BaTiO_3$ (BTO) and $YBa_2Cu_3O_7$ (YBCO). The same parameters as the stannates were recorded, and figures of these trends can be found in the supplementary material.

2.3 Powder Fabrication Analysis

Various methods of powder fabrication are available to pursue. Some of these methods pertain to optimizing the use case of the resulting powder, such as creating nanoparticles or solutions. These methods can be a polymeric precursor method, sol-gel method, or a solid-state reaction, among others.[70, 71, 72] In this study, the solid-state reaction route is used. The following section discusses how other experiments in the field have taken the same approach, and how this study has utilized and modified this approach to prepare $CaSnO_3$ PLD targets.

For both convenience and consistency with the PLD literature, the solid-state reaction route was taken. The polymeric precursor method utilizes different of various reagents and precursor salts involved in various heating and chemical reactions.[72] The sol gel method utilizes the process

of hydrolysis and the mixing of metal precursors and salts within a solution, creating a gel of the target material which can be subsequently dried into a powder or thin film.[73] The solid-state reaction route is another approach that typically incorporates compounds that, when heated to a high enough temperature, react and form the targeted compound as a product. This approach usually starts with the dry powder of the reactants, which are then pulverized and mixed in a mortar or ball mill to create a fine powder. This powder is then transferred to a furnace which can calcinate the powder to begin forming the target compound, then subsequently sintered to increase grain sizes and bonding without melting the subsequent material. This method was chosen due to its reproducibility, available materials and equipment, and convenience.

The solid-state reaction route was performed with strategies taken from several other methods in the literature. Various sources used a combination of precursor powders for the starting mixture. These included $CaCO_3$,[74] CaC_2O_4,[75] $Ca(NO_3)_2$,[76] and SnO_2.[74, 75, 76, 77] Karabulut et al. reported that for a calcination temperature between 900°C and 1000°C, Ca_2SnO_4 will form, but not $CaSnO_3$.[77] Goto found that $CaSnO_3$ would form after 1000°C, but with secondary phases.[78] Karabulut also found that the mixture of $CaCO_3$ and SnO_2 will react continuously at 1100°C to form $CaSnO_3$, and that the orthorhombic structure appears after being sintered at 1200°C for 2 hours.[77] Several authors reported sintering at higher temperatures set at 1350°C,[76] 1400°C,[78] and 1550°C.[74] In this study, a calcination temperature of 1100°C was chosen, while the sintering temperature for the undoped powder was 1300°C, and the doped powder was 1450°C to account for the incorporation of the lanthanum dopant.

2.5.1 Fabricating Powders with Incorporated Dopants

Using the solid-state reaction method, incorporating dopants into the product typically means introducing another reactant compound into the mixture. For example, Goto had used

$MgCO_3$, Pr_6O_{11}, and Tb_4O_7 to dope their samples of $CaSnO_3$. They had made nominal compositions of $(Ca_{1-x}Pr_x)SnO_3$ and $\{Ca_{1-z}Mg_z)_{1-y}Tb_y\}SnO_3$ (x, y, z = 0.0 ~ 0.1) by effectively mixing the additional precursors into the mortar with ethanol, pressing them into disks, and were heated between 1000°C ~ 1400°C.[78] Though, they had only acquired single phases of doped $CaSnO_3$ when x = 0.0~0.1, y = 0.0~0.005, and z = 0.0~0.03. Takani synthesized single phase $CaTi_{1-x}Sn_xO_3$ (x = 0.0-1.0) for all samples using TiO_2 as the additional precursor, with a calcination temperature of 1200°C and sintering temperature of 1450°C, both held at their final temperature for 12 hours.[79]

Goethals et al. were able to dope $CaSnO_3$ to an extreme with neodymium, being able to dope up to 38 molar % concentration without detecting any secondary phase by x-ray diffraction (XRD) or by electron microprobe (EMPA).[74] Their synthesis process of $(1-x)CaSnO_3$-xNd_2O_3 was unique, and the steps were two-fold: the synthesis of pure $CaSnO_3$, then the incorporation of the Nd dopant. In comparison, the earlier studies mentioned[78, 79] combined all precursors together at the very beginning of the process, without making $CaSnO_3$ first. Goethals et al. made pure $CaSnO_3$ by mixing $CaCO_3$ and SnO_2 in a mortar with a pestle, calcinating it at 900°C for 2 hours, then sintering it at 1300°C for 24 hours, where they then reground the sintered powder and repeated the same heating profile. The precursor Nd_2O_3 was used to dope the compound of $CaSnO_3$. However, before incorporating the dopant, they had hydrated the Nd_2O_3 powder, making it into $Nd(OH)_3$. They then mixed the $Nd(OH)_3$ with the pure $CaSnO_3$, and sintered the mixture at 1550C for 24 hours, reground, then sintered at 1550°C again for 72 hours.[74]

The results of the XRD diffraction data showcase that these samples, where x=0.0-0.56, had successfully incorporated the Nd dopant, as the diffraction peaks shifted to lower 2θ values as x increased. Though there were some impurity phases, they had curiously been located at the lower

doped values of x = 0.04, 0.04, and 0.19. At higher dopant levels where x = 0.23, 0.28, and 0.33, the dopant was successfully incorporated, and no impurity phase was detected.[74] The significance of this is that they had first hydrated the Nd_2O_3, which could lead to more homogeneity during the mixing step at room temperature and allow for more finer particles of Nd to help substitute the calcium sites.

2.5.2 Doping $BaSnO_3$ and $SrSnO_3$

To gather a better introspection to the problem of doping $CaSnO_3$, similar PLD experiments were analyzed with the stannate systems, $BaSnO_3$ (BSO) and $SrSnO_3$ (SSO). For lanthanum doped BSO, one study had synthesized $(La_xBa_{1-x})SnO_3$ targets via solid-state reaction (x = 0, 0.02, 0.05, 0.07, 0.10, 0.15, 0.20) by mixing $BaCO_3$, SnO_2, and La_2O_3 as precursors. They had a final sintering temperature of 1450°C held for 24 hours and were able to successfully incorporate the dopants into the thin films.[56] Niedermeier et al. had also synthesized polycrystalline and 7 at. % La:BSO targets using the same precursors, though, there was a secondary phase of the pyrochlore $La_2Sn_2O_7$. Despite this, a nanocrystalline thin film was deposited with seemingly no impurity phase.[37]

For SSO, Liu et al. synthesized ceramic targets of $Sr(Sb_xSn_{1-x})O_3$ (x = 0.0-0.15) and $(Nd_xSr_{1-x})SnO_3$ (NSSO) (x = 0.0-0.10) via solid-state reaction with the precursors $SrCO_3$, SnO_2, Sb_2O_3, and Nd_2O_3.[29] Their final sintering temperature was 1550°C and was held for 24 hours. For the NSSO films, the films grew epitaxially with no secondary phases and changes in lattice parameter for x = 0.0-0.15. These experiments served as guiding factors in how the present study carried out the fabrication procedures of doping $CaSnO_3$ with lanthanum as an n-type dopant.

Chapter 3: Experiment

3.1 Powder Synthesis

Two targets of undoped and 8% La-doped $CaSnO_3$ were fabricated via the solid-state reaction route. To create these targets, undoped and doped $CaSnO_3$ powders were first synthesized using pestle and mortar with molar amounts of $CaCO_3$ (Alfa Aesar, 99.999%), SnO_2 (Thermo Fisher Scientific, 99.996%), and La_2O_3 (Sigma-Aldrich, 99.99%) powders as precursors. Each powder was weighed in an EQ-Bal-CX220-LD Professional Grade Digital Balance (MTI Corporation, readability 0.1mg, linearity ± 0.2mg) to synthesize a total of 9 grams of final powder.

3.1.1 Undoped $CaSnO_3$ Powder Preparation

The undoped powder was prepared by mixing $CaCO_3$ and SnO_2 in a pestle and mortar for 2 hours using acetone as a grinding medium to ensure a homogeneous mixture. After drying for 1 hour, the powder was pressed into a 25.4 mm pellet at 30MPa using a manual die set (MSE Supplies LLC). The pellet was then calcined in a Lindberg/Blue M box furnace: the temperature was ramped at 100°C/hr to 800°C, then at 200°C/hr to 1100°C, held for 12 hours, and cooled to room temperature at 200°C/hr, following established calcination conditions for $CaSnO_3$.[77]

Post-calcination, the pellet was ground again for 30 minutes, with polyvinyl alcohol (PVA) added as a binder. The resulting powder was then re-pressed at 30MPa, then placed in a latex pouch and subsequently cold isostatically pressed at 200MPa in a Benchtop CIP (20,000 psi max, Pellet Press Die Sets). The final pellet was sintered in an alumina crucible using a Lindberg/MPH 54233 Tube Furnace with the following profile: 100°C/hr to 800°C (hold 2 hr), then 200°C/hr to 1300°C (hold 12 hr), and cooled at 200°C/hr to room temperature.

3.1.2 8% La-doped $CaSnO_3$ Powder Preparation

For the 8% doped powder, $CaCO_3$ (3.2383g), SnO_2 (5.302g), and La_2O_3 (0.4603g), were measured and combined in a pestle and mortar, then ground in an acetone medium for 2 hours. The same calcination profile from the undoped powder was used. Post-calcination, XRD revealed secondary phases. The pellet was ground again for 30 minutes, then suspended in isopropyl alcohol with and magnetically stirred for 20 hours. The mixture was dried on a hot plate for 7 ½ hours at ~90°C, re-pressed in the hand press at 30MPa, followed by cold isostatic pressing at 200MPa. Sintering was performed in a Lindberg/MPH tube furnace with a similar profile as the undoped powder, but instead the final temperature was raised to 1450°C and was held at this temperature for 24 hours. This powder still indicated impurity phases of the pyrochlore $La_2Sn_2O_7$.

3.1.3 Varied La-doped $CaSnO_3$ Powder Preparation

To optimize phase purity, subsequent powder experiments were performed at varying La doping concentrations. Unlike previous methods, these trials adopted a different approach as based on another reference.[74] Instead of mixing La_2O_3 powder immediately at the time of the initial powder preparation, pure $CaSnO_3$ powder was synthesized first, then mixed with varying amounts of La_2O_3 powder corresponding with nominal carrier concentrations of 1×10^{21}, 1×10^{20}, 1×10^{19}, and 1×10^{18} cm^{-3}, as shown in the table below.

Carrier Concentration (cm^{-3})	Amount of $CaSnO_3$ (grams)	Amount of La_2O_3 (grams)	Amount of Powder Total (grams)
1×10^{21}	0.7933	0.2075	1.0008
1×10^{20}	0.9806	0.0200	1.0006
1×10^{19}	0.9986	0.0020	1.0006
1×10^{18}	1.0003	0.0002	1.0005

Table 1: Table of constituent amounts of powder for subsequent powder experiment.

Molar amounts of $CaCO_3$ and SnO_2 were measured to yield ~5 grams of $CaSnO_3$ powder, reserving ~1 gram as a reference for XRD to determine phase-purity. The $CaSnO_3$ powder was fabricated via the solid-state reaction route, with both precursors preheated at 200°C for 1 hour to remove any moisture. Once the powders were dried, the same mixing, calcination, and sintering processes were followed from the previous powder experiments. Once sintered, the pellet was reground into a fine powder. Appropriate amounts of La_2O_3 corresponding to the nominal doping concentrations were mixed for 30 minutes with 5 drops of PVA to help bind the mixture. The mixture was pelletized at 30MPa, placed in a latex pouch, and pressed in the cold isostatic press at 200MPa. Final sintering was conducted at a temperature of 1600°C for 24 hours in an MTI Bench-Top Muffle Furnace (KSL-1700X-A1) operated by Dr. Hanping Ding's lab. Although the programmed temperature was 1550°C, it is estimated that the internal temperature was ~1600°C. The results of these trials are discussed in Section 4.5.

3.2 Pulsed Laser Deposition

Pulsed laser deposition is a growth technique similar to physical vapor deposition like sputtering or evaporation, though instead of heat or ion bombardment, a laser is utilized to ablate a target material to deposit onto a substrate. The method was pioneered by T. Venkatesan in 1987

during early studies of high-temperature superconductors like YBCO.[80] The advantages of this deposition technique are due to its ability to transfer the target material composition with high fidelity from target to substrate. This effectively relies on the target material to consist of the desired bulk stoichiometry, allowing the single-crystalline growth to ideally preserve the functional properties of the bulk phase. Additionally, the laser ablation process is critical to the benefits that PLD provides. With the nano-scale timeframe between pulses, the thermal and electron excitation of the target material is realized, which leads to the ejection of the material resulting in a plasma plume. This plasma plume carries the material species, ejecting both light and heavy ions, electrons, and clusters of the material towards the substrate. With this plume of negatively charged materials moving fastest, and the ions moving slower, this creates an electric field that effectively slingshots the heavier material with the lighter material, maintaining the stoichiometry in a more uniform manner.[81]

The desired material is usually in the form of a pellet, placed on a stage at the bottom of the chamber. This stage can rotate and raster forward and backward to allow the laser to ablate the surface uniformly. The laser comes in at an angle which hits the pellet of the target material, which then ablates the material in a vacuum or other background gas, allowing the material to travel to the substrate adhered to a substrate holder above the target. A figure of the apparatus can be seen below:

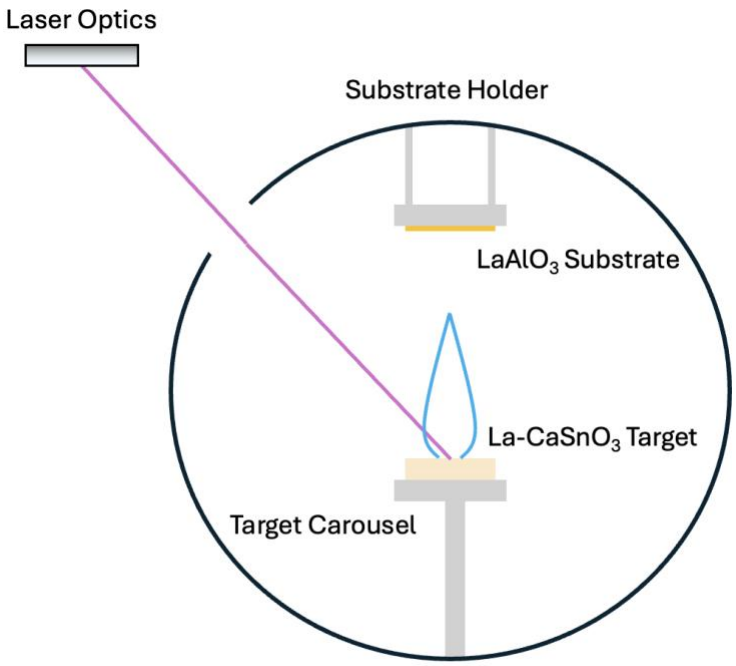

Figure 4: An illustration of the PLD chamber.

In this study, a krypton fluoride (KrF) excimer laser was used as the ablation source. An excimer laser effectively utilizes a noble gas (krypton) and a halogen gas (fluorine) to generate high-energy UV pulses from excited dimers ("excimers"). These excimers are effectively two atoms bonded together but cannot exist together in their ground state. Upon relaxation, the excimer emits UV radiation, and for KrF, the emission occurs at 248nm. This wavelength is particularly effective for PLD as it provides sufficient photon energy to break chemical bonds at the target surface, generating a stoichiometric and energetic ablation plume.

Thin films of undoped $CaSnO_3$ and 8% La-doped $CaSnO_3$ were deposited using pulsed laser deposition (PLD), with growth conditions optimized based on the literature study. Films were primarily grown on 5mm x 5mm x 0.5mm $LaAlO_3$ (100) (Commercial Crystal Laboratories and MTI) while later experiments used 3mm x 3mm x 1.0mm $SrTiO_3$ (100) substrates (Shinkosha), which were cut with a South Bay Technologies Model 850 diamond wire saw.

A Lambda Physik COMPex 205 KrF excimer laser ($\lambda = 248$nm) was used for laser ablation, operated between 16.8kV to 27kV. Various temperatures and pressures were used, while attempting to keep fluence constant. Deposition was performed at 650°C, 750°C, and 850°C, under background oxygen pressures of 100mTorr, 150mTorr, and 200mTorr. Laser fluence was maintained between ~1.5-3.5 J/cm^2 with a fixed repetition rate of 10Hz. The estimated deposition rate was 0.01nm per shot. Films were grown to ~300nm (30,000 shots), except one thinner film at 7,500 shots, resulting in an estimated thickness of 75.47nm via analysis of x-ray reflectivity.

Parameter	**Value(s)**
Target Materials	$CaSnO_3$, La-doped $CaSnO_3$ (8% La)
Substrates	$LaAlO_3$ (100), $SrTiO_3$ (100)
Substrate Sizes	$5 \times 5 \times 0.5\text{mm}^3$, $3 \times 3 \times 1\text{mm}^3$
Laser Type	KrF Excimer ($\lambda = 248$nm)
Laser Voltage	16.8kV – 27kV
Laser Fluence	~1.5 – 3.5 J/cm^2
Repetition Rate	10 Hz
Deposition Temperatures	650°C, 750°C, 850°C
O_2 Pressures	100, 150, 200 mTorr
Est. Deposition Rate	~0.01 nm/shot
Film Thicknesses	~300 nm (30,000 shots), ~75 nm (7,500 shots)

Table 2: Table of Deposition Parameters for $CaSnO_3$ and La-$CaSnO_3$ films.

Prior to deposition, LAO substrates were cleaned via a sequential sonication in a Branson Bransonic CPXH Digital Bath 2800. Each step involved 10mL of solution, followed by drying by nitrogen gas before transfer to the next solvent. The substrate was sonicated in: (1) Hellmanex solution (5 min), (2) deionized (DI) water (5 min), (3) acetone (5 min), (4) isopropyl alcohol (IPA) (5 min), and finally DI water (10 min). After final drying, the substrate was bonded onto the substrate holder with a silver-acetone solution and heated to 170°C on a DATAPLATE Digital Hot Plate/Stirrer (PMC 720 Series). For STO, the process was (1) acetone (10 min), (2) IPA (10 min), and DI water (10 min). Once heated, the holder was transferred to the PLD chamber. The following is the general process which took place for the deposition.

Once the substrate-mounted holder was placed in the PLD chamber, a pre-ablation step was performed at atmospheric pressure (due to a malfunctional shutter). During pre-ablation, the target stage rotated at 30°/sec, while setting a negative/positive raster speed of 1.0/15.0°/sec with the negative/positive raster set at 18.0/19.5°. The substrate-to-target distance was 85mm. Pre-ablation was completed at 5Hz and sustained for 2000 shots (~6 min 40 sec).

Following pre-ablation, the chamber door was cleaned with IPA and sealed. Pump-down was done via a roughing scroll pump, then a turbopump running at 1000Hz, reaching a base pressure between 7×10^{-7} and 5.9×10^{-6} Torr. The heating profile was started, and the turbopump throttled to 200Hz during heating. The temperature ramp began with approaching 600°C at 25°C/min, then 15°C/min to the desired target temperature (650°C, 750°C, or 850°C), where it would be held during the time of the laser ablation.

Once the final temperature was reached, oxygen (99.999% purity) was introduced to the chamber via mass flow control (MFC) to achieve the desired background oxygen pressure (100, 150, or 200mTorr). Once the pressure stabilized, the target stage would be rotated and rastered as

during pre-ablation, and the substrate holder would be rotated at 30°/sec. Laser ablation was then initiated with the laser shutter opened. Depositions were performed at 10 Hz for 30,000 shots (50 min), unless otherwise specified.

Once the deposition was complete, an annealing profile was applied across all films. The gate valves and pumps shut/stopped, and the MFC would be shut off. Oxygen was manually introduced via a coarse line to set the background pressure to ~200 Torr. The annealing heating profile would be started, which maintained the substrate at the deposition temperature for 30 minutes, followed by a ramp down to 600°C at 10°C/min, then ramp down to room temperature at 25°C/min. Once the chamber reached a safe temperature, the chamber was vented back to atmospheric pressure, and the substrate holder was removed.

3.3 Characterization - X-Ray Diffraction

X-ray diffraction is a non-destructive technique used to analyze the crystal structure, phase composition, and orientation of materials with high accuracy. When x-rays interact with a crystalline material, they diffract according to Bragg's Law:

$$n\lambda = 2dsin\theta \tag{3.1}$$

where λ is the incident wavelength of the x-ray, d is the distance between atomic planes in the crystal lattice, and θ is the angle of incidence. When the path difference between reflected x-rays are integer multiples of the wavelength, this leads to constructive interference, enhancing the signal intensity at certain diffraction angles, giving high-intensity peaks that correspond to crystal planes. The powders and films in this study were characterized using a Rigaku SmartLab X-ray diffractometer with a Cu Kα_1 source ($\lambda = 1.5406$Å). X-ray reflectivity (XRR) was also measured to evaluate the thickness of the films.

3.4 Characterization – UV-Vis Spectroscopy

Ultraviolet-visible (UV-vis) spectroscopy is a useful tool in estimating the bandgap of a material. In the context of thin films, a diffuse reflection measurement from a UV-vis spectrometer is enough to extrapolate an estimated value for the bandgap. Materials can absorb light at certain wavelengths in accordance with their crystal structure and stoichiometry. Based off the crystal structure, the band structure is formed, which determines the bandgap (if any) that defines the transition between the valence and conduction bands. This bandgap dictates what wavelengths of light can be absorbed, which is what makes a UV-vis spectrometer useful. In this study, a PerkinElmer UV/VIS/NIR Spectrometer Lambda 750 was used to carry out transmission measurements. The films were secured between two transparent sheets, and a reflective backplate was placed opposite of the incident light, allowing the reflected wavelengths to be recorded. The subsequent direct bandgap data was calculated by using the following equation:

$$(\alpha h\nu)^2 = \frac{2.302 \times A\ (a.u)^2}{\frac{1240\ (eV * nm)}{\lambda\ (nm)}} \tag{3.2}$$

where A is the measured absorbance, and λ is the incident wavelength on the sample. The absorbance was measured between λ = 250 to 1100 nm. When plotting the energy eV against $(\alpha h\nu)^2$, then extrapolating a line of best fit on the steep slope, the x-intercept will be the estimated direct bandgap value. The indirect bandgap (for LAO and STO) were found by taking the square root of the above equation, instead of squaring it.

Chapter 4: Discussion

4.1 Optimized Parameters

The experiment challenged the growth of the ultra-wide bandgap material $CaSnO_3$ to determine the optimal conditions to grow both pure and doped thin films due to the lack of literature on the subject, and because dopant incorporation into $CaSnO_3$ is difficult.[14] Additionally, utilizing a doped target with impurity phase is proven to still grow a film without impurity phases in some cases. Although the films were not semiconducting, the results of this optimization and what the characterization shows is discussed to prove such growths occurred and what can be done in the future to create high-quality semiconducting thin films of $CaSnO_3$.

The optimal growth conditions included a background oxygen pressure of 100mTorr and a heater temperature of 850°C. It should be noted that the heater was not calibrated and could have a temperature of upwards or downwards of 50°C. The optimal fluence seems to change depending on background pressure, though, a fluence of 2.2-2.5 J/cm^2 provided consistent growth, and this phenomenon is further expanded upon in Section 4.3. The undoped growth on STO and the doped growth on LAO indicate an orthorhombic phase by the expansion of shoulder peaks on both sides of the peak maximum. The reason for this being that while the growth is taking place, the orthorhombic tilting nature of $CaSnO_3$ allows it to misalign from the substrate orientation, creating domains of slightly misoriented symmetries from the main orientation. This misorientation can be seen via XRD, as shown below in the overlayed figure:

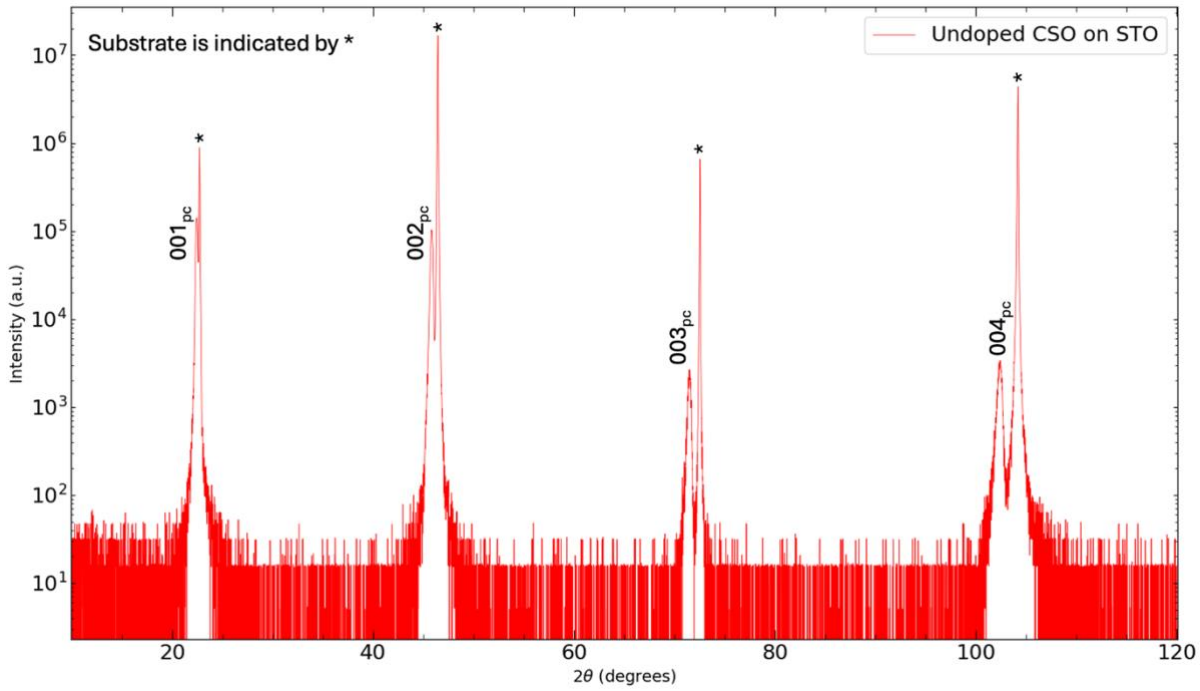

Figure 5: 2θ scan of $CaSnO_3$ film grown at 100mTorr at 850C, indicating epitaxial growth on $SrTiO_3$ (100) substrate.

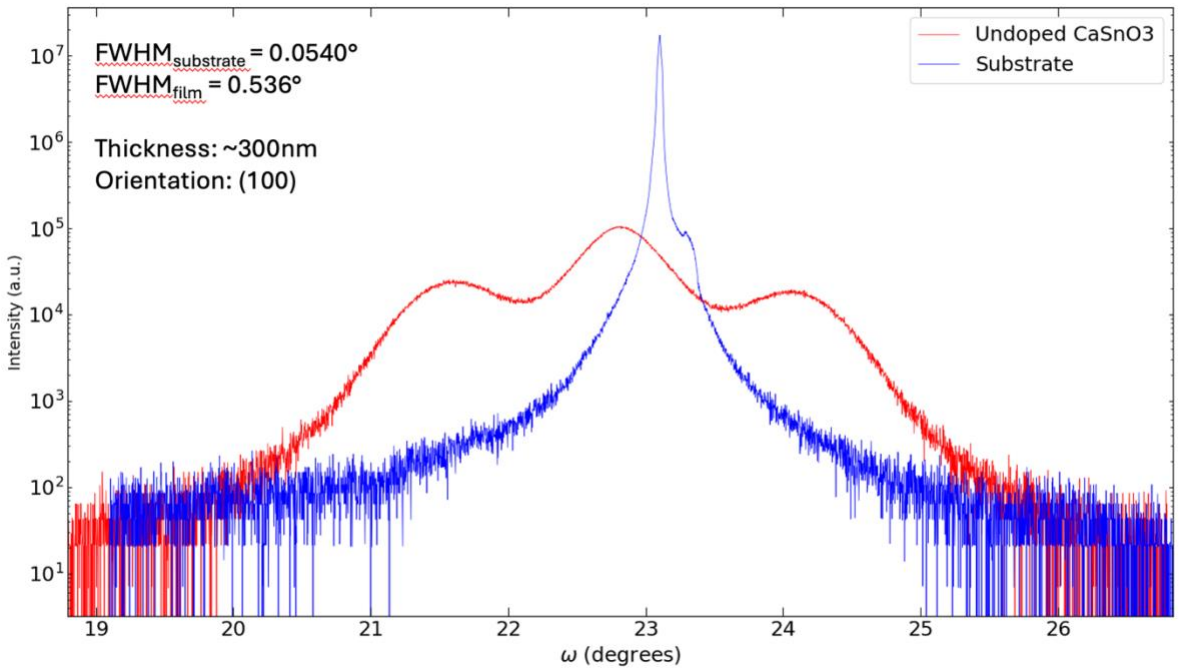

Figure 6: Rocking curve scan of $CaSnO_3$ film (red) and $SrTiO_3$ substrate (blue) with FWHM, thickness, and orientation as insets. The $CaSnO_3$ film indicates relaxation back into orthorhombic phase, giving evidence of strained cubic growth when not relaxed.

This orthorhombic tilting nature has recovered in the STO film and is evidence of a relaxed thin film. This occurrence suggests that the crystal system is growing in a strained cubic form but has a relaxation back into an orthorhombic form. Additionally, RSM was conducted on the sample shown in Figures 5 and 6, which also indicates a relaxation into the orthorhombic phase.

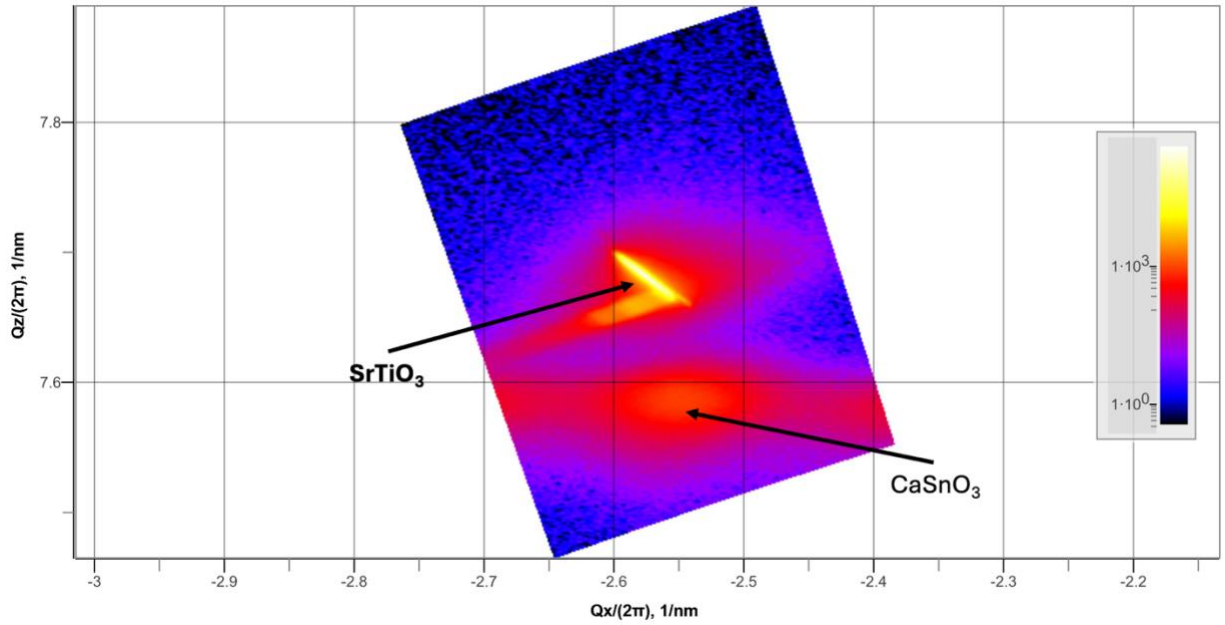

Figure 7: Reciprocal space map (RSM) aligned to the (103) direction. The $SrTiO_3$ substrate can be seen as the bright spot in the middle, while the relaxed phases of $CaSnO_3$ can be seen both in the middle and bottom portions of the map. Estimated in-plane and out-of-plane lattice parameters were calculated to be 3.922 Å and 3.958 Å, respectively.

Additionally, the thin film deposited at 7,500 shots was analyzed for thickness estimation using x-ray reflectivity (XRR). The following figure showcases the XRR plot, and the estimation of the fringe frequency gives a thickness of ~75.47 nm, which correlates to an estimated growth rate of 0.01 nm/shot.

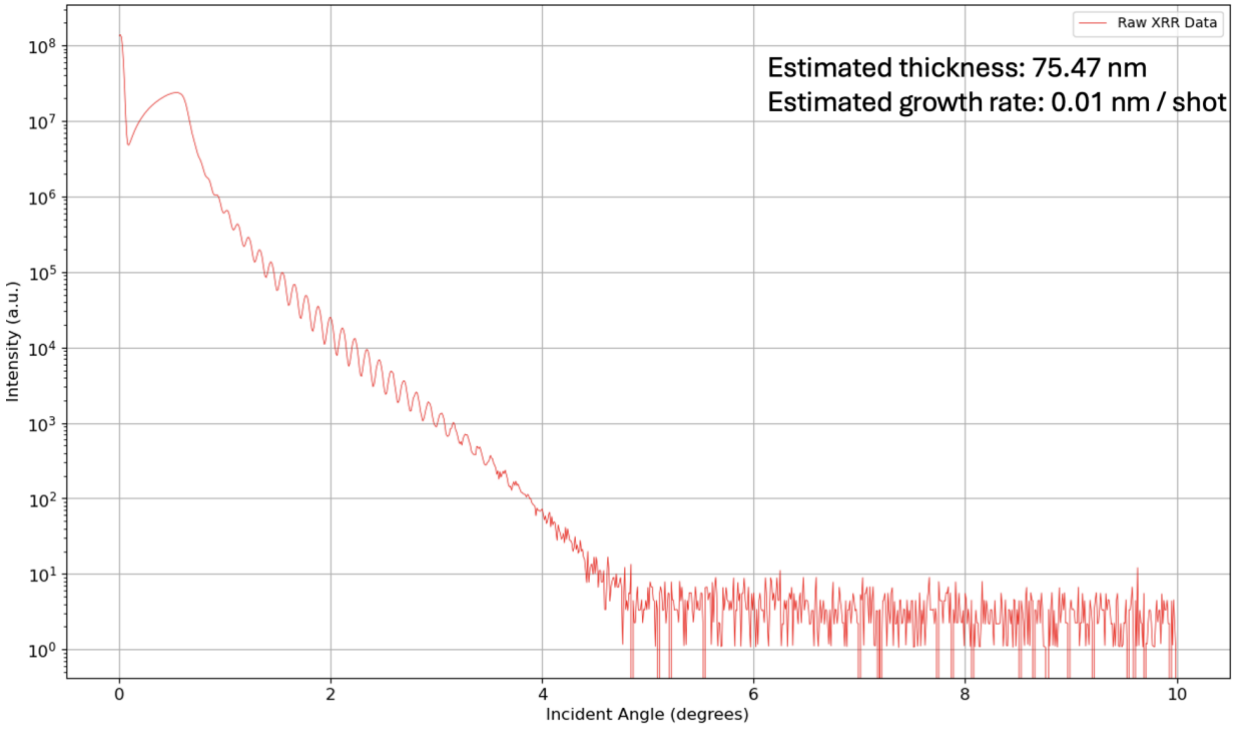

Figure 8: X-ray reflectivity plot of the 7,500 shot $CaSnO_3$ film grown on $SrTiO_3$. The estimated thickness is ~75 nm, which estimates the thicker films grown in this study to be ~300 nm.

4.2 Lattice Constant Mismatch and Crystalline Quality

The pseudocubic bulk lattice constant as calculated from data from the Materials Project[82] and ICSD database[83] is 3.9654Å. The total mismatch of the undoped film lattice constant on LAO from the bulk lattice constant ranges from 0.019% - 0.432%. The total mismatch of the film lattice constant on LAO to the LAO substrate lattice constant is around -4.638%. For the doped film, the mismatch against the bulk constant ranges from -0.126% - 0.205%, while the mismatch against the LAO substrate is around -4.678%. There does not seem to be any significant changes between lattice constants between the undoped and doped films. This could be due to the lack of incorporation of the lanthanum dopant in the doped powder, which would likely indicate some expansion of the lattice parameter, as lanthanum[84] has a 12-fold coordination ionic radius of 1.36 Å, while calcium[85] has a 12-fold coordination ionic radius of 1.34 Å.

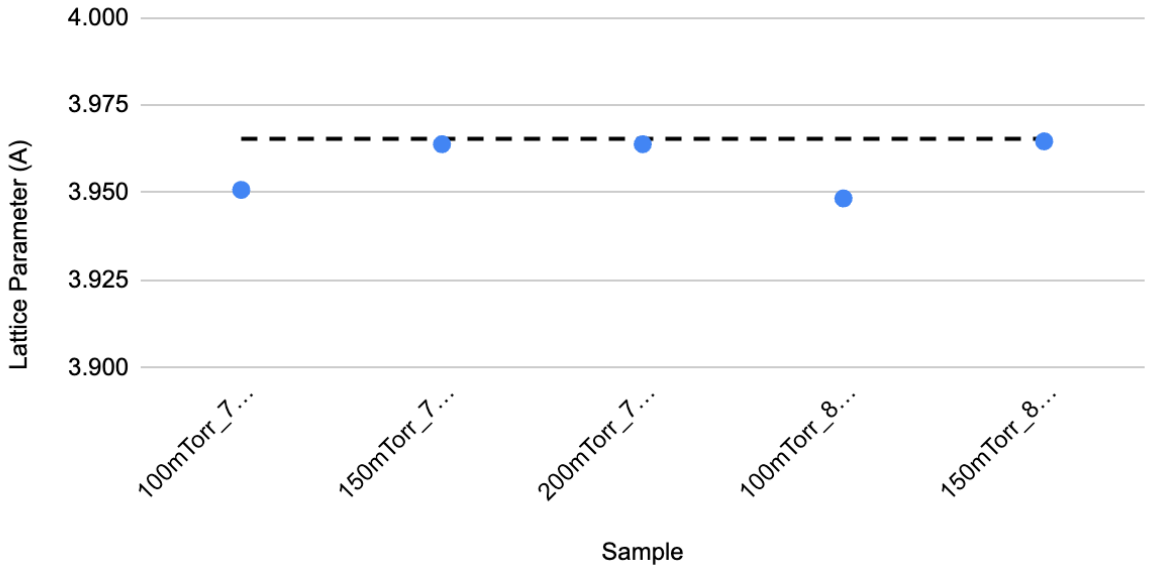
4.000
3.975
3.950
3.925
3.900
Lattice Parameter (A)
100mTorr_7…
150mTorr_7…
200mTorr_7…
100mTorr_8…
150mTorr_8…
Sample

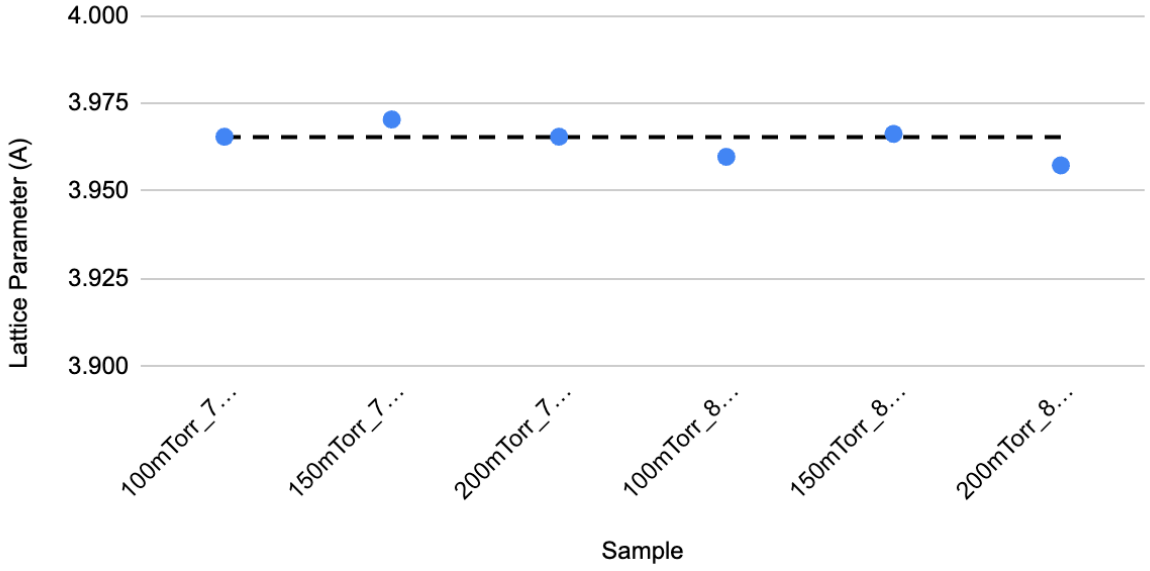
4.000
3.975
3.950
3.925
3.900
Lattice Parameter (A)
100mTorr_7…
150mTorr_7…
200mTorr_7…
100mTorr_8…
150mTorr_8…
200mTorr_8…
Sample

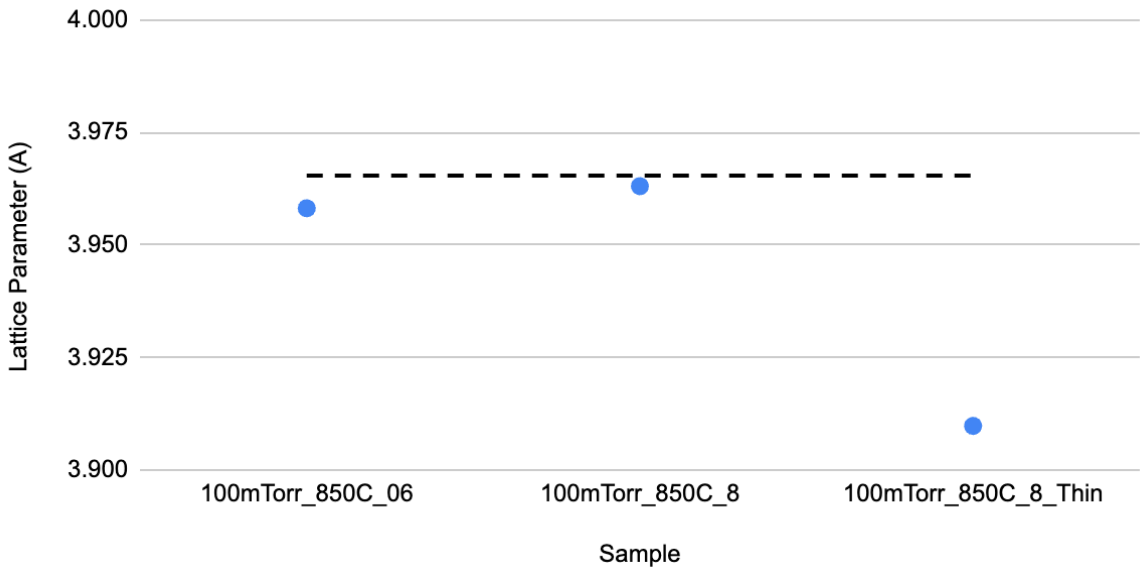

Figure 9: Graphs of comparing the bulk pseudocubic lattice constant against the films grown in the study. Undoped films grown at 750◦C (first three), then 850◦C (last two) on LAO (top), doped films at 750◦C (first three) then 850◦C (last three) on LAO (middle), and the series of three films grown on STO (bottom).

There seems to be a minor trend in the undoped films on LAO that indicates with increasing oxygen pressure, the lattice parameter of the film trends closer to the bulk lattice constant. However, with the decreasing background oxygen pressure, the crystalline quality improves. Though, this behavior is not reflected in the doped films, and more experiments are needed to determine if this phenomenon can be reproduced at the extremes. With the films grown on STO, the lattice parameters of the film compared with the bulk constant are around 0.060%-0.184%. Considering a pseudocubic lattice parameter of 3.9654Å, and the STO substrate lattice constant being 3.905Å, compressive strain on the film would be expected from the interaction between the substrate and film. This is recorded as a negative number in terms of the lattice mismatch, which is -1.343% for the undoped film, and -1.465% for the doped film. An interesting point of discussion is the fact that the angles in which the 200 peak of diffraction occurs for the CaSnO3 films does not shift with any trend concerning doping or substrate used. Effectively, no conclusion can be drawn that correlates the lattice parameter to strain, as one would expect a shift in higher 2θ values

if the compressive strain on STO influenced the lattice parameter, and even more so with LAO if the film grew in a strained manner. In comparison to the films grown on LAO and the films grown on STO, the peak positions have not shifted with any discernable difference in comparison to the corresponding bulk 110 and 220 diffraction peaks.

Sample	Undoped CSO/LAO 2θ 002 Peak Location (deg)	Doped CSO/LAO 2θ 002 Peak Location (deg)	Undoped/Doped CSO/STO 2θ 002 Peak Location (deg)
100mTorr 750C	45.94	45.76	X
150mTorr 750C	45.78	45.7	X
200mTorr 750C	45.78	45.76	X
100mTorr 850C	45.97	45.83	45.85/45.79
150mTorr 850C	45.77	45.75	X
200mTorr 850C	X	45.86	X

Table 3: Table showcasing the 2θ values in which the 002 diffraction peak occurs for the CSO thin film, both doped and undoped on LAO and STO substrates.

Therefore, there is no conclusive evidence that the undoped and doped films have a correlation between dopant incorporation and lattice parameter change. This could be due to the fact that the films are highly relaxed, due to the ~300nm thickness of these films. The expected lattice parameter change should be apparent in terms of the compressive strain and substrate mismatch, however, oxygen vacancies or the valency of electrons could be contributing to this anomaly, or otherwise, the thickness.

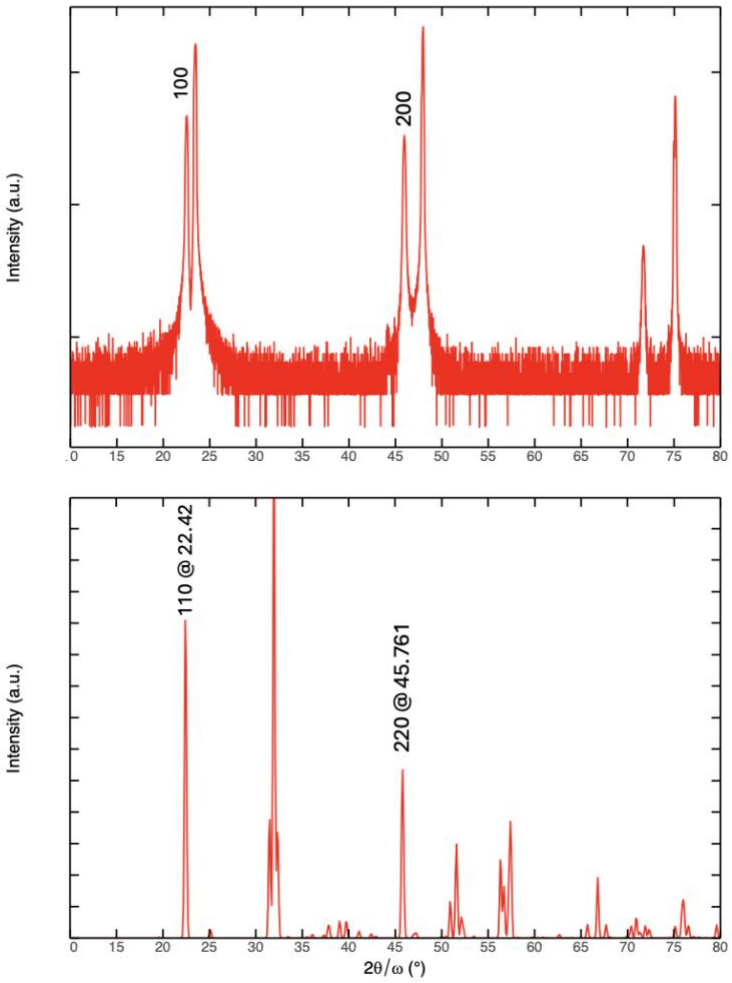

Figure 10: XRD plots comparing thin film of $CaSnO_3$ vs. bulk powder diffraction patterns. Showcased are the orthorhombic planes 110 and 220 of the bulk powder aligning with the undoped thin film planes on LAO (100mTorr @ 850C) of 100 and 200.

4.3 Phase Field and Fluence

During the study, the growths' fluence had varied immensely, due to a fluctuating laser voltage and spot size. It should be said that with the excimer laser in question, when the voltage was changed due to a decrease in output energy, the resulting spot size on the target changed. The ability to keep the fluence constant was challenging, but it led to a notable observation to derive a phase field of the growth regime for the $CaSnO_3$ system.

Below are figures of the phase field where the growths are plotted as ones that grew a $CaSnO_3$ film (green), and those which did not (red). Based off the previous literature, the intended fluence range of 1.5-2.5 J/cm^2 is commonly used.[8, 12, 20-31, 32-69] However, there were some experiments that even within this range, would not grow a film. These deviations revealed a regime that seems to suggest that only certain fluences can grow the $CaSnO_3$ system. For both the undoped and doped growths, it is seen that the films will not grow at 650°C. This seems to be the primary reason that these films don't grow, not the fluence. However, one can then see that for the undoped samples, the two growths at 850°C with a background pressure of 200mTorr did not grow around 1.8 J/cm^2. Though, the growth at the same temperature at 100mTorr grew a film at 1.55 J/cm^2. This suggests that even at a lower fluence, a lower background oxygen pressure allows the atoms to reach the substrate surface, while at higher pressures, a higher fluence is needed.

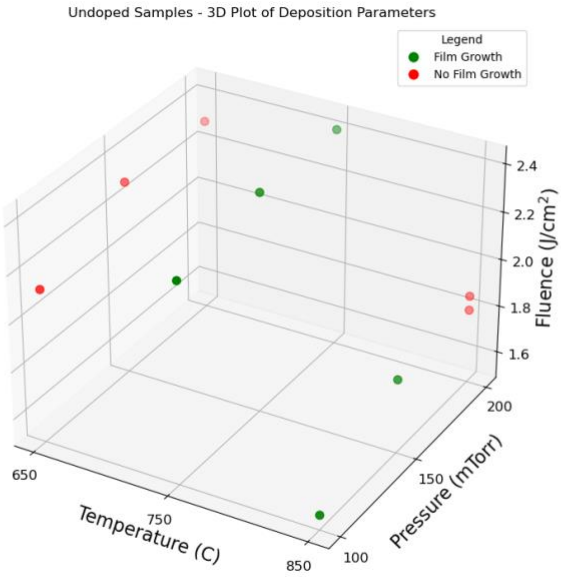

Figure 11: Fluence phase field of undoped growths of $CaSnO_3$. Growths taken place at 650°C would not form. Fluences between 1.55 – 2.4 J/cm^2 could grow films at 100 and 150 mTorr, but 200mTorr requires a higher fluence to grow.

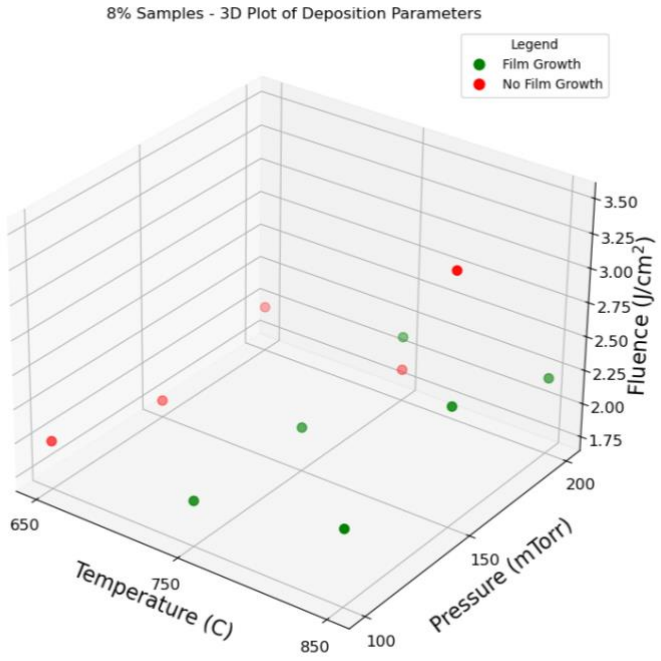

Figure 12: Fluence phase field of doped growths of $CaSnO_3$. Growths taken place at 650°C would not form. Fluences between 1.88 – 2.53 J/cm^2 grew films.

This leads to another aspect of the growths that evolves the previous point. For the 8% doped samples, no film grew at 650°C. However, a growth at 850°C at 150mTorr with a fluence of 3.486 J/cm^2 did not grow a film. Another growth took place at the same parameters, but instead with a fluence ~2.53 J/cm^2. This growth grew a film. Therefore, this suggests that there is some regime of fluence above 2.53 J/cm^2 that $CaSnO_3$ films will not grow for a background oxygen pressure of 150mTorr, and possibly, other pressures. In contrast to the previous point that a low enough fluence isn't enough to ablate the target material with enough energy to reach the surface, this finding suggests that with too large of a fluence, the material hits the surface of the substrate with too much energy, leading to a growth that doesn't progress epitaxially. Regarding the growth that took place at 750°C at 200mTorr, it can be seen once again that a fluence of 1.88 J/cm^2 is not

enough to grow a film. This again suggests that a lower fluence is not enough to propel the material through a higher oxygen pressure. Though the current optimized conditions seem to be at 850°C at 100mTorr, future experiments are encouraged to try depositions at lower pressures below 100mTorr, as well as varying the fluence to determine the true regime where the $CaSnO_3$ system can grow.

4.4 UV-vis Measurements

The optical bandgap measurements made were inconclusive, as perhaps the instrumentation and setup were incorrect. There is no distinguishment between substrate and film contribution to bandgap. However, the results found can be discussed here.

The estimated bandgap of these $CaSnO_3$ films should have been in the range of 4.1eV to 4.4eV, according to literature findings.[10, 11, 12] The bandgap of LAO[86] can reach up to 6.1eV and the bandgap of STO is 3.75eV (direct) and 3.25eV (indirect).[87] We should expect to estimate the films' bandgaps within the 4.1eV-4.4eV, however, the resulting measurements estimated bandgaps between 3.82eV-3.89eV. To ensure that this outcome was consistent, test measurements of reference substrates of LAO and STO were also ran. Both reference estimations came out to be 3.89eV for the direct bandgap estimation, and 3.56eV and 3.53eV for the indirect bandgap estimation for LAO and STO, respectively. Though, it should be mentioned that even for samples in which films did not grow, the value of the estimated bandgap was similar to samples where the film did grow. For instance, the undoped film that did not grow (850°C at 200mTorr with a fluence of 1.8J/cm^2) had an estimated direct bandgap of 3.82eV. Though, a doped film that did grow (750°C, 150mTorr, 1.96J/cm^2) also had an estimated direct bandgap of 3.82eV. The inconclusiveness of this portion of the study can be further refined and carried out in future work, as the instrumentation may have been faulty, or improper methods were utilized.

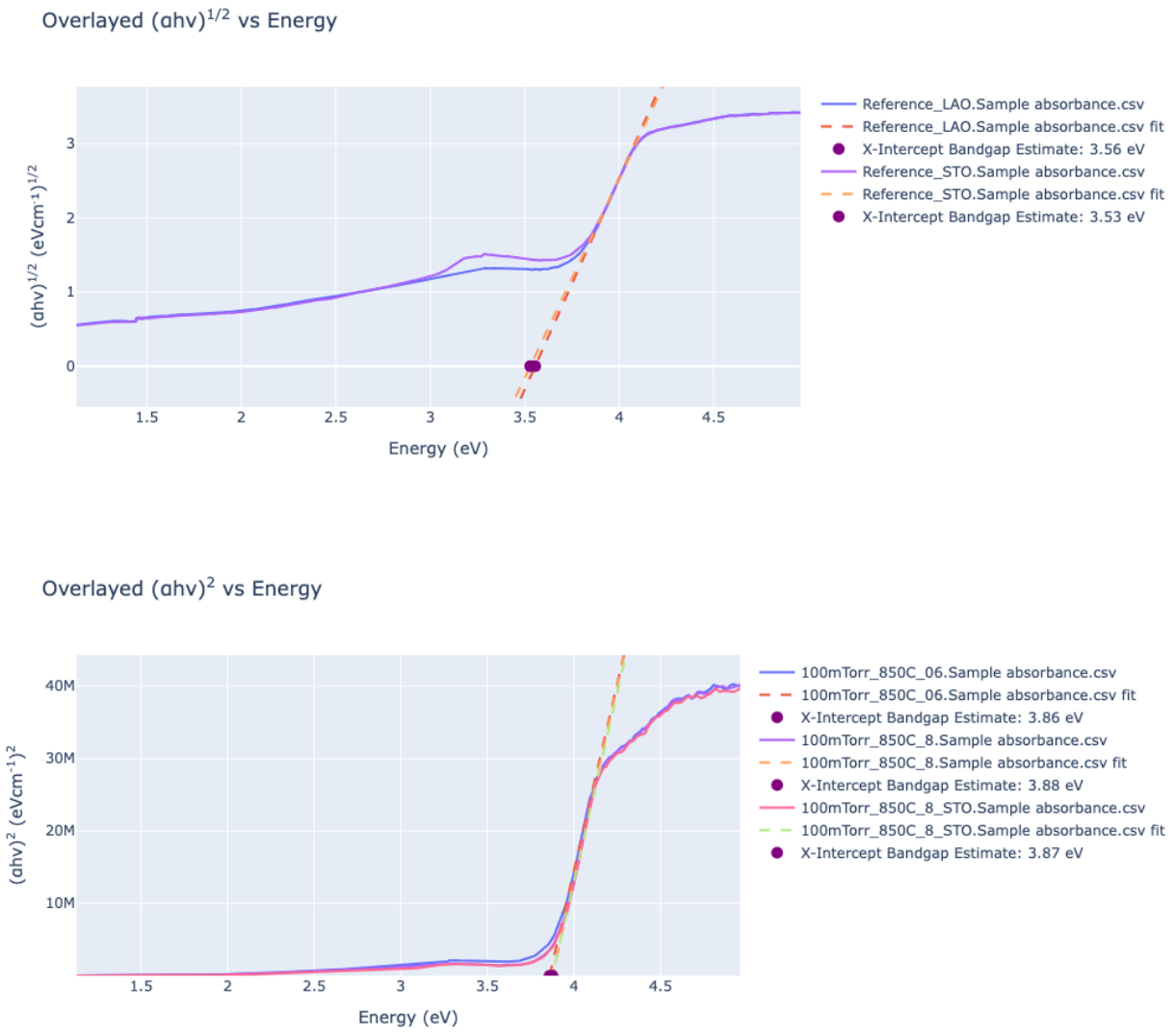

Figure 13: Tauc plots showing estimated indirect bandgap for LAO and STO substrates (top) and estimated direct bandgap for $CaSnO_3$ films grown at 100mTorr at 850°C (bottom).

4.5 Powder Refinement

Powder fabrication was carried with various methodologies. Pure $CaSnO_3$ could be fabricated with a reliable method, though, the heavily doped versions of the powder proved challenging to be both conductive and phase pure. Secondary phases of the $La_2Sn_2O_7$ pyrochlore consistently appeared in the more heavily doped powder experiments. Though this pyrochlore secondary phase appeared for the 8% doped $CaSnO_3$ target, the majority of the films which were

grown with this target did not exhibit secondary phases. The only film that exhibited secondary phases was the doped film grown on LAO at 750°C at 200mTorr with a fluence of 2.13J/cm^2. This pyrochlore phase can be seen in blue, overlayed with the actual 8% doped powder used in this paper's 8% doped film growths.

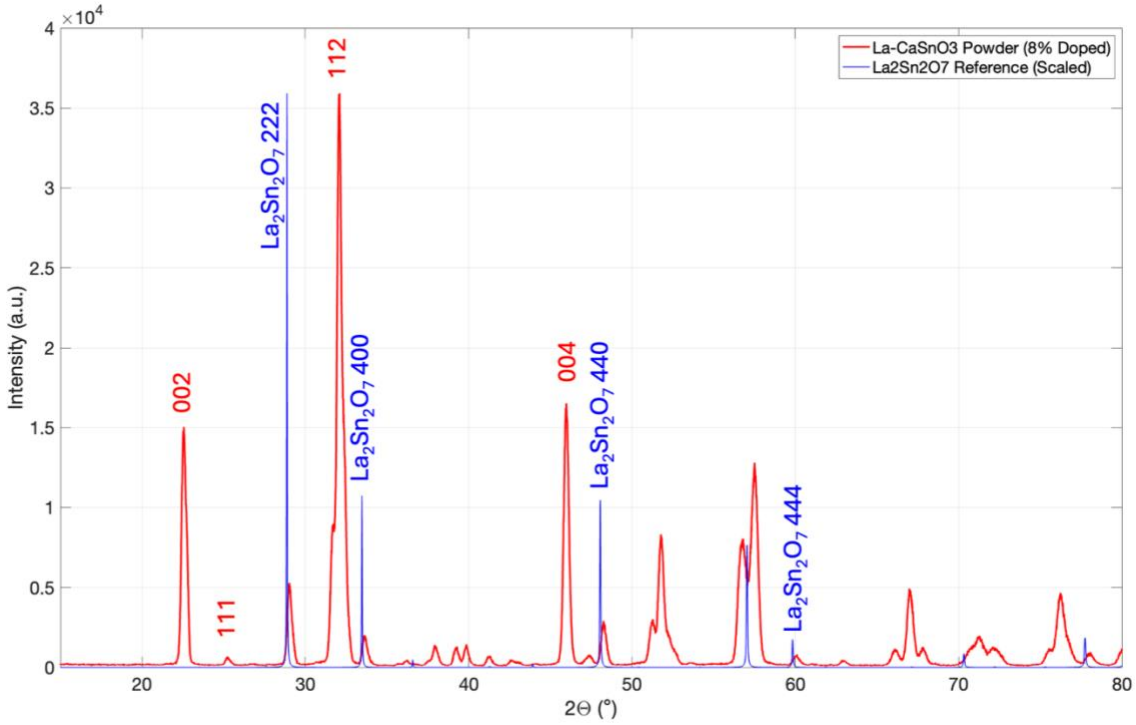

Figure 14: 8% La-$CaSnO_3$ powder diffraction pattern (red) overlayed with $La_2Sn_2O_7$ reference (blue), indicating impurity phase.

Various other powders were fabricated to test the ability to incorporate the lanthanum dopant and increase the dopant activation while maintaining the perovskite structure of $CaSnO_3$. These powders were doped with lanthanum with concentrations in accordance with the number of carriers to be incorporated (if 100% activated), which includes molar amounts corresponding to 1×10^{21}, 1×10^{20}, 1×10^{19}, and 1×10^{18} cm^{-3}.

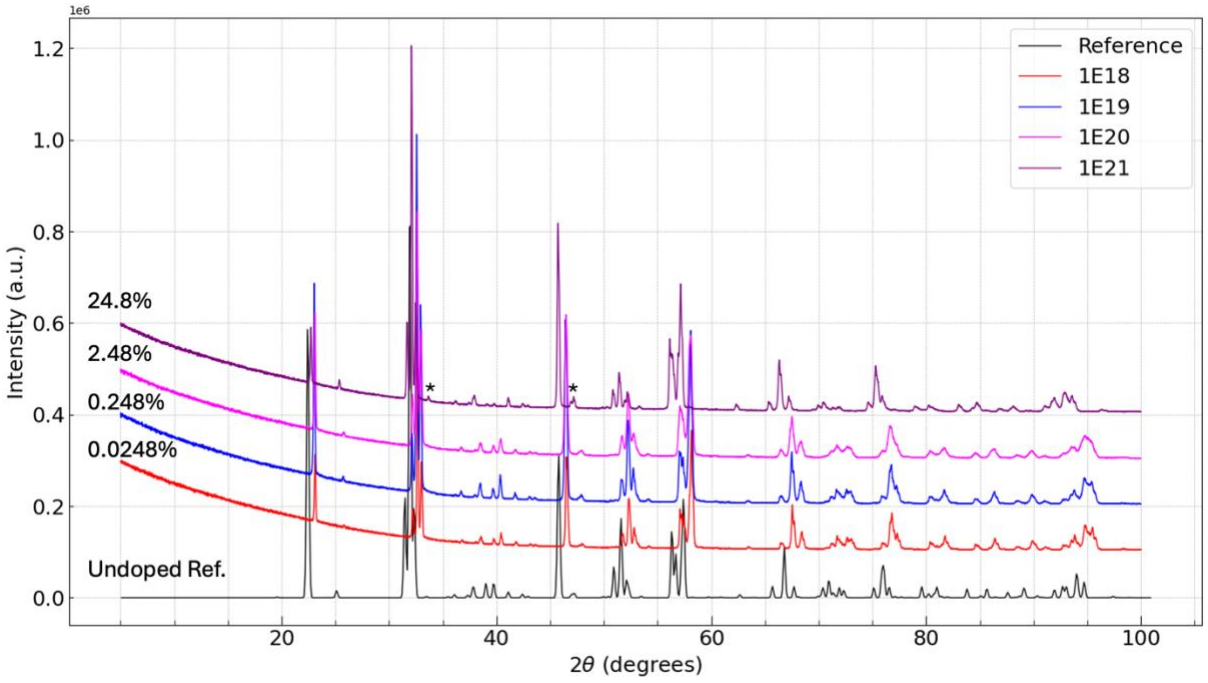

Figure 15: XRD diffraction patterns of the doping trials, with reference[88] $CaSnO_3$ powder (black), indicating that a shift has occurred in the various trials. Possible pyrochlore impurity phase is indicated by (*).

In Figure 15, there is a noticeable reduction in the pyrochlore phase with the highly alloyed 24.8% La-incorporation. This suggests that the methodology employed has had an effect on the way the La dopant is incorporated into the crystal structure. Additionally, when taking a closer look on the various peaks, there seems to be a light trend with increasing dopant %. It should be expected that with increasing La %, the further the plots shift to lower 2θ values. However, with the misalignment from the reference, this study requires further exploration to determine if the La dopant is truly incorporated. Additionally, this trend isn't consistent between the four trials. In actuality, the 0.248% is shifted more leftwards than the 2.48%. However, considering the 0.0248% to the 24.8%, there is a trend of leftwards shifting, disregarding the middle inconsistency.

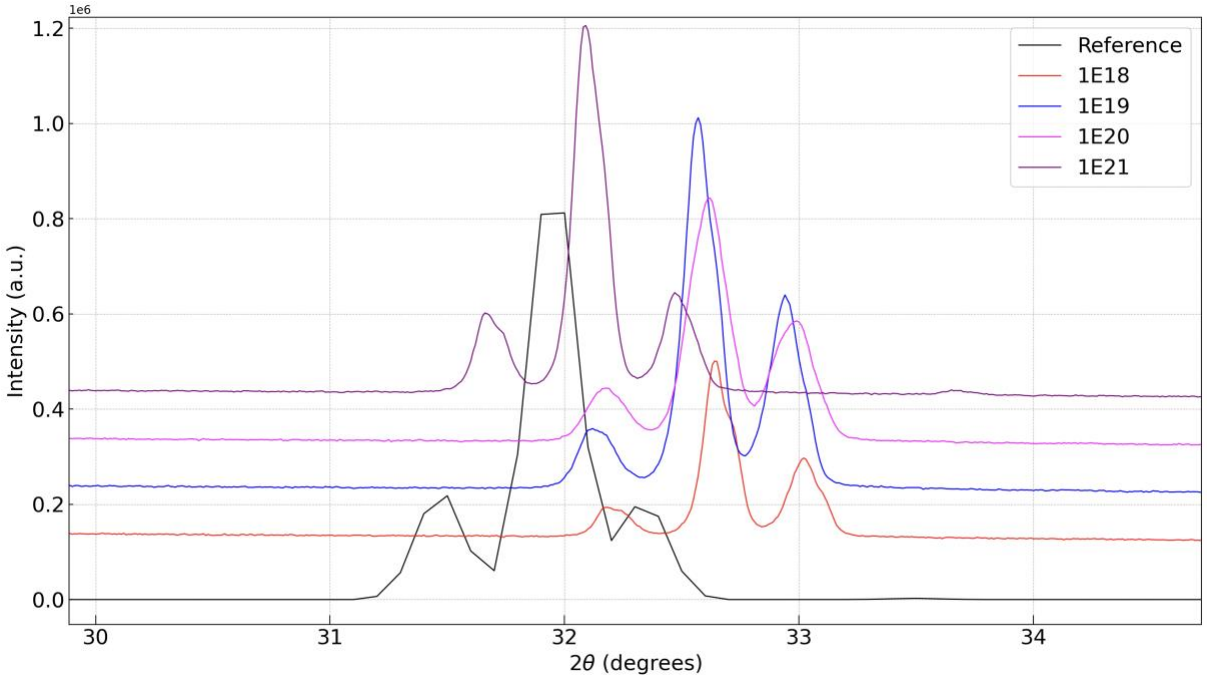

Figure 16: Zoomed in view on the 020 (leftmost), 112 (middle), 220 (rightmost) peaks of diffraction for the doping series. A trend can be seen within the trials, disregarding the reference (bottom line). However, interestingly, each of the series falls right of the reference, instead of the expected leftward shifting due to La-incorporation. This suggests that either the La dopant was not properly incorporated, or other phenomena are at work.

Regarding further study, the literature survey that was conducted also included a variety of oxide systems that have been grown in the literature and their PLD deposition parameters. Figures of these parameters have been included in the supplementary material, and these parameters can be further utilized as a guiding baseline for future depositions, may it be $CaSnO_3$, or other oxide systems.[89-184] Additionally, Nelson-Riley estimations of lattice parameters[185] and comparison with the bulk lattice parameter of $CaSnO_3$ are included in the appendix.

Chapter 5: Conclusion

The previously discussed study focuses on challenging the single-crystalline growth of the ultra-wide bandgap oxide semiconductor $CaSnO_3$. The fabrication of polycrystalline powders facilitated the single-crystalline growth of $CaSnO_3$ thin films, which resulted in proving the relaxed orthorhombic phase of the crystal system. This study concludes that the pulsed laser deposition method is viable for the growth of epitaxial, perovskite-phase $CaSnO_3$. Albeit there is no evidence of semiconductive behavior with these samples, the study optimized the growth conditions of single-crystalline $CaSnO_3$, which also led to the correlation of a certain fluence being required to grow at low and high background oxygen pressures, as well as a relatively independent single-crystalline nature with an impure phase PLD target.

Additionally, further analysis indicates that as the background oxygen pressure increases, the pseudocubic lattice constant of the undoped $CaSnO_3$ films form closer to the bulk lattice constant. Conversely, when the background oxygen pressure decreases, the single-crystalline quality improves, as indicated by the FWHMs of the film peaks. This study concludes that due to the increasing oxygen pressure, the reduction in oxygen vacancies contribute to the contraction of the lattice constant to be closer to the bulk constant.

Future work includes the further study of the optical bandgap of the grown films, as the instrumentation was limited during the timeframe of this study. Additionally, further growths are encouraged to be done at a lower oxygen pressure, as there are both literary and experimental indications that the tin stannates grown at a lower oxygen pressure have better crystallinity.[14] This may also help improve conductivity due to the nature of oxygen vacancies acting as an electron donor. Not only this, but an optimization in the solid-state reaction route of fabricating doped pure-

phase polycrystalline powders of $CaSnO_3$ is crucial to utilize the PLD techniques main advantages, as pure-phase, conductive powders could very well translate to semiconducting and high-performing thin films. This study has completed the preliminary trials of this powder work, which suggests possible incorporation of the La dopant, but needs further confirmation. The optimization of this step can create an advantageous opportunity to synthesize the UWBG semiconductor $CaSnO_3$ more efficiently and pave the way for new devices moving forward.

REFERENCES

[1] U.S. Geological Survey, *MINERAL COMMODITY SUMMARIES 2025* (2025).

[2] M. Cuoco, and A. Di Bernardo, "Materials challenges for SrRuO3: From conventional to quantum electronics," APL Materials **10**(9), (2022).

[3] D.K. Singh, A. Ernst, Vitalii Dugaev, Y. Chen, and J. Gunasekera, "Quantum Magnetic Properties and Metal-to-Insulator Transition in Chemically Doped Calcium Ruthenate Perovskite," Physica Status Solidi (B) **259**(4), (2022).

[4] M.N. Gastiasoro, J. Ruhman, and R.M. Fernandes, "Superconductivity in dilute SrTiO3: A review," Annals of Physics **417**, 168107–168107 (2020).

[5] S.P. More, M.V. Khedkar, S.A. Jadhav, S.B. Somvanshi, A.V. Humbe, and K.M. Jadhav, "Wet chemical synthesis and investigations of structural and dielectric properties of BaTiO3 nanoparticles," Journal of Physics Conference Series **1644**(1), 012007–012007 (2020).

[6] S. Kumar, A. Prakash, J. Yue, Bharat Jalan, and S.J. Koester, "Demonstration of a Depletion-Mode $SrSnO_3$ n-Channel MESFET," IEEE Electron Device Letters **39**(9), 1381–1384 (2018).

[7] T. Truttmann, A. Prakash, J. Yue, T.E. Mates, and Bharat Jalan, "Dopant solubility and charge compensation in La-doped SrSnO3 films," Applied Physics Letters **115**(15), (2019).

[8] J. Seo, J. Kim, J.H. Kim, J.H. Kim, and K. Char, "Fully Deep-UV Transparent Thin Film Transistors Based on $SrSnO_3$," Advanced Electronic Materials **10**(1), (2023).

[9] H. Paik, Z. Chen, E. Lochocki, H Ariel Seidner, A. Verma, N. Tanen, J. Park, M. Uchida, S. Shang, Bi Cheng Zhou, M. Brützam, R. Uecker, Z. Liu, D. Jena, K. Shen, D.A. Muller, and D.G. Schlom, "Adsorption-controlled growth of La-doped $BaSnO_3$ by molecular-beam epitaxy," APL Materials **5**(11), 116107–116107 (2017).

[10] Manh Hoang Tran, T. Park, and J. Hur, "Wide-Bandgap $CaSnO_3$ Perovskite As an Efficient and Selective Deep-UV Absorber for Self-Powered and High-Performance p-i-n Photodetector," ACS Applied Materials & Interfaces **13**(11), 13372–13382 (2021).

[11] F. Liu, Prafful Golani, T.K. Truttmann, I. Evangelista, M.A. Smeaton, D. Bugallo, J. Wen, Anusha Kamath Manjeshwar, S.J. May, L.F. Kourkoutis, A. Janotti, S.J. Koester, and Bharat Jalan, "Doping the Undopable: Hybrid Molecular Beam Epitaxy Growth, n-Type Doping, and Field-Effect Transistor Using $CaSnO_3$," ACS Nano **17**(17), 16912–16922 (2023).

[12] M. Wei, H.J. Cho, and H. Ohta, "Tuning of the Optoelectronic Properties for Transparent Oxide Semiconductor $ASnO_3$ by Modulating the Size of A-Ions," ACS Applied Electronic Materials **2**(12), 3971–3976 (2020).

[13] D.J. Singh, Q. Xu, and K.P. Ong, "Strain effects on the band gap and optical properties of perovskite $SrSnO_3$ and $BaSnO_3$," Applied Physics Letters **104**(1), 011910–011910 (2014).

[14] L. Weston, L. Bjaalie, K. Krishnaswamy, and C.G. Van de Walle, "Origins of n -type doping difficulties in perovskite stannates," Physical Review B **97**(5), (2018).

[15] Lars Bjaalie, Burak Himmetoglu, L. Weston, A. Janotti, and C.G. Van, "Oxide interfaces for novel electronic applications," New Journal of Physics **16**(2), 025005–025005 (2014).

[16]"NSM Archive - Silicon Carbide (SiC)," Www.ioffe.ru, (n.d.).

[17] K. Czelej, M. Mansoor, S.M. Ali, M. Tas, Sorkhe, Yahya A, M. Mansoor, M. Mansoor, B. Derin, O. Ergen, S. Timur, and M. Ürgen, "Atomistic Origins of Various Luminescent Centers and nType Conductivity in GaN: Exploring the Point Defects Induced by Cr, Mn, and O through an Ab Initio Thermodynamic Approach," Chem. Mater. **36**(13), 6392–6409 (2024).

[18] M. Higashiwaki, and G.H. Jessen, "Guest Editorial: The dawn of gallium oxide microelectronics," Applied Physics Letters **112**(6), 060401 (2018).

[19] Q. Liu, F. Jin, B. Li, and L. Geng, "Structure and band gap energy of CaSnO3 epitaxial films on LaAlO3 substrate," Journal of Alloys and Compounds **717**, 55–61 (2017).

[20] M.C.F. Alves, S. Boursicot, S. Ollivier, V. Bouquet, S. Députier, A. Perrin, I.T. Weber, A.G. Souza, I.M.G. Santos, and M. Guilloux-Viry, "Synthesis of SrSnO3 thin films by pulsed laser deposition: Influence of substrate and deposition temperature," Thin Solid Films **519**(2), 614–618 (2010).

[21] Q. Gao, K. Li, L. Zhao, K. Zhang, H. Li, J. Zhang, and Q. Liu, "Wide-Range Band-Gap Tuning and High Electrical Conductivity in La- and Pb-Doped $SrSnO_3$ Epitaxial Films," ACS Applied Materials & Interfaces **11**(28), 25605–25612 (2019).

[22] Z. Huang, D. Wang, R. Niu, and W. Wang, "Modulation of the band gap and enhancement of the third-order optical nonlinearity in vanadium-doped $SrSnO_3$ films," Journal of the Optical Society of America B **41**(4), 931–931 (2024).

[23] Q. Gao, H. Chen, K. Li, and Q. Liu, "Band Gap Engineering and Room-Temperature Ferromagnetism by Oxygen Vacancies in $SrSnO_3$ Epitaxial Films," ACS Applied Materials & Interfaces **10**(32), 27503–27509 (2018).

[24] D. Gao, X. Gao, Y. Wu, T. Zhang, J. Yang, and X. Li, "Co-doped SrSnO3 epitaxial thin films on MgO with tunable band gap and room-temperature ferromagnetism," Physica E: Low-Dimensional Systems and Nanostructures **109**, 101–106 (2019).

[25] X.-M. HU, X.-D. GAO, X.-M. LI, Z.-Y. GU, Y. SHI, and Y.-Q. WU, "Microstructure and Band Gap Modulation of $SrSn_{1-x}Co_xO_3$ Epitaxial Thin Films *via* Pulsed Laser Deposition," Acta Physico-Chimica Sinica **32**(4), 828–833 (2016).

[26] X. Hu, X. Gao, D. Gao, and X. Li, "Room-temperature ferromagnetism and oxygen pressure-dependent optical, ferromagnetic properties in $SrSn_{0.5}Co_{0.5}O_3$ thin films," Materials Research Letters **6**(5), 276–282 (2018).

[27] E. Baba, D. Kan, Y. Yamada, Mitsutaka Haruta, H. Kurata, Y. Kanemitsu, and Yuichi Shimakawa, "Optical and transport properties of transparent conducting La-doped $SrSnO_3$thin films," Journal of Physics D Applied Physics **48**(45), 455106–455106 (2015).

[28] K. Li, Q. Gao, L. Zhao, and Q. Liu, "Electrical and Optical Properties of Nb-doped SrSnO3 Epitaxial Films Deposited by Pulsed Laser Deposition," Nanoscale Research Letters **15**(1), (2020).

[29] Q. Liu, J. Dai, X. Zhang, G. Zhu, Z. Liu, and G. Ding, "Perovskite-type transparent and conductive oxide films: Sb- and Nd-doped SrSnO3," Thin Solid Films **519**(18), 6059–6063 (2011).

[30] D.-P. Wang, R.-F. Niu, L.-Q. Cui, and W.-T. Wang, "Unusual Electrical Transport Characteristic of the SrSnO3/Nb-Doped SrTiO3 Heterostructure," Korean Journal of Materials Research **33**(6), 229–235 (2023).

[31] M. Wei, A.V. Sanchela, B. Feng, Yuichi Ikuhara, H.J. Cho, and H. Ohta, "High electrical conducting deep-ultraviolet-transparent oxide semiconductor La-doped SrSnO3 exceeding ∼3000 S cm−1," Applied Physics Letters **116**(2), (2020).

[32] J. Cui, Y. Zhang, J. Wang, Z. Zhao, H. Huang, W. Zou, M. Yang, R. Peng, W. Yan, Q. Huang, Z. Fu, and Y. Lu, "Oxygen deficiency induced strong electron localization in lanthanum doped transparent perovskite oxide BaSnO3," Physical Review. B./Physical Review. B **100**(16), (2019).

[33] P. Singh, A. Swartz, D. Lu, S.S. Hong, K. Lee, A.F. Marshall, K. Nishio, Y. Hikita, and H.Y. Hwang, "Large-Area Crystalline $BaSnO_3$ Membranes with High Electron Mobilities," ACS Applied Electronic Materials **1**(7), 1269–1274 (2019).

[34] A.P.N. Tchiomo, Emanuela Carleschi, Aletta R. E. Prinsloo, W. Sigle, P.A. Van Aken, Jochen Mannhart, Prosper Ngabonziza, and B.P. Doyle, "Combined spectroscopy and electrical characterization of La:BaSnO3 thin films and heterostructures," AIP Advances **12**(10), (2022).

[35] A.P. Nono Tchiomo, W. Braun, B.P. Doyle, W. Sigle, P. van Aken, J. Mannhart, and P. Ngabonziza, "High-temperature-grown buffer layer boosts electron mobility in epitaxial La-doped BaSnO3/SrZrO3 heterostructures," APL Materials **7**(4), (2019).

[36] P.V. Wadekar, J. Alaria, M. O'Sullivan, O. Flack, T.D. Manning, L.J. Phillips, K. Durose, O. Lozano, S. Lucas, J.B. Claridge, and M.J. Rosseinsky, "Improved electrical mobility in highly epitaxial La:BaSnO3 films on SmScO3(110) substrates," Applied Physics Letters **105**(5), (2014).

[37] C.A. Niedermeier, S. Rhode, S. Fearn, K. Ide, M.A. Moram, H. Hiramatsu, Hideo Hosono, and T. Kamiya, "Solid phase epitaxial growth of high mobility La:BaSnO3 thin films co-doped with interstitial hydrogen," Applied Physics Letters **108**(17), (2016).

[38] J. John, S.R. Chalana, R. Prabhu, and V.P. Mahadevan Pillai, "Effect of oxygen pressure on the structural and optical properties of BaSnO3 films prepared by pulsed laser deposition method," Applied Physics A **125**(3), (2019).

[39] J. John, S. Suresh, M. Sivakumar, K.G. Gopchandran, and V.P.M. Pillai, "Ni doping induced property enhancement in laser ablated BaSnO3 films suitable for optoelectronic applications," Heliyon **10**(5), e26688 (2024).

[40] H. Mun, U. Kim, H. Min Kim, C. Park, T. Hoon Kim, H. Joon Kim, K. Hoon Kim, and K. Char, "Large effects of dislocations on high mobility of epitaxial perovskite $Ba_{0.96}La_{0.04}SnO_3$ films," Applied Physics Letters **102**(25), 252105 (2013).

[41] K. Balamurugan, E.S. Kumar, B. Ramachandran, S. Venkatesh, N.H. Kumar, S. Ramachandra, and P.N. Santhosh, "Dielectric resonance and magnetic properties of Fe-3% doped BaSnO3 thin films grown by pulsed laser deposition," Journal of Applied Physics **111**(7), (2012).

[42] K.K. James, A. Aravind, and M.K. Jayaraj, "Structural, optical and magnetic properties of Fe-doped barium stannate thin films grown by PLD," Applied Surface Science **282**, 121–125 (2013).

[43] U.S. Alaan, P. Shafer, A.T. N'Diaye, E. Arenholz, and Y. Suzuki, "Gd-doped BaSnO3: A transparent conducting oxide with localized magnetic moments," Applied Physics Letters **108**(4), (2016).

[44] U.S. Alaan, F.J. Wong, J.J. Ditto, A.W. Robertson, E. Lindgren, A. Prakash, G. Haugstad, P. Shafer, A.T. N'Diaye, D. Johnson, E. Arenholz, Bharat Jalan, N.D. Browning, and Y. Suzuki, "Magnetism and transport in transparent high-mobility BaSnO3 films doped with La, Pr, Nd, and Gd," Physical Review Materials **3**(12), (2019).

[45] F.-Y. Fan, W.-Y. Zhao, T.-W. Chen, J.-M. Yan, J.-P. Ma, L. Guo, G.-Y. Gao, F.-F. Wang, and R.-K. Zheng, "Excellent structural, optical, and electrical properties of Nd-doped BaSnO3 transparent thin films," Applied Physics Letters **113**(20), (2018).

[46] D.-S. Gao, X.-D. Gao, Y.-Q. Wu, T.-T. Zhang, J.-N. Yang, and X.-M. Li, "Epitaxial Co doped BaSnO3 thin films with tunable optical bandgap on MgO substrate," Applied Physics A **125**(3), (2019).

[47] Q. Gao, K. Li, K. Zhang, J. Zhang, and Q. Liu, "Structure and bandgap nonlinearity in BaSn1−xTixO3 epitaxial films," Applied Physics Letters **114**(8), 081901 (2019).

[48] H. M. Iftekhar Jaim, S. Lee, X. Zhang, and I. Takeuchi, "Stability of the oxygen vacancy induced conductivity in BaSnO3 thin films on SrTiO3," Applied Physics Letters **111**(17), (2017).

[49] B. Kang, D.H. Tran, and W.N. Kang, "Scaling of pinning forces in BaSnO3-added GdBa2Cu3O7 − x superconducting thin films," Thin Solid Films **624**, 16–20 (2017).

[50] Kyung-Pil Ko, Soon-Mi Choi, Jung-Woo Lee, Rock-Kil Ko, Seung-Hyun Moon, Chan Park, and Sang-Im Yoo, "Optimization of the BaSnO3 Doping Content in GdBa2Cu3O7-delta Coated Conductors by Pulsed Laser Deposition," IEEE Transactions on Applied Superconductivity **24**(6), 1–8 (2014).

[51] T. Kotaki, Y. Uraguchi, T. Makihara, M. Suenaga, T. Sueyoshi, T. Fujiyoshi, F. Mitugi, and T. Ikegami, "Influence of nano-particle diameter on superconducting properties in BaMO3(M = Sn, Hf)/YBa2Cu3Oy quasi-multilayered films," Physica C: Superconductivity and Its Applications **518**, 63–68 (2015).

[52] A. Kumar, Sandeep Maurya, S. Chawla, S. Patwardhan, and Balasubramaniam Kavaipatti, "Effect of thickness on metal to semiconductor transition in La doped BaSnO3 films deposited on high mismatch LSAT substrates," Applied Physics Letters **114**(21), (2019).

[53] A. Kumar, Sandeep Maurya, S. Patwardhan, and K.R. Balasubramaniam, "Opto-electronic properties of poly-crystalline La doped $BaSnO_3$ films deposited on quartz substrates," Journal of Physics D Applied Physics **54**(18), 185108–185108 (2021).

[54] J.H. Lee, W.-J. Lee, T.H. Kim, T. Lee, S. Hong, and K.H. Kim, "Transparent*p*-CuI/*n*-$BaSnO_{3-\delta}$heterojunctions with a high rectification ratio," Journal of Physics Condensed Matter **29**(38), 384004–384004 (2017).

[55] W.-J. Lee, H.J. Kim, E. Sohn, T.H. Kim, J.-Y. Park, W. Park, H. Jeong, T. Lee, J.H. Kim, K.-Y. Choi, and K.H. Kim, "Enhanced electron mobility in epitaxial (Ba,La)SnO3 films on BaSnO3(001) substrates," Applied Physics Letters **108**(8), (2016).

[56] Q. Liu, J. Liu, B. Li, H. Li, G. Zhu, K. Dai, Z. Liu, P. Zhang, and J. Dai, "Composition dependent metal-semiconductor transition in transparent and conductive La-doped $BaSnO_3$epitaxial films," Applied Physics Letters **101**(24), 241901 (2012).

[57] Q. Liu, B. Li, J. Liu, H. Li, Z. Liu, K. Dai, G. Zhu, P. Zhang, F. Chen, and J. Dai, "Structure and band gap tuning of transparent $(Ba_{1-x}Sr_x)SnO_3$ thin films epitaxially grown on MgO substrates," EPL (Europhysics Letters) **98**(4), 47010–47010 (2012).

[58] P. Mele, K. Matsumoto, A. Ichinose, Masashi Mukaida, Y. Yoshida, S. Horii, and R. Kita, "Systematic study of the $BaSnO_3$insertion effect on the properties of $YBa_2Cu_3O_{7-x}$films prepared by pulsed laser ablation," Superconductor Science and Technology **21**(12), 125017–125017 (2008).

[59] Y. Ozaki, D. Kan, and Y. Shimakawa, "Influence of cation off-stoichiometry on structural and transport properties of (Ba,La)SnO3 epitaxial thin films grown by pulsed laser deposition," Journal of Applied Physics **121**(21), (2017).

[60] D. Pfützenreuter, M. Zupancic, Z. Galazka, R. Schewski, A. Dittmar, K. Irmscher, M. Albrecht, and J. Schwarzkopf, "Epitaxial $BaSnO_3$ thin films with low dislocation density grown on lattice matched $LaInO_3$ substrates," Nanotechnology **32**(50), 505609–505609 (2021).

[61] J. Shin, J. Lim, T. Ha, Y.M. Kim, C. Park, J. Yu, J.H. Kim, and K. Char, "Band gap and mobility of epitaxial perovskite BaSn1−xHfxO3 thin films," Physical Review Materials **2**(2), (2018).

[62] S. Shrivastava, D. Mahana, S. Nehra, S. Gangwar, S. Singh, C.S. Yadav, S.K. Muthusamy, and A. Dogra, "CO gas sensing characteristics of BaSnO3 epitaxial films prepared by PLD: The effect of film thickness," Sensors and Actuators B: Chemical **400**, 134882 (2023).

[63] S. Shrivastava, K. Kumar, A. Yadav, S. Nehra, S. Srivastava, P. Singh, M. Kumar, G. Gupta, and A. Dogra, "Unraveling the Thickness-Dependent High Photoconductivity in BaSnO3 Thin Films: Insights from Ultrafast Charge Carrier Dynamics," Journal of Physics D Applied Physics **58**(10), (2024).

[64] S. Soltani, S. Hong, B. Kim, D. Kim, J.K. Jung, B. Sohn, T.W. Noh, K. Char, and C. Kim, "2×2R45∘ surface reconstruction and electronic structure of BaSnO3 film," Physical Review Materials **4**(5), (2020).

[65] Y. Tanaka, M. Mukaida, R. Teranishi, K. Yamada, A. Ichinose, K. Matsumoto, S. Horii, Y. Yoshida, R. Kita, T. Fujiyoshi, and N. Mori, "Fabrication and characterization of BaSnO3-doped NdBa2Cu3O7−δ thin film," Physica C: Superconductivity **468**(15-20), 1864–1868 (2008).

[66] H. Takashima, and Y. Inaguma, "Near-infrared luminescence in perovskite $BaSnO_3$ epitaxial films," Applied Physics Letters **111**(9), 091903 (2017).

[67] D.H. Tran, W. B. K. Putri, B. Kang, N.H. Lee, and W.N. Kang, "A close correlation between nanostructure formations and the thickness dependence of the critical current density in pure and BaSnO3-added GdBa2Cu3O7-δ films," Journal of Applied Physics **115**(16), (2014).

[68] K. Yamada, A. Ichinose, S. Yasunaga, R. Teranishi, Masashi Mukaida, S. Horii, R. Kita, S. Kato, Y. Yoshida, K. Matsumoto, and S. Toh, "Transmission Electron Microscopy Analysis of Nanorods in $BaSnO_3$-Doped $ErBa_2Cu_3O_{7-\delta}$ Films," Japanese Journal of Applied Physics **47**(2R), 899–899 (2008).

[69] S. Yasunaga, M. Mukaida, A. Ichinose, S. Horii, R. Teranishi, K. Yamada, K. Matsumoto, R. Kita, Y. Yoshida, and N. Mori, "Growth of BaSnO3 doped ErBa2Cu3O7−δ thin films for high JC applications," Physica C: Superconductivity **468**(15-20), 1858–1860 (2008).

[70] A. Stadler, "Transparent Conducting Oxides—An Up-To-Date Overview," Materials **5**(12), 661–683 (2012).

[71] M.C.F. Alves, M.R. Nascimento, S.J.G. Lima, P.S. Pizani, J.W.M. Espinosa, E. Longo, L.E.B. Soledade, A.G. Souza, and I.M.G. Santos, "Influence of synthesis conditions on carbonate entrapment in perovskite SrSnO3," Materials Letters **63**(1), 118–120 (2008).

[72] M.C.F. Alves, S.C. Souza, G. Lima, E. Longo, A.G. Souza, and Santos, "Influence of the precursor salts in the synthesis of CaSnO3 by the polymeric precursor method," Journal of Thermal Analysis and Calorimetry **87**(3), 763–766 (2007).

[73] A.-M. Azad, M. Hashim, S. Baptist, A. Badri, and A.U. Haq, "Phase Evolution and Microstructural Development in sol-gel derived MSnO3 (M = Ca, Sr, and Ba)," Journal of Materials Science **35**(21), 5475–5483 (2000).

[74] J. Goethals, Chloé Fourdrin, M. Tarrida, A. Bedidi, Frédéric Hatert, and S. Rossano, "Structural investigations of neodymium incorporation in calcium stannate perovskite CaSnO3," Physics and Chemistry of Minerals **46**(2), 143–155 (2018).

[75] K. Beppu, Fumiya Funatomi, H. Adachi, and T. Wada, "Fabrication of antiferroelectric $NaNbO_3$-$CaSnO_3$ film by pulsed laser deposition," Japanese Journal of Applied Physics **60**(SF), SFFB01–SFFB01 (2021).

[76] A. Azad, L. Liew, and M.A. Alim, "The AC electrical characterization of the solid-state reaction derived CaSnO3," Journal of Materials Science **34**(14), 3375–3396 (1999).

[77] Y. Karabulut, M. Ayvacıklı, A. Canimoglu, J. Garcia Guinea, Z. Kotan, E. Ekdal, O. Akyuz, and N. Can, "Synthesis and Luminescence Properties of Trivalent Rare-Earth Element-Doped Calcium Stannate Phosphors," Spectroscopy Letters **47**(8), 630–641 (2014).

[78] K. Goto, Y. Nakachi, and K. Ueda, "Photoluminescence properties of Pr doped and Tb–Mg codoped CaSnO3 with perovskite structure," Thin Solid Films **516**(17), 5885–5889 (2008).

[79] Naoki Takani, and H. Yamane, "Structure analysis of $CaTi_{1-x}Sn_xO_3$ (x = 0.0–1.0) solid solutions," Powder Diffraction **29**(3), 254–259 (2014).

[80] D. Dijkkamp, T. Venkatesan, X.D. Wu, S.A. Shaheen, N. Jisrawi, Y.H. Min-Lee, W.L. McLean, and M. Croft, "Preparation of Y-Ba-Cu oxide superconductor thin films using pulsed laser evaporation from high$T_c$bulk material," Applied Physics Letters **51**(8), 619–621 (1987).

[81] N.A. Shepelin, Z.P. Tehrani, N. Ohannessian, C.W. Schneider, D. Pergolesi, and T. Lippert, "A practical guide to pulsed laser deposition," Chemical Society Reviews **52**(7), 2294–2321 (2023).

[82]Data Retrieved from the Materials Project for CaSnO3 (Mp-4438) from Database Version V2025.02.12.Post1., (2025).

[83]Data Retrieved from the Inorganic Crystal Structure Database (Retrieved August. 5th, 2024), (n.d.).

[84] R.D. Shannon, "Radii for La," Ic.ac.uk, (2025).

[85] R.D. Shannon, "Radii for Ca," Ic.ac.uk, (2025).

[86] M. Rizwan, S. Gul, T. Iqbal, U. Mushtaq, M.H. Farooq, M. Farman, R. Bibi, and M. Ijaz, "A review on perovskite lanthanum aluminate (LaAlO3), its properties and applications," Materials Research Express **6**(11), 112001 (2019).

[87] I. Fareed, H. Farooq, M.D. Khan, Z. Ali, and F.K. Butt, "Band gap engineering of Strontium Titanate (SrTiO3) for improved photocatalytic activity and excellent bio-sensing aptitude," Materials Science in Semiconductor Processing **177**, 108327–108327 (2024).

[88] J. Zhao, N.L. Ross, and R.J. Angel, "Tilting and distortion of CaSnO 3 perovskite to 7 GPa determined from single-crystal X-ray diffraction," Physics and Chemistry of Minerals **31**(5), 299–305 (2004).

[89] P.P. Balakrishnan, M.J. Veit, U.S. Alaan, M.T. Gray, and Y. Suzuki, "Metallicity in SrTiO3 substrates induced by pulsed laser deposition," APL Materials **7**(1), (2019).

[90] A. Barman, S. Chatterjee, C. Ou, Yau Yau Tse, N. Banerjee, Sohini Kar-Narayan, A. Datta, and D. Mukherjee, "Large electrocaloric effect in lead-free ferroelectric Ba0.85Ca0.15Ti0.9Zr0.1O3 thin film heterostructure," APL Materials **9**(2), (2021).

[91] K. Beppu, Fumiya Funatomi, H. Adachi, and T. Wada, "Fabrication of antiferroelectric $NaNbO_3$-$CaSnO_3$ film by pulsed laser deposition," Japanese Journal of Applied Physics **60**(SF), SFFB01–SFFB01 (2021).

[92] Anuradha Bhogra, Anha Masarrat, R. Meena, Dilruba Hasina, M. Bala, C.-L. Dong, C.-L. Chen, T. Som, A. Kumar, and Asokan Kandasami, "Tuning the Electrical and Thermoelectric Properties of N Ion Implanted SrTiO3 Thin Films and Their Conduction Mechanisms," Scientific Reports **9**(1), (2019).

[93] C. Bigi, P. Orgiani, A. Nardi, A. Troglia, J. Fujii, G. Panaccione, I. Vobornik, and G. Rossi, "Robustness of topological states in Bi2Se3 thin film grown by Pulsed Laser Deposition on (0 0 1)-oriented SrTiO3 perovskite," Applied Surface Science **473**, 190–193 (2019).

[94] A. Boileau, A. Cheikh, A. Fouchet, A. David, C. Labbé, P. Marie, F. Gourbilleau, and U. Lüders, "Tuning of the Optical Properties of the Transparent Conducting Oxide $SrVO_3$ by Electronic Correlations," Advanced Optical Materials **7**(7), (2019).

[95] A. Chatterjee, Z. Lan, Dennis Valbjørn Christensen, F. Bauitti, A. Morata, Emigdio Chavez-Angel, S. Sanna, I.E. Castelli, Y. Chen, A. Tarancon, and Nini Pryds, "On the thermoelectric properties of Nb-doped $SrTiO_3$ epitaxial thin films," Physical Chemistry Chemical Physics **24**(6), 3741–3748 (2022).

[96] L. Cheng, Y. Tang, Y. Zhu, and X. Ma, "Self-Recovery of Defective $PbTiO_3$ Film with Enhanced Piezoelectricity by Homogenizing Annealing," Crystal Growth & Design **20**(9), 5967–5973 (2020).

[97] A. Crespo, J. Gallenberger, M. De Santis, V. Langlais, F. Carla, J.M. Caicedo, J. Rius, and X. Torrelles, "Heteroepitaxial growth of anatase (0 0 1) films on SrTiO3 (0 0 1) by PLD and MBE," Applied Surface Science **632**, 157586 (2023).

[98] W. Dai, Y. Li, C. Jia, C. Kang, M. Li, and W. Zhang, "High-performance ferroelectric non-volatile memory based on La-doped BiFeO3 thin films," RSC Advances **10**(31), 18039–18043 (2020).

[99] D. Diaz-Fernandez, M. Spreitzer, T. Parkelj, and D. Suvorov, "Multi-stage pulsed laser deposition of high quality epitaxial ultra-thin SrTiO3 on Si substrates," Applied Surface Science **455**, 227–235 (2018).

[100] D. Diaz-Fernandez, M. Spreitzer, T. Parkelj, J. Kovač, and D. Suvorov, "The importance of annealing and stages coverage on the epitaxial growth of complex oxides on silicon by pulsed laser deposition," RSC Advances **7**(40), 24709–24717 (2017).

[101] G. Franceschi, M. Schmid, U. Diebold, and M. Riva, "Atomically resolved surface phases of $La_{0.8}Sr_{0.2}MnO_3$(110) thin films," Journal of Materials Chemistry A **8**(43), 22947–22961 (2020).

[102] M. Gal, K. Gadani, D. Dhruv, Z. Joshi, A. Zankat, B. Rajyaguru, A.D. Joshi, K. Asokan, P.S. Solanki, and N.A. Shah, "Thermionic emission driven resistive switching behaviour in Ca and Sr doped YMnO3 thin film devices," Solid State Communications **303-304**, 113737 (2019).

[103] Felix, C. Xu, F. Gunkel, and R. Dittmann, "Unraveling the enhanced Oxygen Vacancy Formation in Complex Oxides during Annealing and Growth," Scientific Reports **7**(1), (2017).

[104] Z.-Z. Jiang, Z. Guan, N. Yang, P.-H. Xiang, R.-J. Qi, R. Huang, P.-X. Yang, N. Zhong, and C.-G. Duan, "Epitaxial growth of BiFeO3 films on SrRuO3/SrTiO3," Materials Characterization **131**, 217–223 (2017).

[105] P. Jiao, J. Li, Z. Xi, X. Zhang, J. Wang, Y. Yang, Y. Deng, and D. Wu, "Ferroelectric Hf0.5Zr0.5O2 thin films deposited epitaxially on (110)-oriented SrTiO3," Applied Physics Letters **119**(25), (2021).

[106] K.T. Kang, H.I. Seo, O. Kwon, K. Lee, J.-S. Bae, M.-W. Chu, S.C. Chae, Y. Kim, and W.S. Choi, "Ferroelectricity in SrTiO3 epitaxial thin films via Sr-vacancy-induced tetragonality," Applied Surface Science **499**, 143930 (2020).

[107] T. KAWAGUCHI, T. KAWAI, T. HIRAIWA, N. SAKAMOTO, K. SHINOZAKI, H. SUZUKI, and N. WAKIYA, "Spontaneous superlattice formation and electrical properties of Sr-excess $SrTiO_3$ thin film deposited on $SrTiO_3$(101) by dynamic aurora pulsed laser deposition," Journal of the Ceramic Society of Japan **129**(7), 390–396 (2021).

[108] E.K. Ko, J. Mun, H.G. Lee, J. Kim, J. Song, S.H. Chang, T.H. Kim, S.B. Chung, M. Kim, L. Wang, and T.W. Noh, "Oxygen Vacancy Engineering for Highly Tunable Ferromagnetic Properties: A Case of $SrRuO_3$ Ultrathin Film with a $SrTiO_3$ Capping Layer," Advanced Functional Materials **30**(50), (2020).

[109] T. Kobayashi, H. Nakagawa, H. Ogawa, F. Nabeshima, and A. Maeda, "Anisotropy of upper critical fields and interface superconductivity in FeSe/$SrTiO_3$ grown by PLD," Journal of Physics: Condensed Matter **35**(41), 41LT01 (2023).

[110] T. Kobayashi, H. Ogawa, F. Nabeshima, and A. Maeda, "Interface superconductivity in FeSe thin films on SrTiO 3 grown by the PLD technique," Superconductor Science and Technology **35**(7), 07LT01 (2022).

[111] S. Kondo, T. Yamada, A.K. Tagantsev, P. Ma, J. Leuthold, P. Martelli, P. Boffi, M. Martinelli, M. Yoshino, and Takanori Nagasaki, "Large impact of strain on the electro-optic effect in (Ba, Sr)TiO3 thin films: Experiment and theoretical comparison," Applied Physics Letters **115**(9), (2019).

[112] G. Li, X. Li, Y. Chen, S. Jia, and X. Xu, "Epitaxial growth mechanism of perovskite (1 1 1) SrTiO3 on wurtzite (0 0 0 2) GaN with single unit-cell TiN buffer layers," Applied Surface Science **465**, 1055–1060 (2018).

[113] T. Li, M. Ye, Z. Sun, N. Zhang, W. Zhang, S. Inguva, C. Xie, L. Chen, Y. Wang, S. Ke, and H. Huang, "Origin of Ferroelectricity in Epitaxial Si-Doped HfO_2 Films," ACS Applied Materials & Interfaces **11**(4), 4139–4144 (2019).

[114] Y.M. Liang, X.K. Ning, Z.J. Wang, B. He, Y. Bai, X.G. Zhao, W. Liu, and Z.D. Zhang, "Charge Transfer, Orbital Reconstruction, and Induced Magnetic Coupling in Manganite/$BiFeO_3$ Heterostructures," The Journal of Physical Chemistry C **121**(31), 16810–16818 (2017).

[115] Y. Liu, Y. Qi, P. Zhou, C. Guan, H. Chen, J. Wang, Z. Ma, T. Zhang, and Y. Liu, "Mechanisms of resistive switching in $BiFeO_3$ thin films modulated by bottom electrode," Journal of Physics D: Applied Physics **51**(2), 025303 (2017).

[116] G. Liu, X. Li, Y. Wang, W. Liang, B. Liu, H. Feng, H. Yang, J. Zhang, and J. Sun, "Nanoscale domains of ordered oxygen-vacancies in LaCoO3 films," Applied Surface Science **425**, 121–129 (2017).

[117] H. Liu, J. Fan, F. Qian, Y. Ji, A. Rahman, R. Tang, L. Zhang, L. Ling, Y. Zhu, and H. Yang, "Two-dimensional magnetic interplay in the tensile-strained $LaCoO_3$ thin films," Physical Chemistry Chemical Physics **23**(8), 4912–4918 (2021).

[118] H. Lu, J. Lin, and H. Zheng, "Superior ferroelectric properties and fatigue resistance in Tb modified (BaCa)(ZrTi)O3 film grown on SrTiO3 prepared by pulsed laser deposition," Applied Surface Science **527**, 146892 (2020).

[119] Z. Lu, J. Liu, J. Feng, X. Zheng, L. Yang, C. Ge, K. Jin, Z. Wang, and R.-W. Li, "Synthesis of single-crystal La0.67Sr0.33MnO3 freestanding films with different crystal-orientation," APL Materials **8**(5), (2020).

[120] A. Magrasó, B. Ballesteros, R. Rodríguez-Lamas, M.F. Sunding, and J. Santiso, "Optimisation of growth parameters to obtain epitaxial Y-doped BaZrO3 proton conducting thin films," Solid State Ionics **314**, 9–16 (2017).

[121] G. Mattoni, A. Filippetti, N. Manca, P. Zubko, and A.D. Caviglia, "Charge doping and large lattice expansion in oxygen-deficient heteroepitaxial WO3," Physical Review Materials **2**(5), (2018).

[122] S. Muff, M. Fanciulli, A.P. Weber, N. Pilet, Z. Ristić, Z. Wang, N.C. Plumb, M. Radović, and J.H. Dil, "Observation of a two-dimensional electron gas at CaTiO3 film surfaces," Applied Surface Science **432**, 41–45 (2017).

[123] D. Mukherjee, Mahesh Hordagoda, D. Pesquera, D. Ghosh, J.L. Jones, P. Mukherjee, and Sarath Witanachchi, "Enhanced ferroelectric polarization in epitaxial (Pb1−xLax)," Physical Review **95**(17), (2017).

[124] M.D. Nguyen, E.P. Houwman, H. Yuan, B.J. Wylie-van Eerd, M. Dekkers, G. Koster, J.E. Ten Elshof, and G. Rijnders, "Controlling Piezoelectric Responses in $Pb(Zr_{0.52}Ti_{0.48})O_3$ Films through Deposition Conditions and Nanosheet Buffer Layers on Glass," ACS Applied Materials & Interfaces **9**(41), 35947–35957 (2017).

[125] J.A. Padilla, E. Xuriguera, L. Rodríguez, A. Vannozzi, M. Segarra, G. Celentano, and M. Varela, "Epitaxial Growth of SrTiO3 Films on Cube-Textured Cu-Clad Substrates by PLD at Low Temperature Under Reducing Atmosphere," Nanoscale Research Letters **12**(1), (2017).

[126] N. Palina, L. Wang, S. Dash, X. Yu, M.B.H. Breese, J. Wang, and A. Rusydi, "Investigation of the metal–insulator transition in $NdNiO_3$films by site-selective X-ray absorption spectroscopy," Nanoscale **9**(18), 6094–6102 (2017).

[127] G. Panchal, D.K. Shukla, R.J. Choudhary, V.R. Reddy, and D.M. Phase, "The effect of oxygen stoichiometry at the interface of epitaxial BaTiO3/La0.7Sr0.3MnO3 bilayers on its electronic and magnetic properties," Journal of Applied Physics **122**(8), (2017).

[128] W. Pei, J. Chen, D. You, Q. Zhang, M. Li, Y. Lu, Z. Fu, and Y. He, "Enhanced photovoltaic effect in Ca and Mn co-doped BiFeO3 epitaxial thin films," Applied Surface Science **530**, 147194–147194 (2020).

[129] A. Rastogi, M. Brahlek, J.M. Ok, Z. Liao, C. Sohn, S. Feldman, and H.N. Lee, "Metal-insulator transition in (111) $SrRuO_3$ ultrathin films," APL Materials **7**(9), 091106 (2019).

[130] P. Scheiderer, M. Schmitt, J. Gabel, M. Zapf, M. Stübinger, P. Schütz, L. Dudy, C. Schlueter, T. Lee, M. Sing, and R. Claessen, "Tailoring Materials for Mottronics: Excess Oxygen Doping of a Prototypical Mott Insulator," Advanced Materials **30**(25), (2018).

[131] C.W. Schneider, M. Döbeli, C. Richter, and T. Lippert, "Oxygen diffusion in oxide thin films grown on SrTiO3," Physical Review Materials **3**(12), (2019).

[132] A.P. Sharma, D.K. Pradhan, S.K. Pradhan, and M. Bahoura, "Large energy storage density performance of epitaxial BCT/BZT heterostructures via interface engineering," Scientific Reports **9**(1), (2019).

[133] S. Singh, A.L. Sangle, T. Wu, N. Khare, and J.L. MacManus-Driscoll, "Growth of Doped $SrTiO_3$ Ferroelectric Nanoporous Thin Films and Tuning of Photoelectrochemical Properties with Switchable Ferroelectric Polarization," ACS Applied Materials & Interfaces **11**(49), 45683–45691 (2019).

[134] H. Takashima, M. Cho, T. Taniyama, and M. Itoh, "Surface morphology and dielectric behavior of perovskite SrTiO 3 thin film in heterostructure electroluminescence devices," Current Applied Physics **17**(5), 657–660 (2017).

[135] J.G. Ulbrandt, X. Zhang, R.L. Headrick, R. Liu, M. Dawber, and K. Evans-Lutterodt, "Fast nonthermal processes in pulsed laser deposition," Physical Review B **101**(24), (2020).

[136] K. Wang, M.H. Tang, Y. Xiong, G. Li, Y.G. Xiao, W. L. Zhang, Z.P. Wang, Z. Li, and J. He, "Epitaxial growth and magnetic/transport properties of $La_{0.7}Sr_{0.3}MnO_3$ thin films grown on $SrTiO_3$ with optimized growth conditions," RSC Advances **7**(50), 31327–31332 (2017).

[137] L. Wang, S. Ju, L. You, Y. Qi, Y. Guo, P. Ren, Y. Zhou, and J. Wang, "Competition between strain and dimensionality effects on the electronic phase transitions in NdNiO3 films," Scientific Reports **5**(1), (2015).

[138] L. Wang, S. Dash, L. Chang, L. You, Y. Feng, X. He, K. Jin, Y. Zhou, H.G. Ong, P. Ren, S. Wang, L. Chen, and J. Wang, "Oxygen Vacancy Induced Room-Temperature Metal–Insulator Transition in Nickelate Films and Its Potential Application in Photovoltaics," ACS Applied Materials & Interfaces **8**(15), 9769–9776 (2016).

[139] L. Wang, L. Chang, X. Yin, L. You, J. Zhao, H. Guo, K. Jin, K. Ibrahim, J. Wang, Andrivo Rusydi, and J. Wang, "Self-powered sensitive and stable UV-visible photodetector based on GdNiO3/Nb-doped SrTiO3 heterojunctions," Applied Physics Letters **110**(4), (2017).

[140] T.-H. Wang, P.-C. (Brent) Hsu, M. Korytov, J. Genoe, and C. Merckling, "Polarization control of epitaxial barium titanate (BaTiO3) grown by pulsed-laser deposition on a MBE-SrTiO3/Si(001) pseudo-substrate," Journal of Applied Physics **128**(10), (2020).

[141] H. Wei, J.L. Barzola-Quiquia, C. Yang, C. Patzig, T. Höche, P. Esquinazi, M. Grundmann, and M. Lorenz, "Charge transfer-induced magnetic exchange bias and electron localization in (111)- and (001)-oriented LaNiO3/LaMnO3 superlattices," Applied Physics Letters **110**(10), (2017).

[142] J. Winiger, K. Keller, D. Moor, M. Baumann, D. Kim, D. Chelladurai, M. Kohli, T. Blatter, E. Dénervaud, Yuriy Fedoryshyn, U. Koch, S. Pané, R. Grange, and J. Leuthold, "PLD Epitaxial Thin-Film $BaTiO_3$ on MgO − Dielectric and Electro-Optic Properties," Advanced Materials Interfaces **11**(1), (2023).

[143] M. Zheng, X. Li, W. Xiao, W. Wang, and H. Ni, "Oxygen deficiency and cooling field driven vertical hysteretic shift in epitaxial SrRuO3/SrTiO3 heterostructures," Applied Physics Letters **111**(15), (2017).

[144] J. Zhu, J.-W. Lee, H. Lee, L. Xie, X. Pan, R.A. De, C.-B. Eom, and S.S. Nonnenmann, "Probing vacancy behavior across complex oxide heterointerfaces," Science Advances **5**(2), (2019).

[145] W. Abbas, D. Ho, and A. Pramanick, "High energy storage efficiency and thermal stability of A-site-deficient and 110-textured $BaTiO_3$–$BiScO_3$ thin films," Journal of the American Ceramic Society **103**(5), 3168–3177 (2020).

[146] N.Z. Abed, R.A. Ismail, and S.S. Shaker, "Role of substrate temperature on the performance of BaTiO3/Si photodetector prepared by pulsed laser deposition," Scientific Reports **14**(1), (2024).

[147] A. Aidoud, T. Maroutian, S. Matzen, G. Agnus, B. Amrani, K. Driss-Khodja, P. Aubert, and P. Lecoeur, "Tuning the growth and strain relaxation of ferroelectric $BaTiO_3$ thin films on $SrRuO_3$ electrode: influence on electrical properties," The European Physical Journal Applied Physics **80**(3), 30303 (2017).

[148] Pratik Bagul, H. Han, Pieter Lagrain, S. Sergeant, I. Hoflijk, J. Serron, O. Richard, T. Conard, J.V. Houdt, I.D. Wolf, and Sean, "Achieving High Ferroelectric Polarization in Ultrathin $BaTiO_3$ Films on Si," Advanced Electronic Materials **11**(4), (2024).

[149] S. Chatterjee, A. Barman, S. Barman, Tanmay Chabri, Sohini Kar-Narayan, A. Datta, and D. Mukherjee, "Role of oxygen vacancies on the low-temperature dielectric relaxor behavior in epitaxial Ba0.85Ca0.15Ti0.9Zr0.1," Physical Review Materials **5**(6), (2021).

[150] L. Dai, G. Niu, J. Zhao, Y. Xue, R. Luo, B. Chen, R. An, Y. Sun, B. Feng, S. Ding, W. Luo, Z.-G. Ye, and W. Ren, "Oxygen vacancy induced phase and conductivity transition of epitaxial BaTiO3−δ films directly grown on Ge (001) without surface passivation," Journal of Applied Physics **129**(4), (2021).

[151] X. Gao, L. Li, J. Jian, H. Wang, M. Fan, J. Huang, X. Wang, and H. Wang, "Vertically Aligned Nanocomposite $BaTiO_3$:$YMnO_3$ Thin Films with Room Temperature Multiferroic Properties toward Nanoscale Memory Devices," ACS Applied Nano Materials **1**(6), 2509–2514 (2018).

[152] S. Hohenberger, V. Lazenka, S. Selle, C. Patzig, Kristiaan Temst, and M. Lorenz, "Magnetoelectric Coupling in Epitaxial Multiferroic $BiFeO_3$–$BaTiO_3$ Composite Thin Films," Physica Status Solidi (B) Basic Solid State Physics **257**(7), (2020).

[153] Y. Hu, Q. Xie, R. Liang, X. Zhao, Z. Zhou, X. Dong, F. Wang, Y. Tang, N. Liu, and X. Liu, "High energy storage performance in lead-free BiFeO3-BaTiO3 ferroelectric thin film fabricated by pulsed laser deposition," AIP Advances **9**(8), (2019).

[154] A.A. Instan, S.P. Pavunny, M.K. Bhattarai, and R.S. Katiyar, "Ultrahigh capacitive energy storage in highly oriented Ba(ZrxTi1-x)O3 thin films prepared by pulsed laser deposition," Applied Physics Letters **111**(14), (2017).

[155] S. Kondo, T. Murakami, L. Pichon, J. Leblanc-Lavoie, T. Teranishi, A. Kishimoto, and M.A. El Khakani, "Colossal Dielectric Constant of Nanocrystalline/Amorphous Homo-Composite BaTiO3 Films Deposited via Pulsed Laser Deposition Technique," Nanomaterials **14**(20), 1677 (2024).

[156] A. Li, Q. Li, C. Jia, and W. Zhang, "Control of resistive switching type in BaTiO3 thin films grown by high and low laser fluence," Applied Physics Letters **122**(23), (2023).

[157] J. Liu, Y. Feng, R. Tang, R. Zhao, J. Gao, D. Shi, and H. Yang, "Mechanically Tunable Magnetic Properties of Flexible $SrRuO_3$ Epitaxial Thin Films on Mica Substrates," Advanced Electronic Materials **4**(4), (2018).

[158] J. Lyu, S. Estandía, J. Gazquez, M.F. Chisholm, I. Fina, N. Dix, J. Fontcuberta, and F. Sánchez, "Control of Polar Orientation and Lattice Strain in Epitaxial $BaTiO_3$ Films on Silicon," ACS Applied Materials & Interfaces **10**(30), 25529–25535 (2018).

[159] Y. Noguchi, and H. Matsuo, "Polarization and Dielectric Properties of BiFeO3-BaTiO3 Superlattice-Structured Ferroelectric Films," Nanomaterials **11**(7), 1857 (2021).

[160] B.K. Pandey, T.N. Bhat, B. Roul, K.K. Nanda, and S.B. Krupanidhi, "BTO/GaN heterostructure based on Schottky junction for high-temperature selective ultra-violet photo detection," Journal of Physics D: Applied Physics **51**(4), 045104 (2018).

[161] A. Piorra, V. Hrkac, N. Wolff, C. Zamponi, V. Duppel, J. Hadermann, L. Kienle, and E. Quandt, "(Ba0.85Ca0.15)(Ti0.9Zr0.1)O3 thin films prepared by PLD: Relaxor properties and complex microstructure," Journal of Applied Physics **125**(24), (2019).

[162] T. Ruf, S. Merker, F. Syrowatka, P. Trempler, G. Schmidt, M. Lorenz, M. Grundmann, and R. Denecke, "Preferential growth of perovskite $BaTiO_3$ thin films on $Gd_3Ga_5O_{12}$(100) and $Y_3Fe_5O_{12}$(100) oriented substrates by pulsed laser deposition," Materials Advances **3**(12), 4920–4931 (2022).

[163] Yeong Jae Shin, L. Wang, Y. Kim, H.-H. Nahm, D. Lee, Jeong Rae Kim, Sang Mo Yang, J.-G. Yoon, J.-S. Chung, M. Kim, Seo Hyoung Chang, and Tae Won Noh, "Oxygen Partial Pressure during Pulsed Laser Deposition: Deterministic Role on Thermodynamic Stability of Atomic Termination Sequence at $SrRuO_3/BaTiO_3$ Interface," ACS Applied Materials & Interfaces **9**(32), 27305–27312 (2017).

[164] Y. Song, X. Liu, F. Wen, M. Kareev, R. Zhang, Y. Pei, J. Bi, P. Shafer, A.T. N'Diaye, E. Arenholz, S.Y. Park, Y. Cao, and J. Chakhalian, "Unconventional crystal-field splitting in noncentrosymmetric BaTiO3 thin films," Physical Review Materials **4**(2), (2020).

[165] Z. Sun, S. Huang, W. Zhu, Y.A. Birkhölzer, X. Gao, R.A. Avila, H. Huang, X. Lou, E.P. Houwman, M.D. Nguyen, G. Koster, and Guus Rijnders, "Structure evolution of the interfacial layer of BaTiO3 thin films during annealing process and related good resistive switching behaviors," APL Materials **11**(10), (2023).

[166] A. Zhang, Q. Li, D. Gao, M. Guo, J. Feng, Z. Fan, D. Chen, M. Zeng, X. Gao, G. Zhou, X. Lu, and J-M. Liu, "Conductivity, charge transport, and ferroelectricity of La-doped $BaTiO_3$ epitaxial thin films," Journal of Physics D: Applied Physics **53**(2), 025301 (2019).

[167] A. Zhang, Q. Li, D. Gao, M. Guo, J. Feng, M. Zeng, Z. Fan, D. Chen, X. Gao, G. Zhou, X. Lu, and J-M. Liu, "Strain effects on conductivity and charge transport in La-doped $BaTiO_3$ thin films," Journal of Physics D Applied Physics **53**(7), 075305–075305 (2019).

[168] D. Zhang, S. Misra, L. Li, X. Wang, J. Jian, P. Lu, X. Gao, X. Sun, Z. Qi, Matias Kalaswad, X. Zhang, and H. Wang, "Tunable Optical Properties in Self-Assembled Oxide-Metal Hybrid Thin Films via Au-Phase Geometry Control: From Nanopillars to Nanodisks," Advanced Optical Materials **8**(4), (2019).

[169] G. Zhong, F. An, Yugandhar Bitla, J. Wang, X. Zhong, J. Yu, W. Gao, Y. Zhang, C. Tan, Y. Ou, J. Jiang, Y.-H. Hsieh, X. Pan, S. Xie, Y.-H. Chu, and J. Li, "Deterministic, Reversible, and Nonvolatile Low-Voltage Writing of Magnetic Domains in Epitaxial $BaTiO_3/Fe_3O_4$ Heterostructure," ACS Nano **12**(9), 9558–9567 (2018).

[170] S. Kong, L. Li, Z. Lu, J. Feng, X. Zheng, P. Song, Y. Shi, Y. Wang, B. Ge, K. Rolfs, E. Pomjakushina, T. Schmitt, N.C. Plumb, M. Shi, Z. Zhong, M. Radovic, Z. Wang, and R.-W. Li, "Isostructural metal-insulator transition driven by dimensional-crossover in SrIrO3 heterostructures," Physical Review Materials **6**(3), (2022).

[171] T. Orvis, Mythili Surendran, Y. Liu, A. Cunniff, and J. Ravichandran, "*In situ* Auger electron spectroscopy of complex oxide surfaces grown by pulsed laser deposition," Journal of Vacuum Science & Technology a Vacuum Surfaces and Films **37**(6), (2019).

[172] S. Al-Khateeb, D. Pavlopoulos, T.W. Button, and J.S. Abell, "Pulsed Laser Deposition of YBa2Cu3O7 Superconducting Film on MgO Templates Spray Pyrolyzed on Hastelloy C276," Journal of Superconductivity and Novel Magnetism **25**(6), 1823–1827 (2012).

[173] R. Arpaia, E. Andersson, Edoardo Trabaldo, T. Bauch, and F. Lombardi, "Probing the phase diagram of cuprates with YBa2Cu3O7−δ thin films and nanowires," Physical Review Materials **2**(2), (2018).

[174] A. Augieri, G. Celentano, V. Galluzzi, A. Mancini, A. Rufoloni, A. Vannozzi, A.A. Armenio, T. Petrisor, L. Ciontea, S. Rubanov, E. Silva, and N. Pompeo, "Pinning analyses on epitaxial YBa2Cu3O7−δ films with BaZrO3 inclusions," Journal of Applied Physics **108**(6), (2010).

[175] M.S. Bhuiyan, M Paranthaman, S Sathyamurthy, T Aytug, S. Kang, D.F. Lee, A. Goyal, E.A. Payzant, and K. Salama, "MOD approach for the growth of epitaxial CeO_2buffer layers on biaxially textured Ni–W substrates for YBCO coated conductors," Superconductor Science and Technology **16**(11), 1305–1309 (2003).

[176] T.A. Campbell, T.J. Haugan, I. Maartense, J. Murphy, L. Brunke, and P.N. Barnes, "Flux pinning effects of Y2O3 nanoparticulate dispersions in multilayered YBCO thin films," Physica C: Superconductivity **423**(1-2), 1–8 (2005).

[177] M. Coll, J. Gàzquez, R. Hühne, B. Holzapfel, Y. Morilla, J. García-López, A. Pomar, F. Sandiumenge, T. Puig, and X. Obradors, "All chemical $YBa_2Cu_3O_7$ superconducting multilayers: Critical role of CeO_2 cap layer flatness," Journal of Materials Research **24**(4), 1446–1455 (2009).

[178] A. Crisan, V.S. Dang, and P. Mikheenko, "Nano-engineered pinning centres in YBCO superconducting films," Physica C: Superconductivity and Its Applications **533**, 118–132 (2016).

[179] K Develos-Bagarinao, and H. Yamasaki, "Microstructural defects associated with enhanced magnetic flux pinning in YBCO/DyBCO/YBCO multilayered thin films," Superconductor Science and Technology **24**(6), 065017–065017 (2011).

[180] S.R. Foltyn, P. Tiwari, R.C. Dye, M.Q. Le, and X.D. Wu, "Pulsed laser deposition of thick YBa2Cu3O7−δ films with $J_c \geq 1$ MA/cm2," Applied Physics Letters **63**(13), 1848–1850 (1993).

[181] D.K. Fork, D.B. Fenner, A. Barrera, J.M. Phillips, T.H. Geballe, G.A.N. Connell, and J.B. Boyce, "Buffer layers for high-quality epitaxial YBCO films on Si," IEEE Transactions on Applied Superconductivity **1**(1), 67–73 (1991).

[182] D.K. Fork, K. Nashimoto, and T.H. Geballe, "Epitaxial YBa2Cu3O7−δ on GaAs(001) using buffer layers," Applied Physics Letters **60**(13), 1621–1623 (1992).

[183] V. Galluzzi, A. Augieri, L. Ciontea, G. Celentano, F. Fabbri, U. Gambardella, A. Mancini, T. Petrișor, N. Pompeo, A. Rufoloni, E. Silva, and A. Vannozzi, "${\rm YBa}_{2}{\rm Cu}_{3}{\rm O}_{7-\delta}$ Films With ${\rm BaZrO}_{3}$ Inclusions for Strong-Pinning in Superconducting Films on Single Crystal Substrate," IEEE Transactions on Applied Superconductivity **17**(2), 3628–3631 (2007).

[184] T. Kotaki, Y. Uraguchi, T. Makihara, M. Suenaga, T. Sueyoshi, T. Fujiyoshi, F. Mitugi, and T. Ikegami, "Influence of nano-particle diameter on superconducting properties in BaMO3(M = Sn, Hf)/YBa2Cu3Oy quasi-multilayered films," Physica C: Superconductivity and Its Applications **518**, 63–68 (2015).

[185] J.B. Nelson, and D.P. Riley, "An experimental investigation of extrapolation methods in the derivation of accurate unit-cell dimensions of crystals," Proceedings of the Physical Society **57**(3), 160–177 (1945).

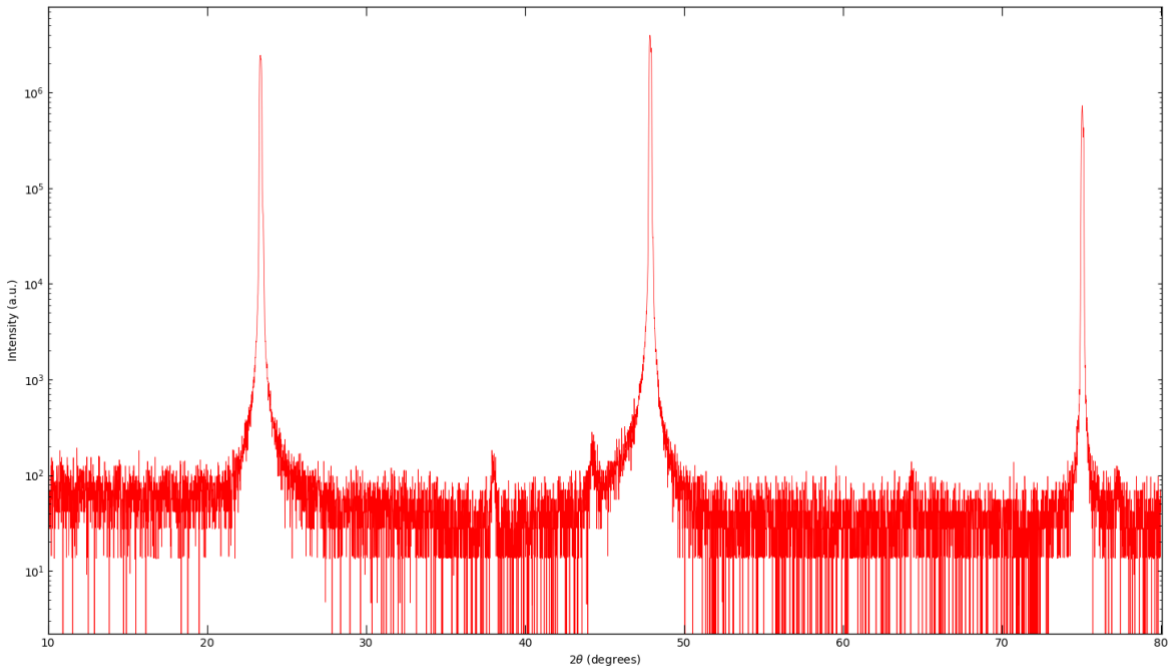

Figure A17: XRD 2θ plot of undoped CSO sample grown at 100mTorr and 650°C on LAO.

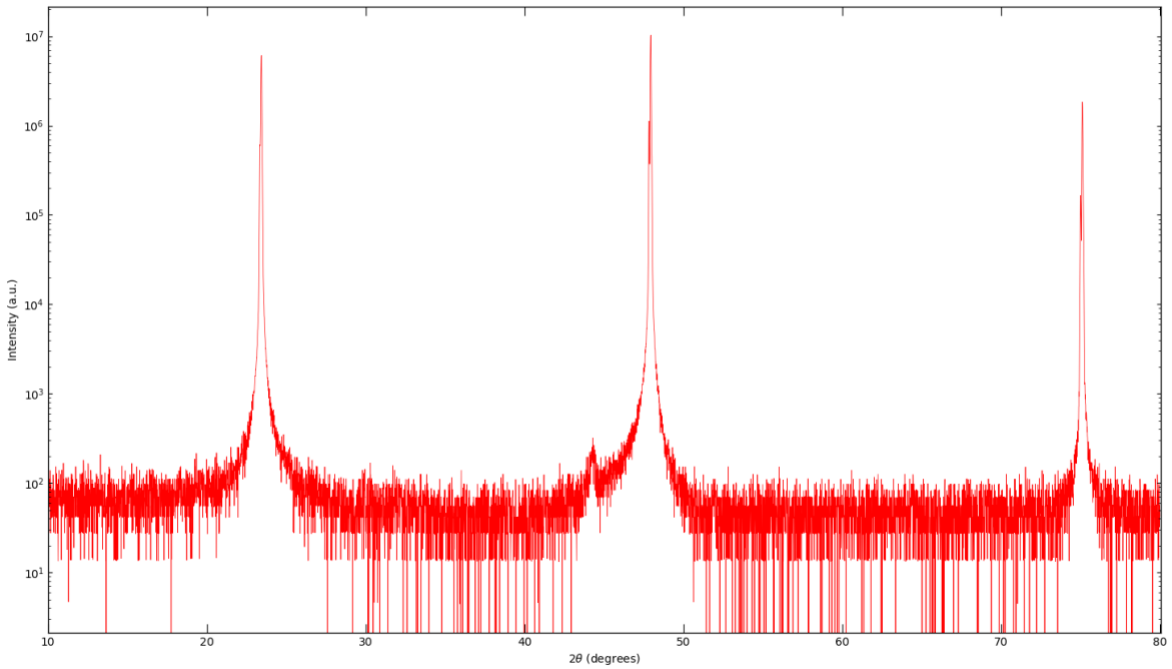

Figure A18: XRD 2θ plot of undoped CSO sample grown at 150mTorr and 650°C on LAO.

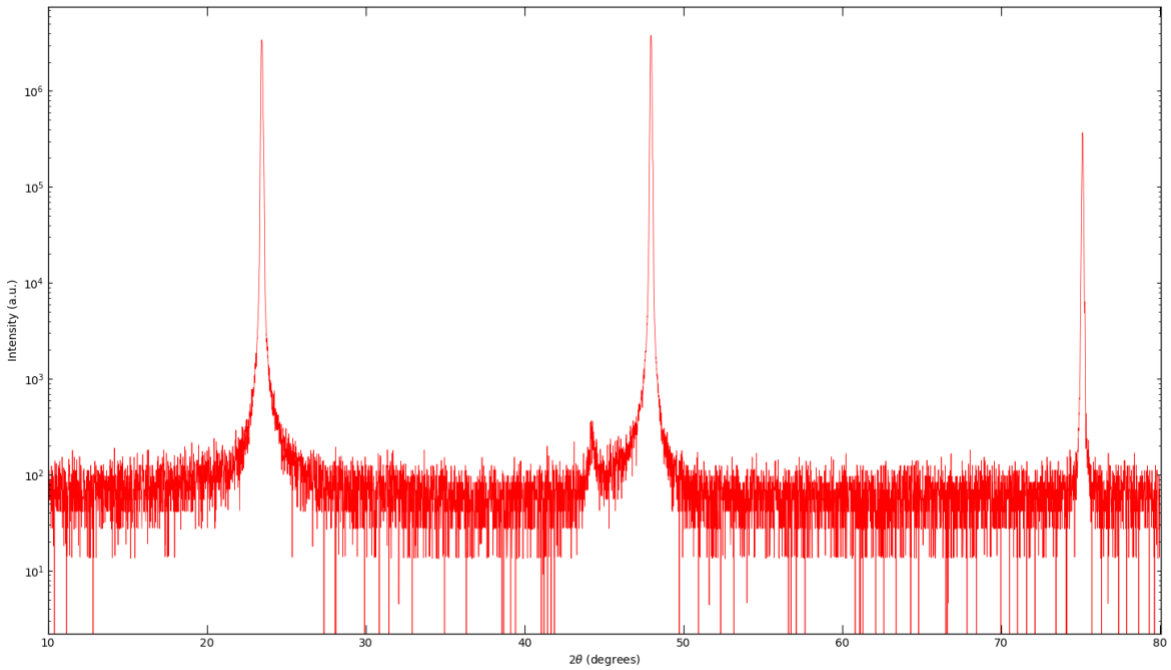

Figure A19: XRD 2θ plot of undoped CSO sample grown at 200mTorr and 650°C on LAO.

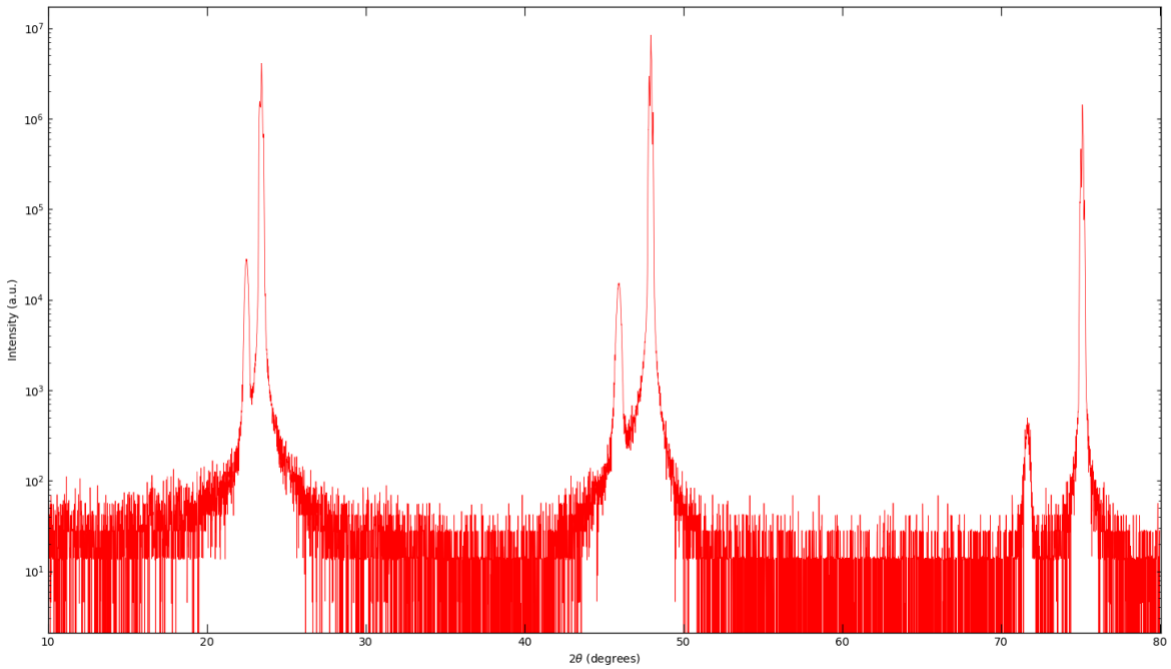

Figure A20: XRD 2θ plot of undoped CSO sample grown at 100mTorr and 750°C on LAO.

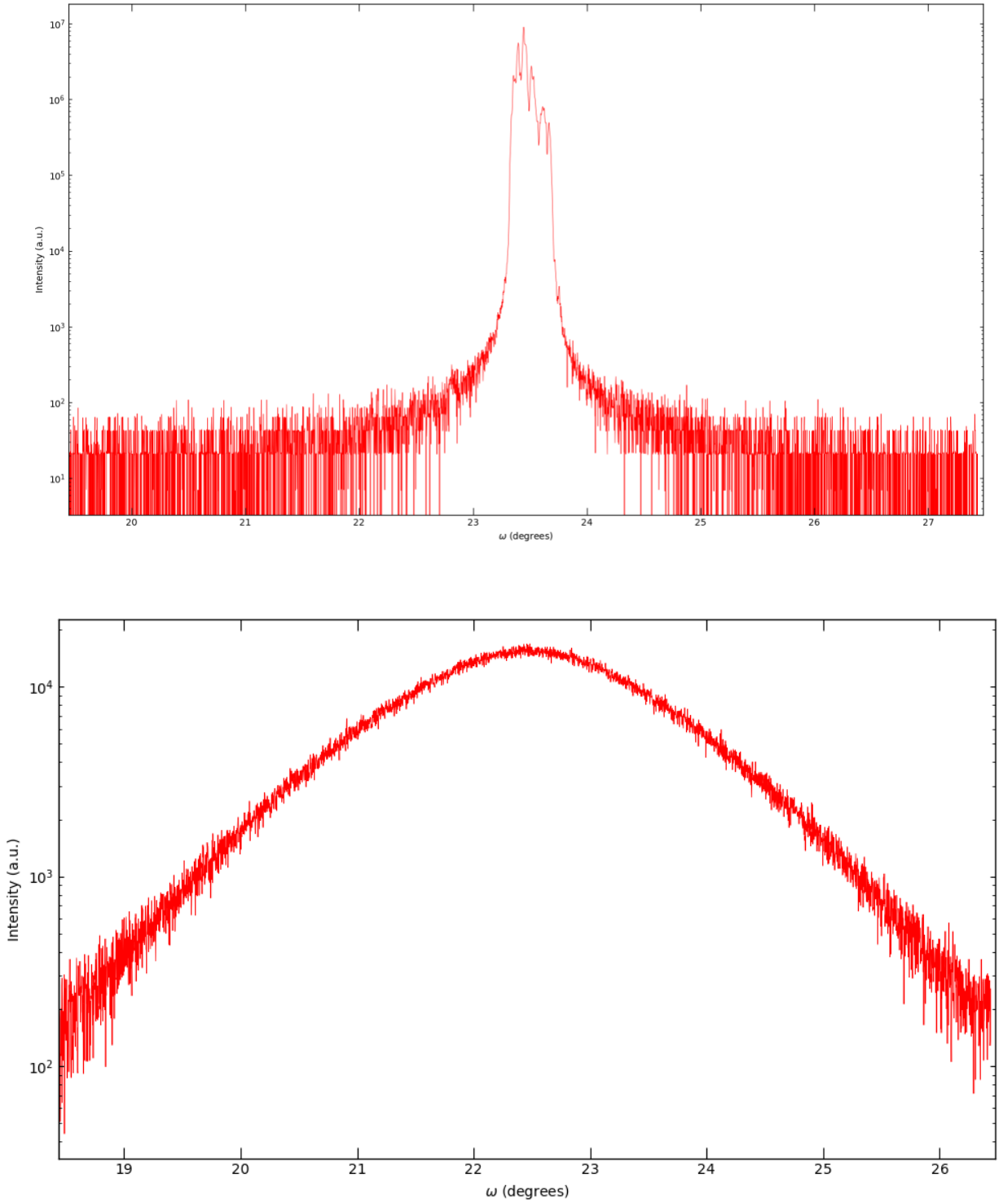

Figure A21: ω rocking curve of substrate (top) and film (bottom) of undoped CSO sample grown at 100mTorr and 750°C on LAO. $FWHM_{film} = 2.34°$

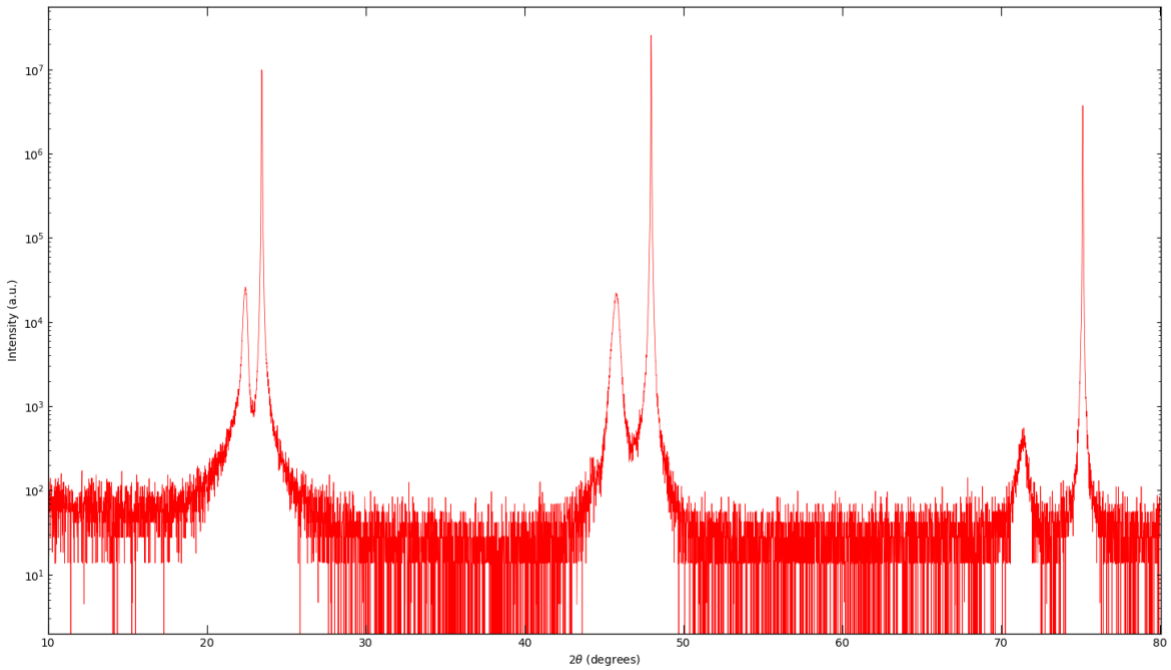

Figure A22: XRD 2θ plot of undoped CSO sample grown at 150mTorr and 750°C on LAO.

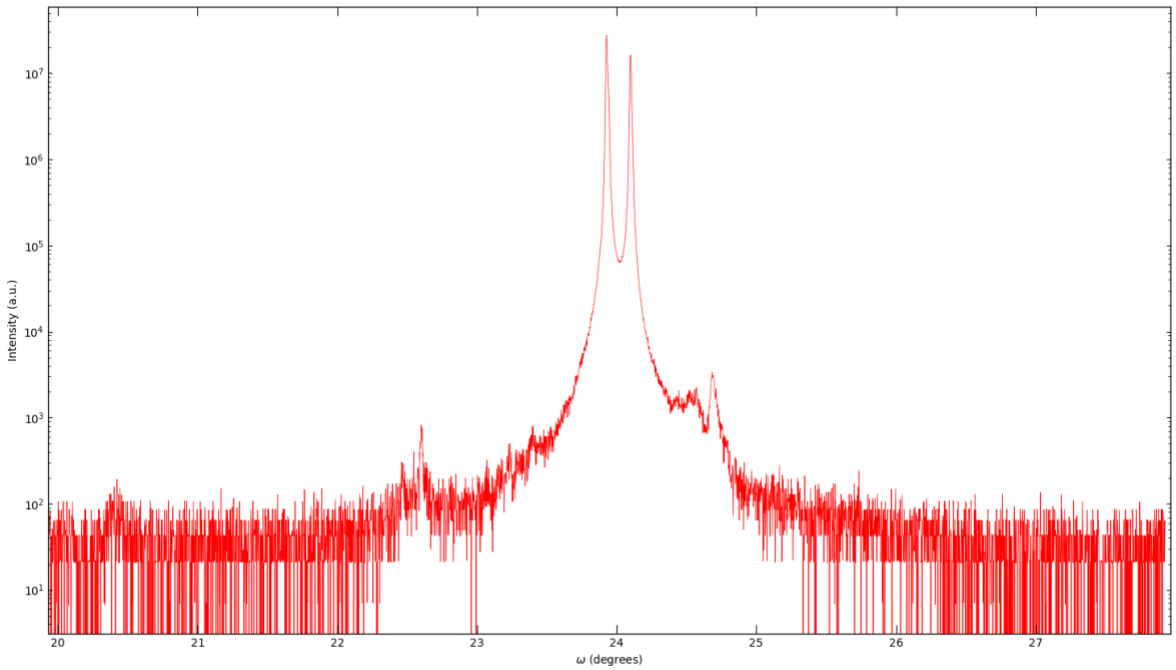

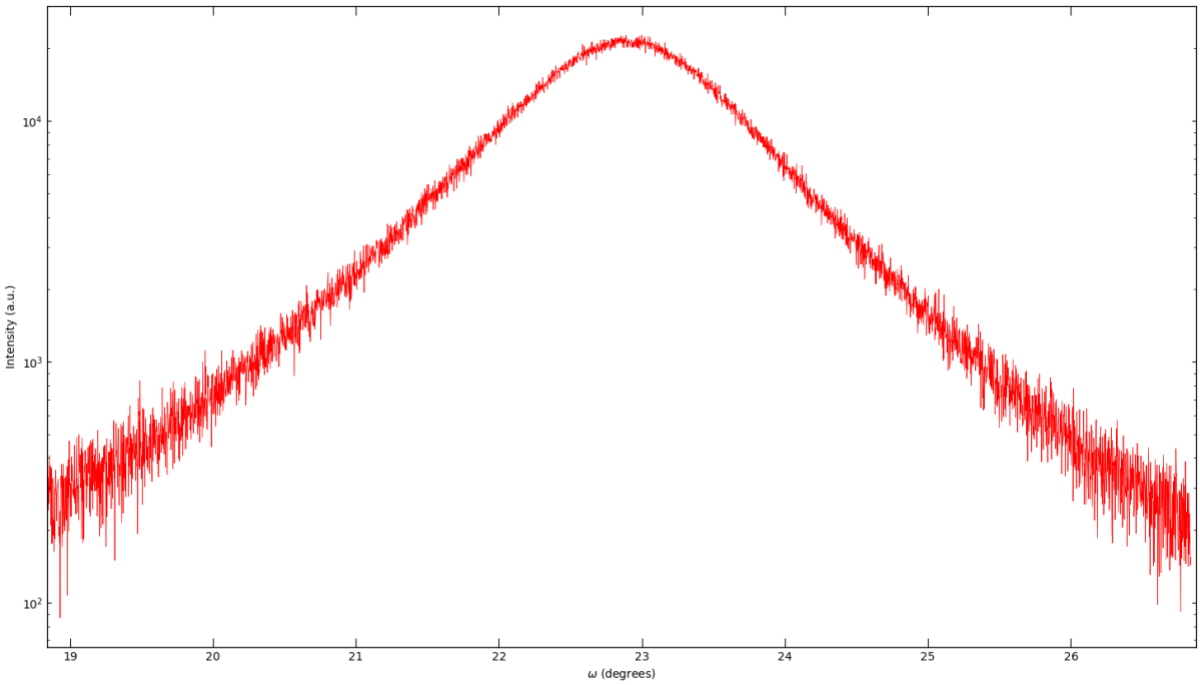

Figure A23: ω rocking curve of substrate (top) and film (bottom) of undoped CSO sample grown at 150mTorr and 750°C on LAO. $FWHM_{film} = 1.559°$

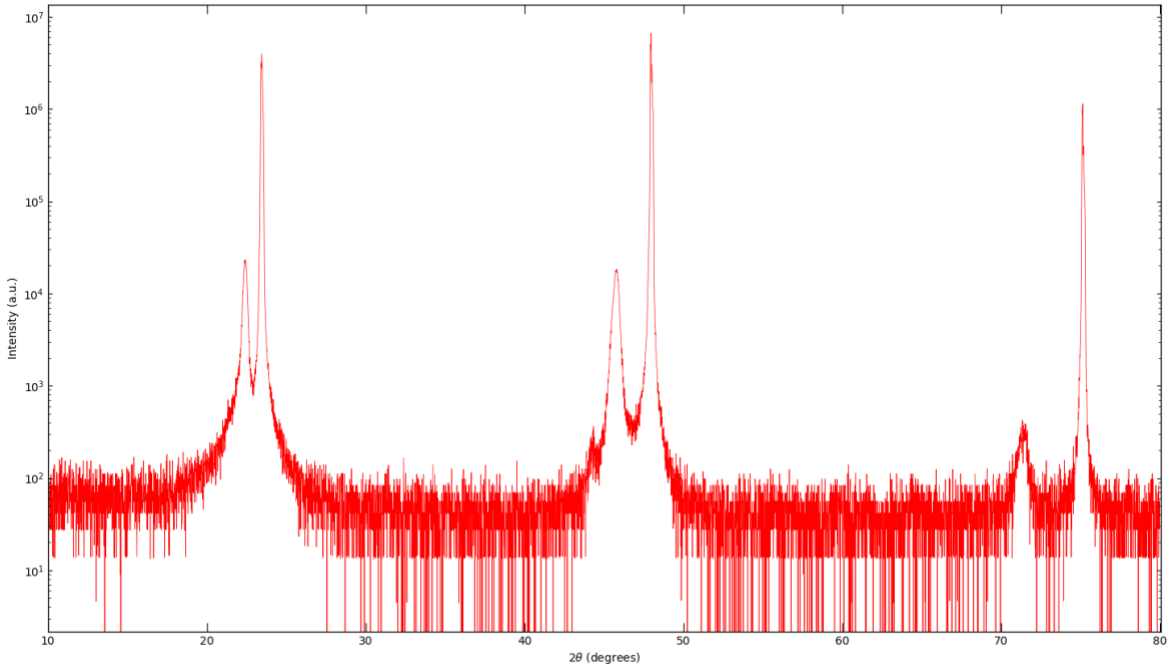

Figure A24: XRD 2θ plot of undoped CSO sample grown at 200mTorr and 750°C on LAO.

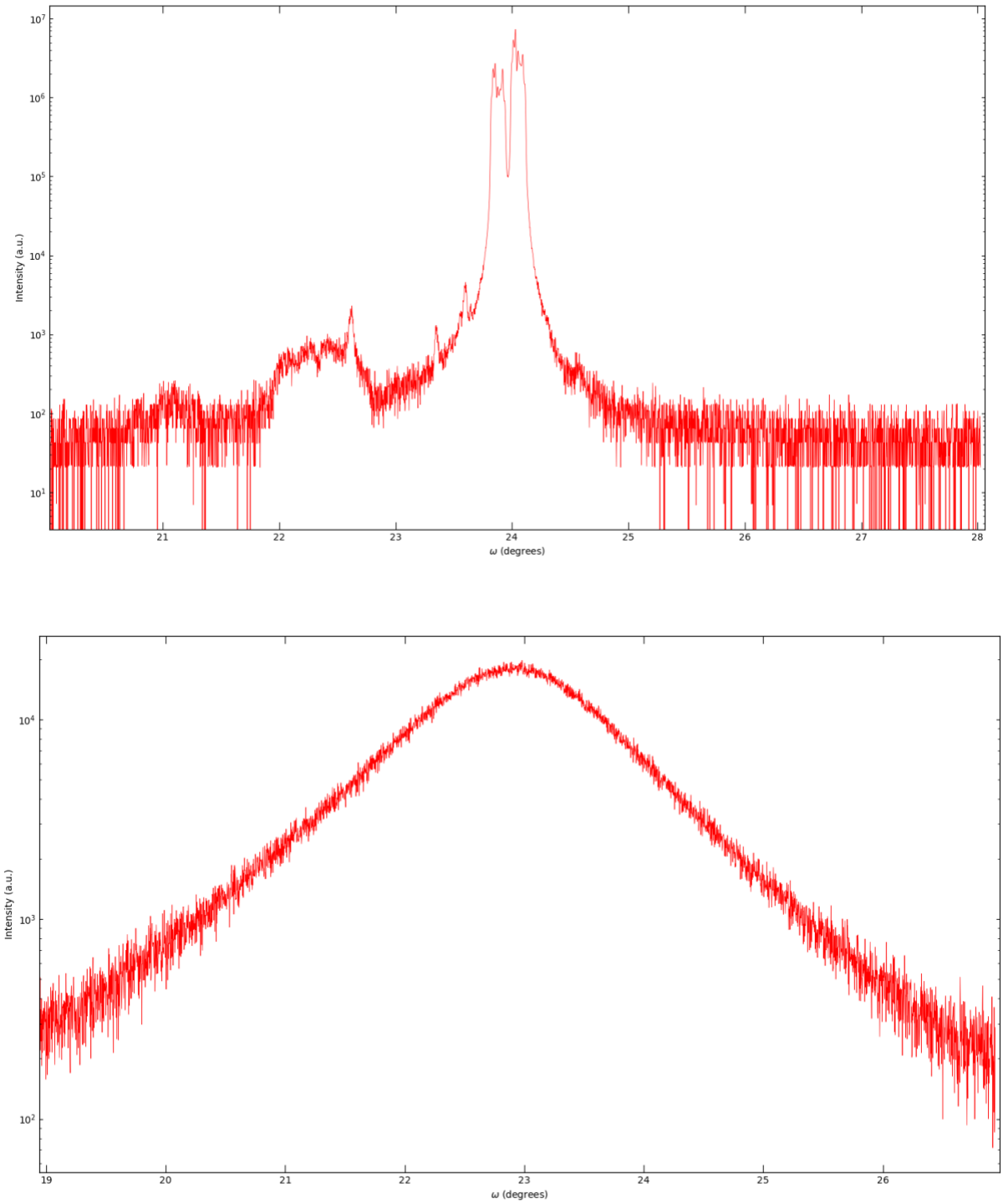

Figure A25: ω rocking curve of substrate (top) and film (bottom) of undoped CSO sample grown at 200mTorr and 750°C on LAO. $FWHM_{film} = 1.66°$

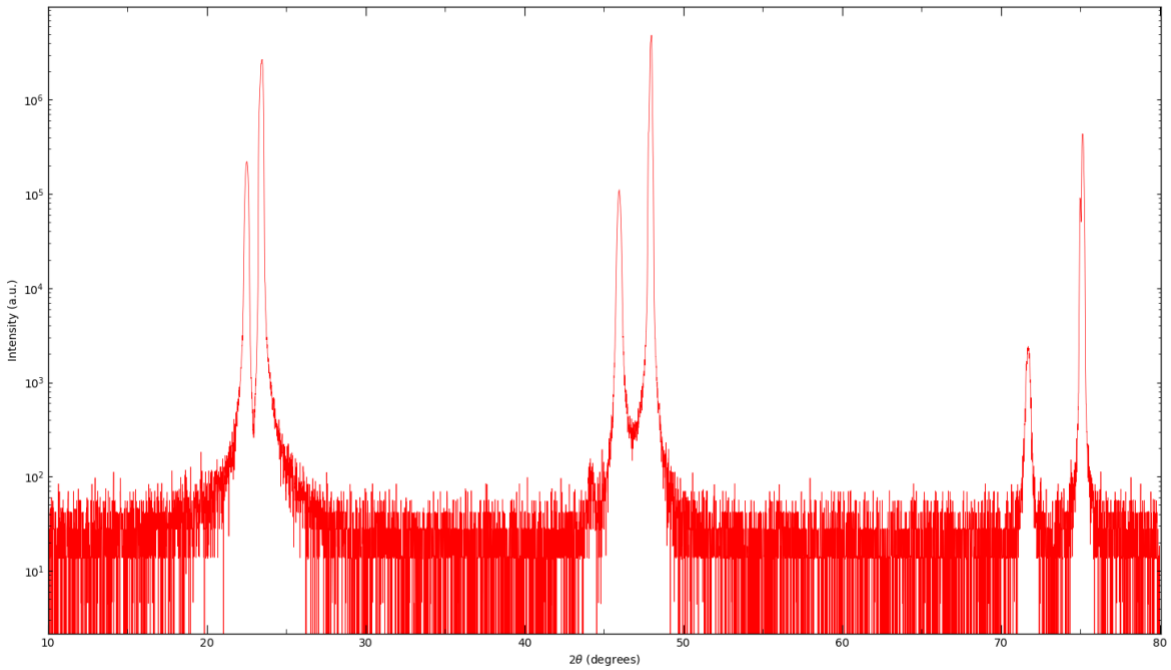

Figure A26: XRD 2θ plot of undoped CSO sample grown at 100mTorr and 850°C on LAO.

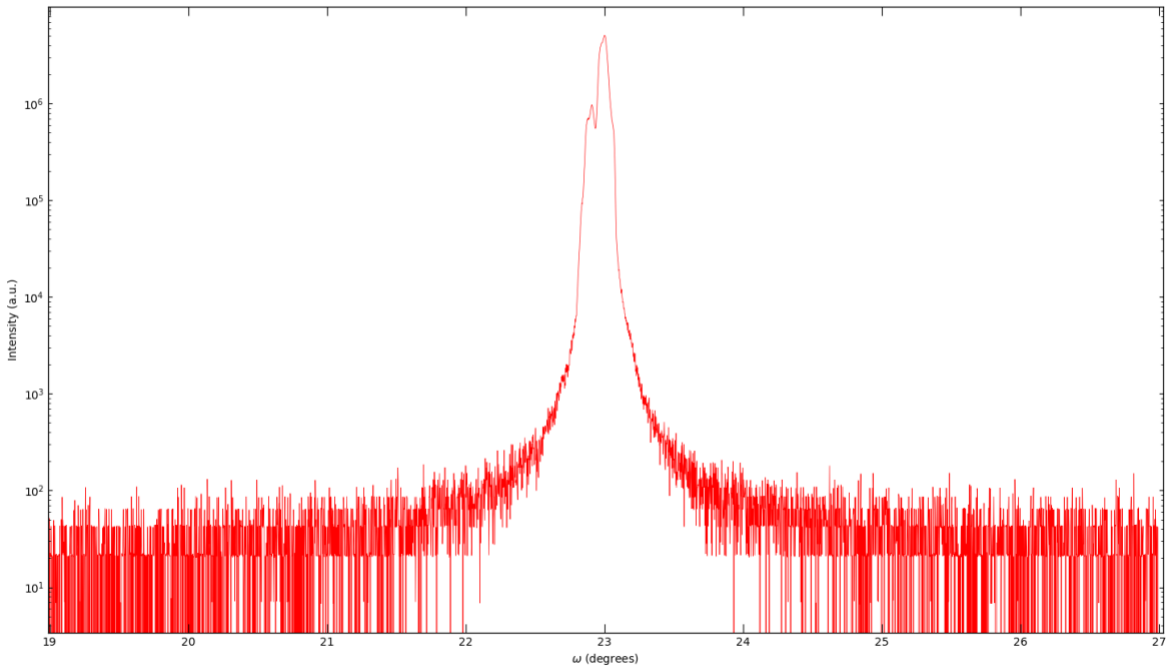

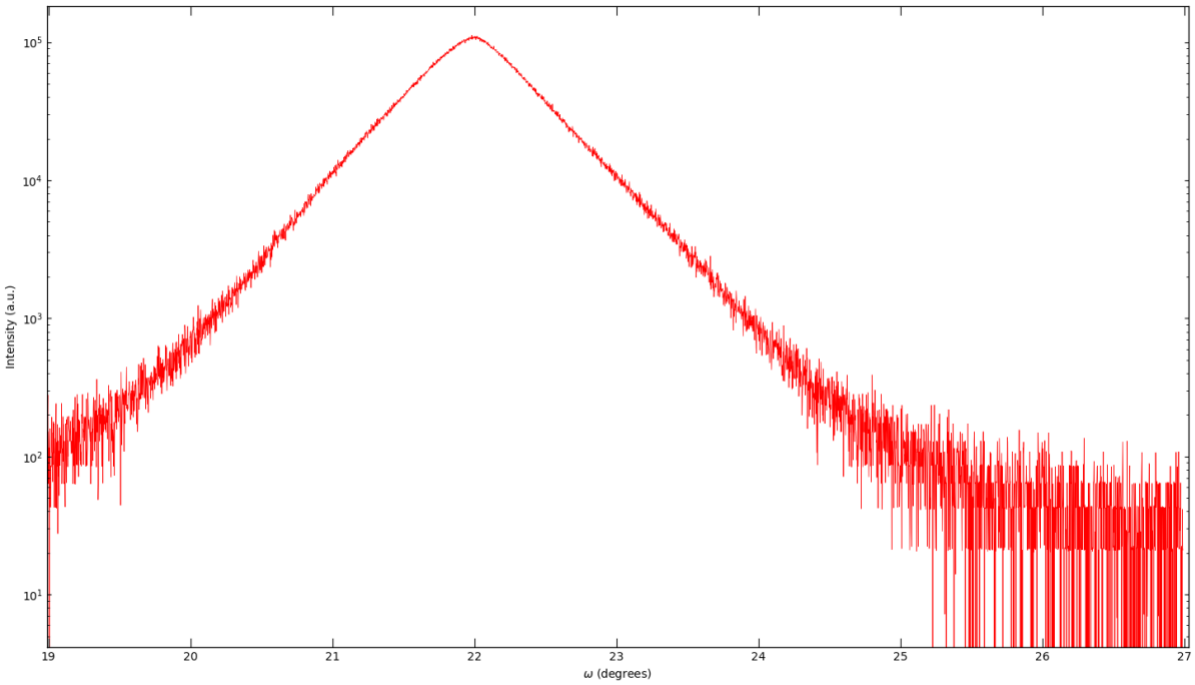

Figure A27: ω rocking curve of substrate (top) and film (bottom) of undoped CSO sample grown at 100mTorr and 850°C on LAO. $FWHM_{film} = 0.732°$

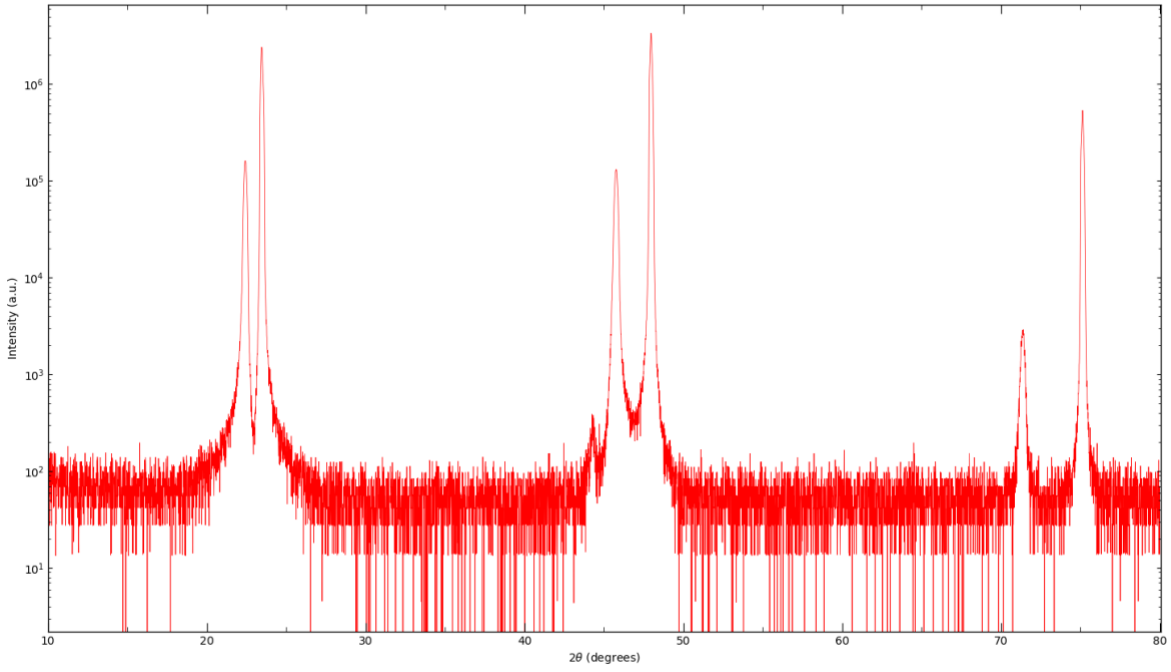

Figure A28: XRD 2θ plot of undoped CSO sample grown at 150mTorr and 850°C on LAO.

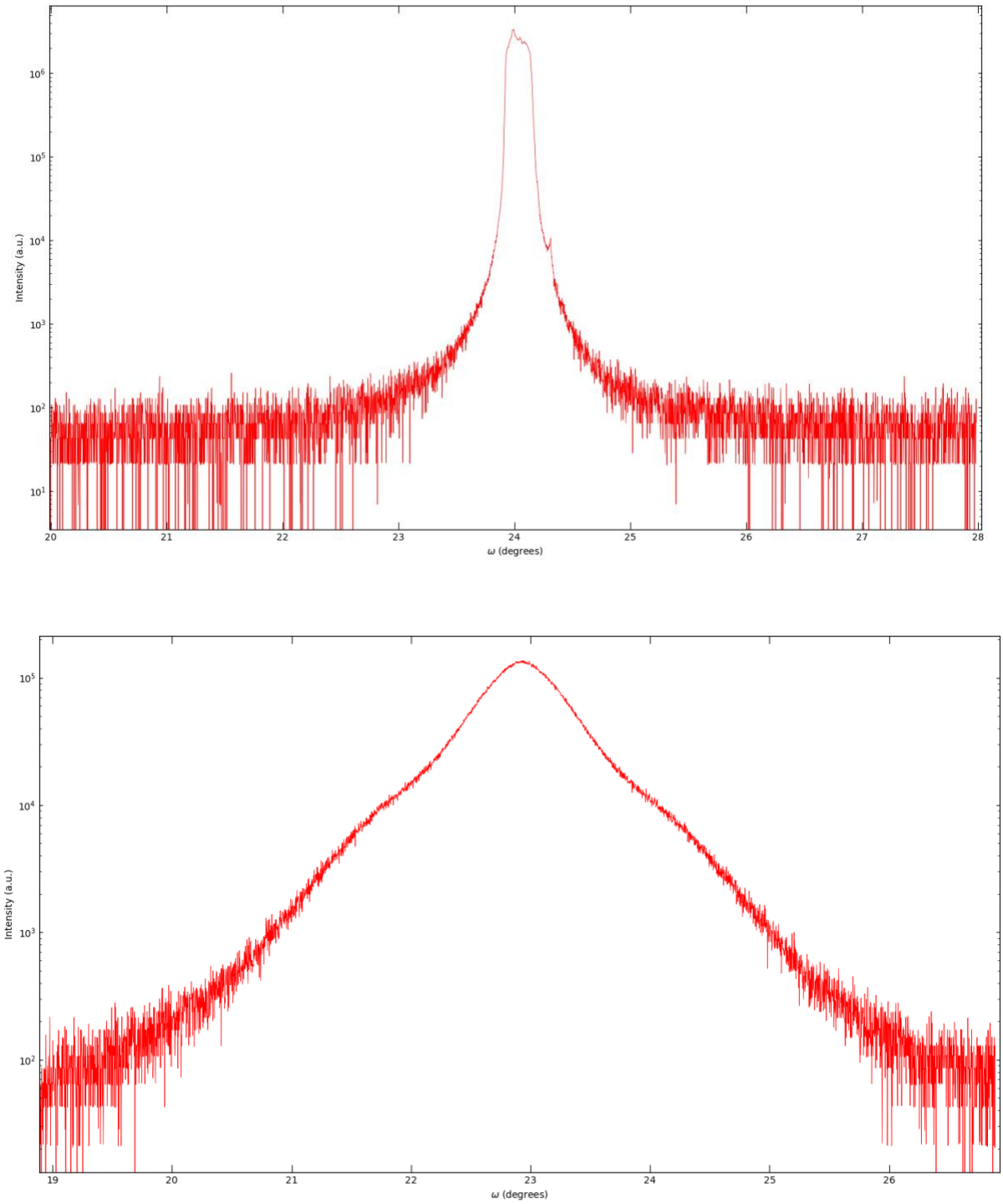

Figure A29: ω rocking curve of substrate (top) and film (bottom) of undoped CSO sample grown at 150mTorr and 850°C on LAO. $FWHM_{film} = 0.719°$

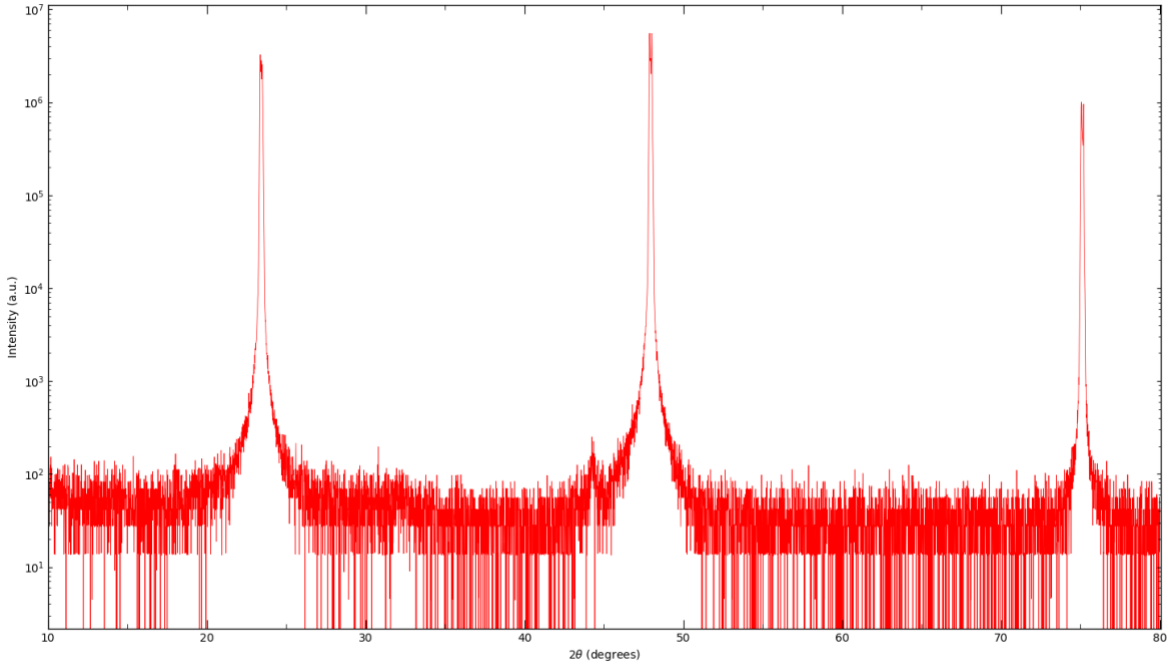

Figure A30: XRD 2θ plot of undoped CSO sample grown at 200mTorr and 850°C on LAO.

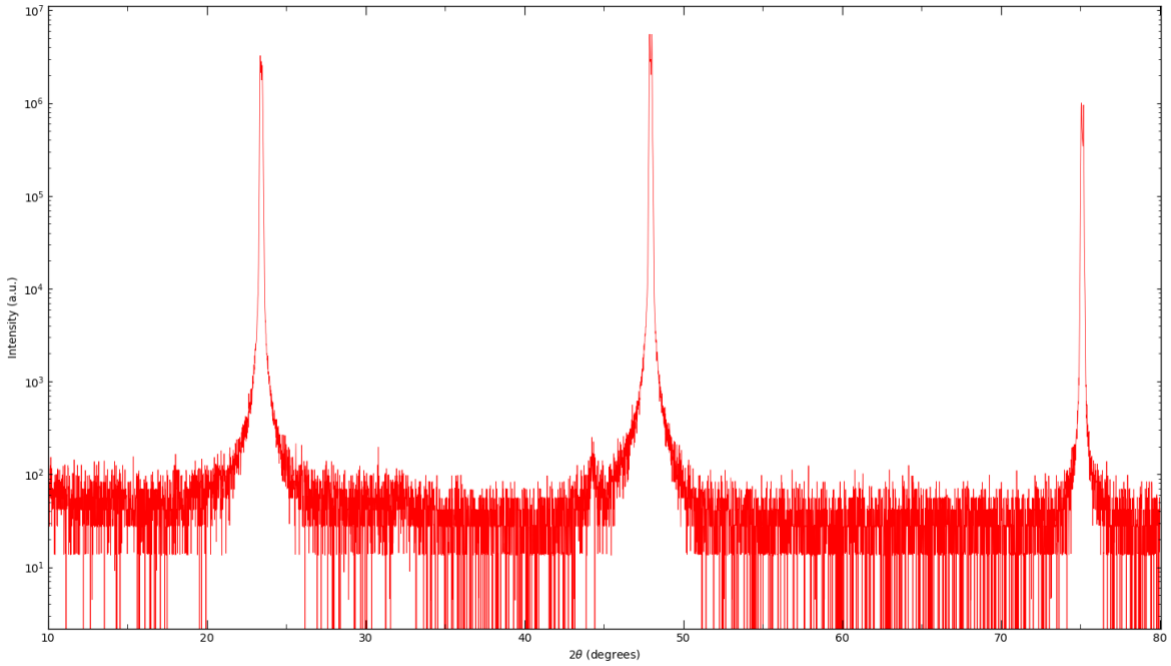

Figure A31: XRD 2θ plot of undoped CSO sample grown at 200mTorr and 850°C on LAO.

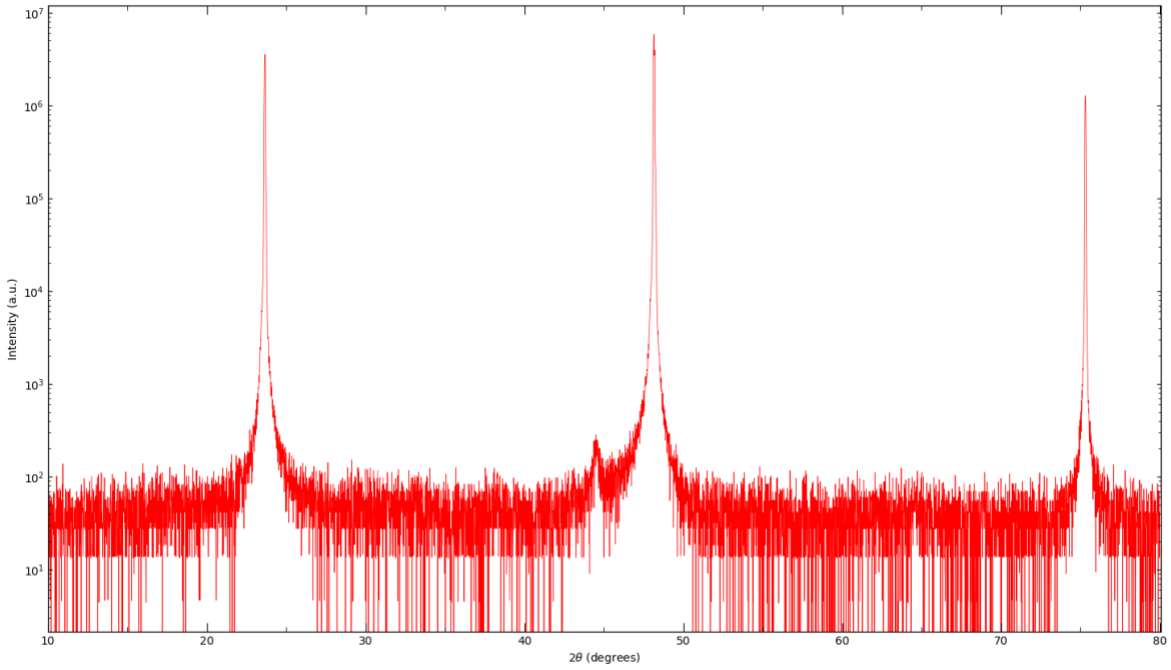

Figure A32: XRD 2θ plot of doped CSO sample grown at 100mTorr and 650°C on LAO.

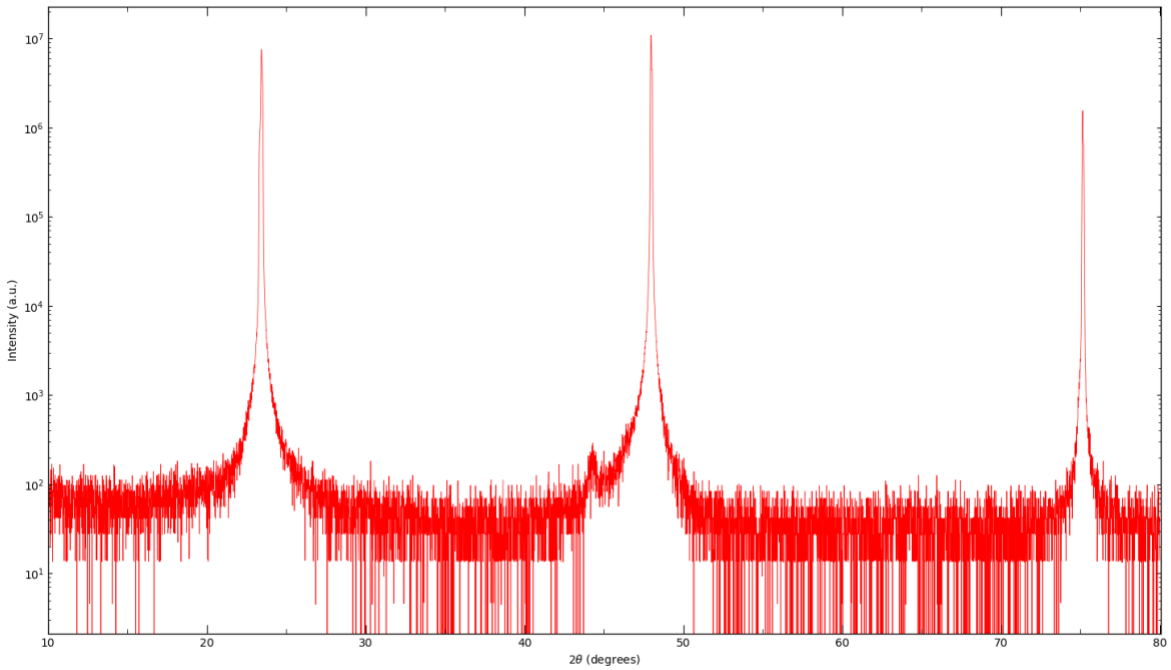

Figure A33: XRD 2θ plot of doped CSO sample grown at 150mTorr and 650°C on LAO.

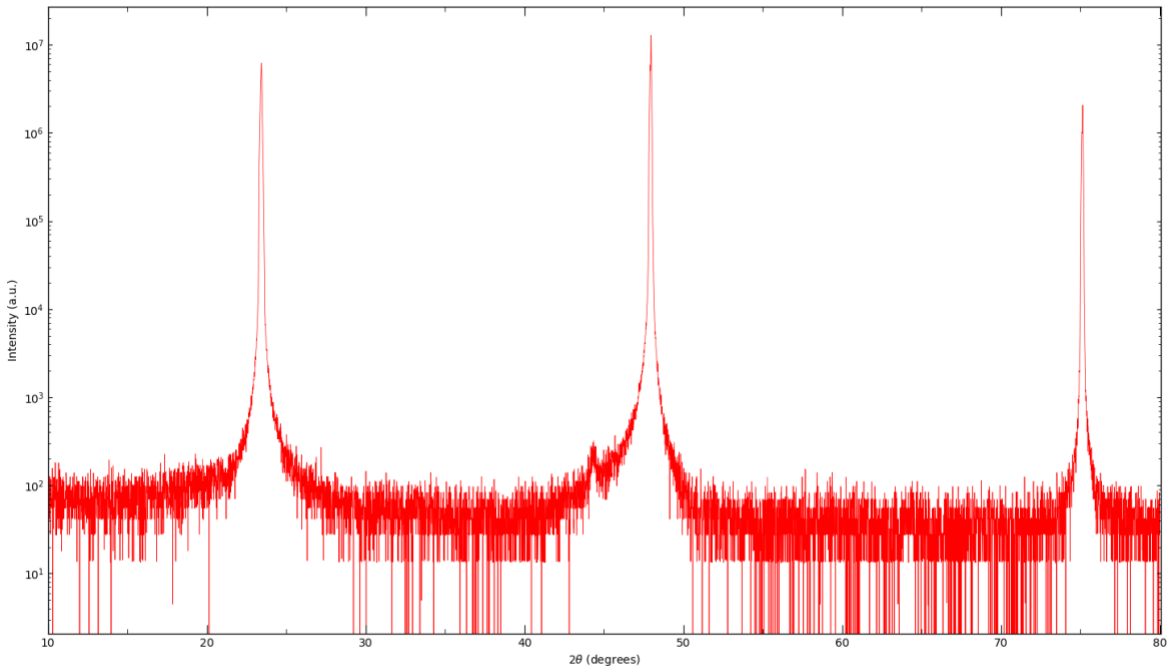

Figure A34: XRD 2θ plot of doped CSO sample grown at 200mTorr and 650°C on LAO.

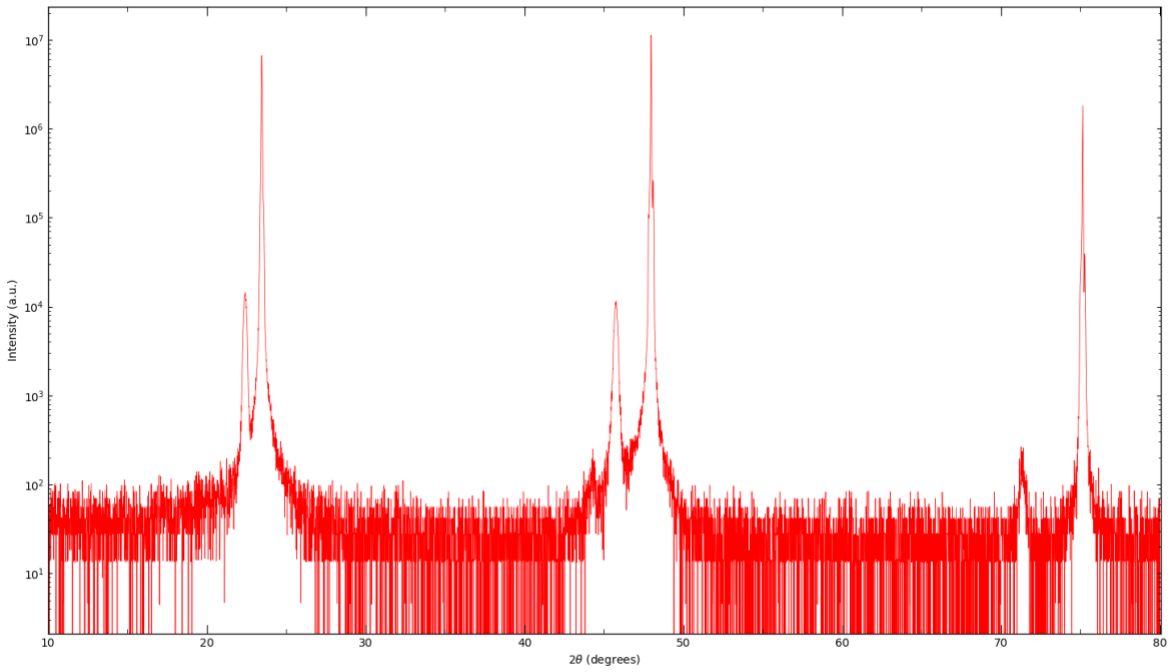

Figure A35: XRD 2θ plot of doped CSO sample grown at 100mTorr and 750°C on LAO.

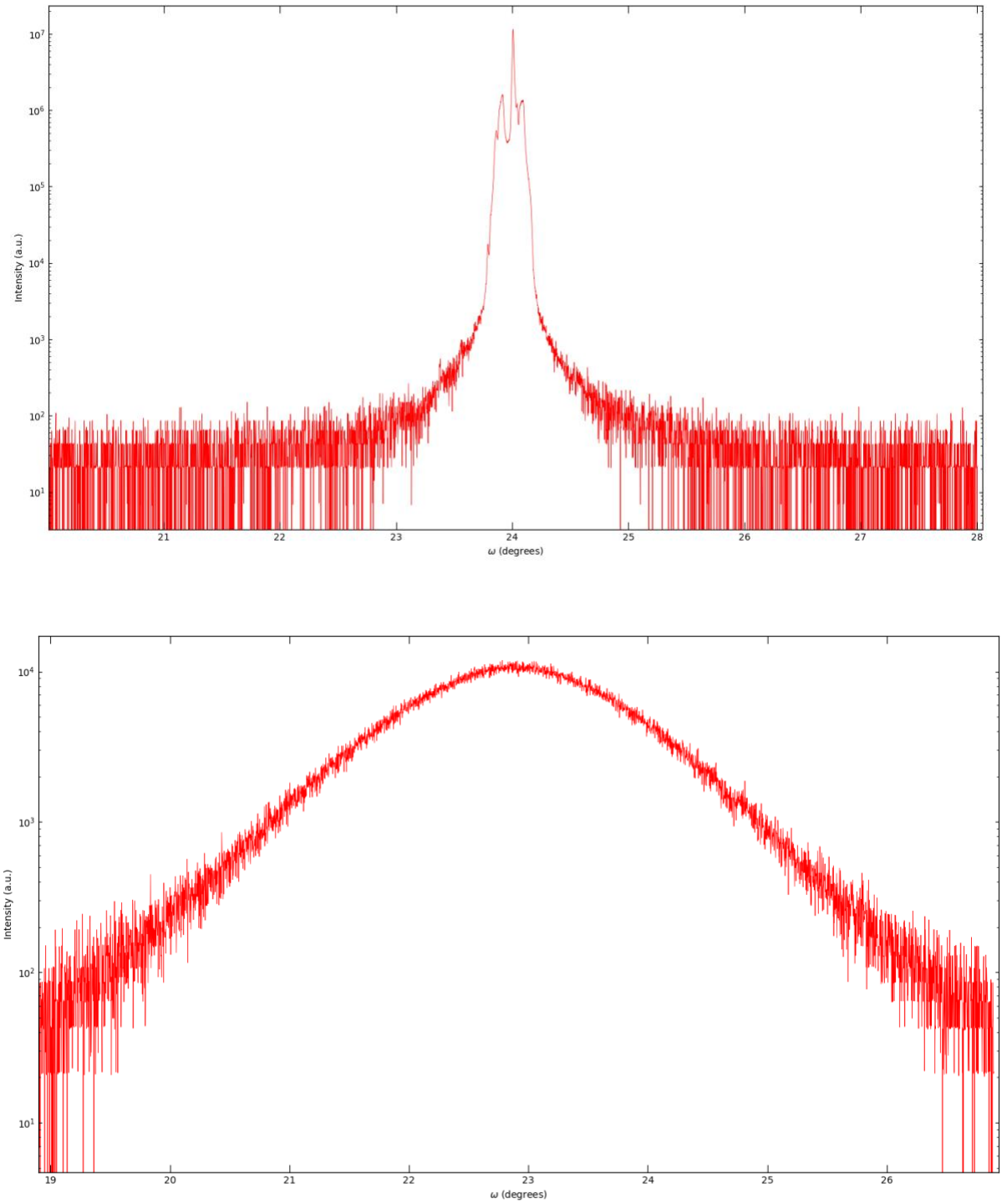

Figure A36: ω rocking curve of substrate (top) and film (bottom) of doped CSO sample grown at 100mTorr and 750°C on LAO. $FWHM_{film} = 1.904°$

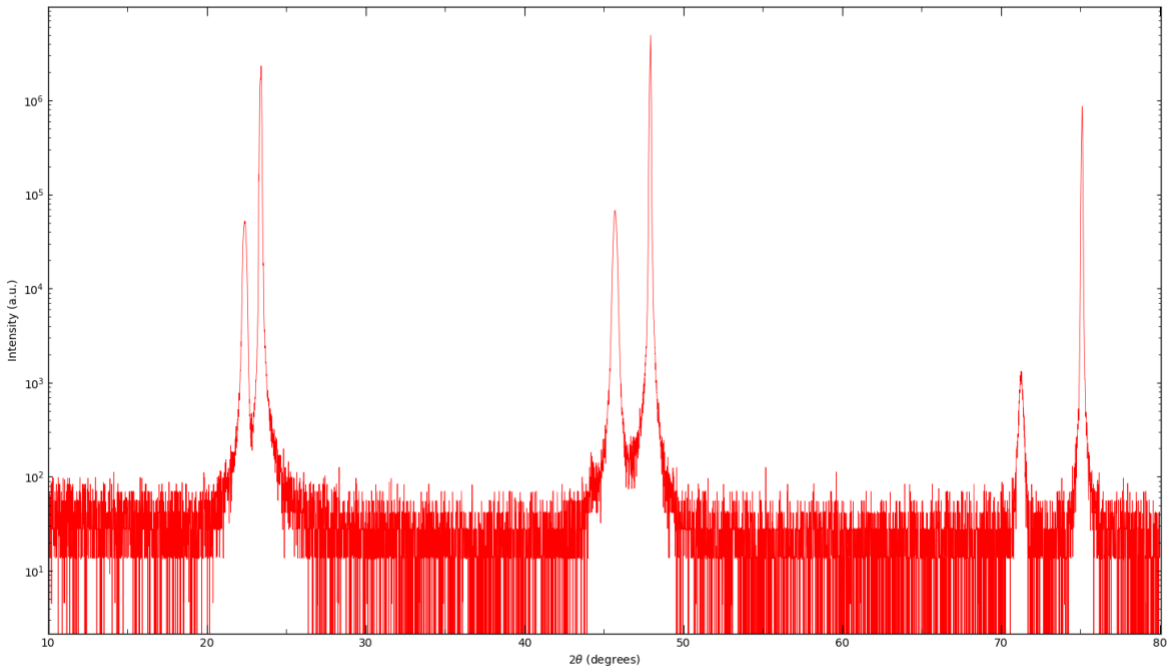

Figure A37: XRD 2θ plot of doped CSO sample grown at 150mTorr and 750°C on LAO.

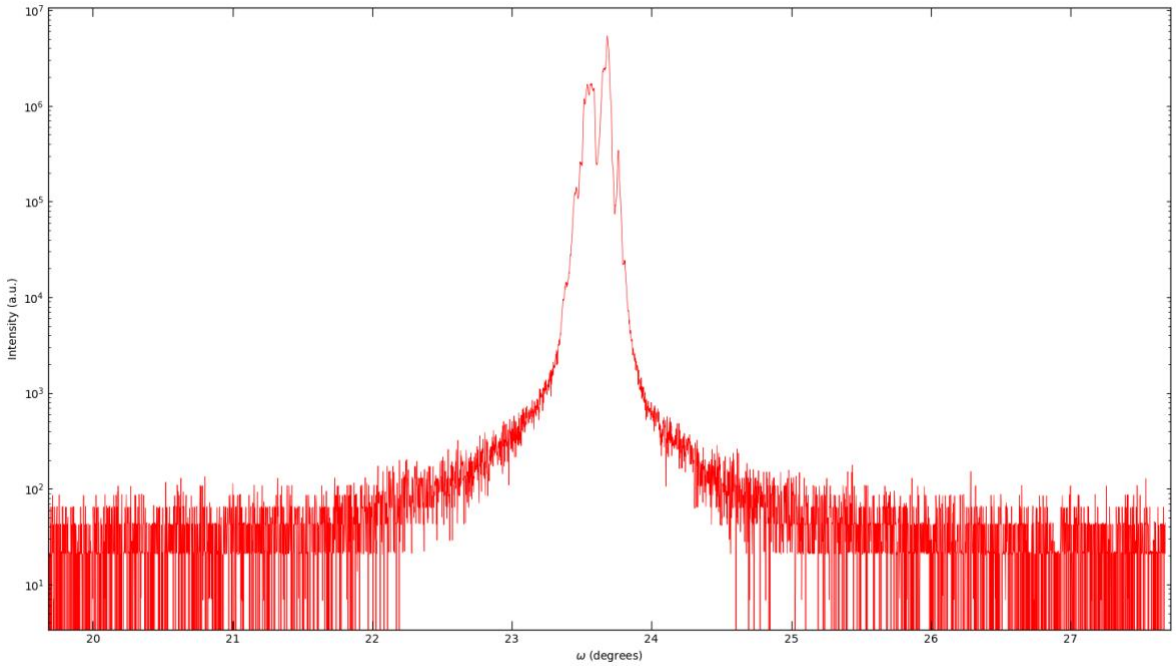

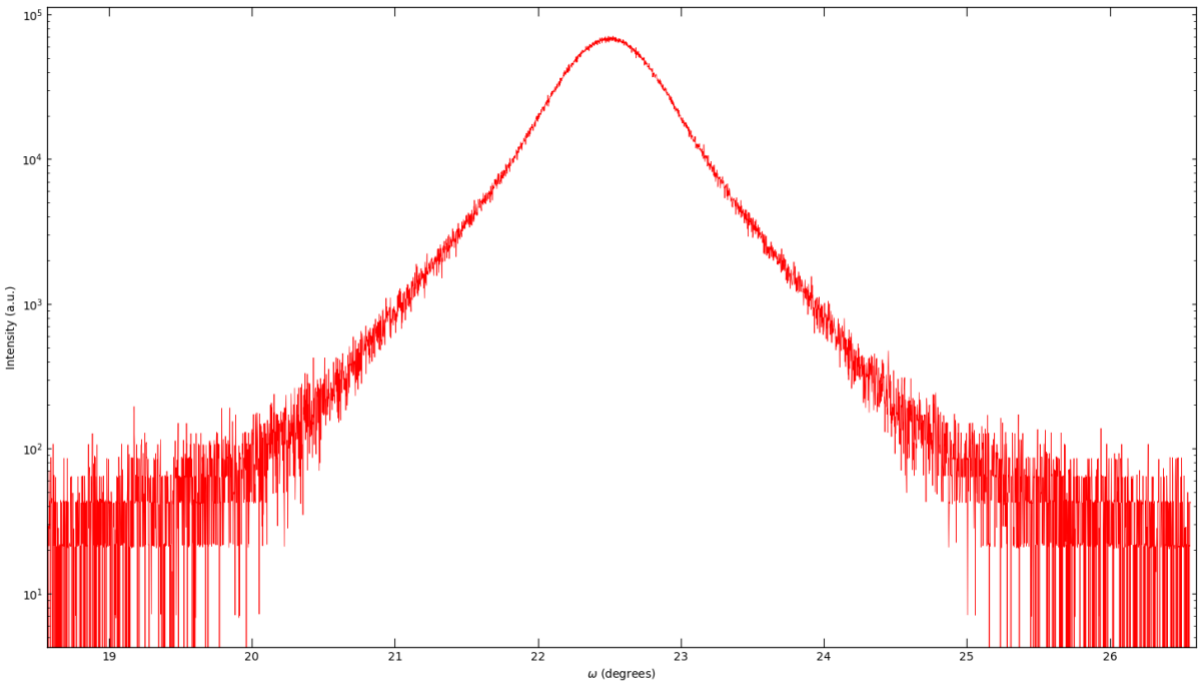

Figure A38: ω rocking curve of substrate (top) and film (bottom) of doped CSO sample grown at 150mTorr and 750°C on LAO. $FWHM_{film} = 0.698°$

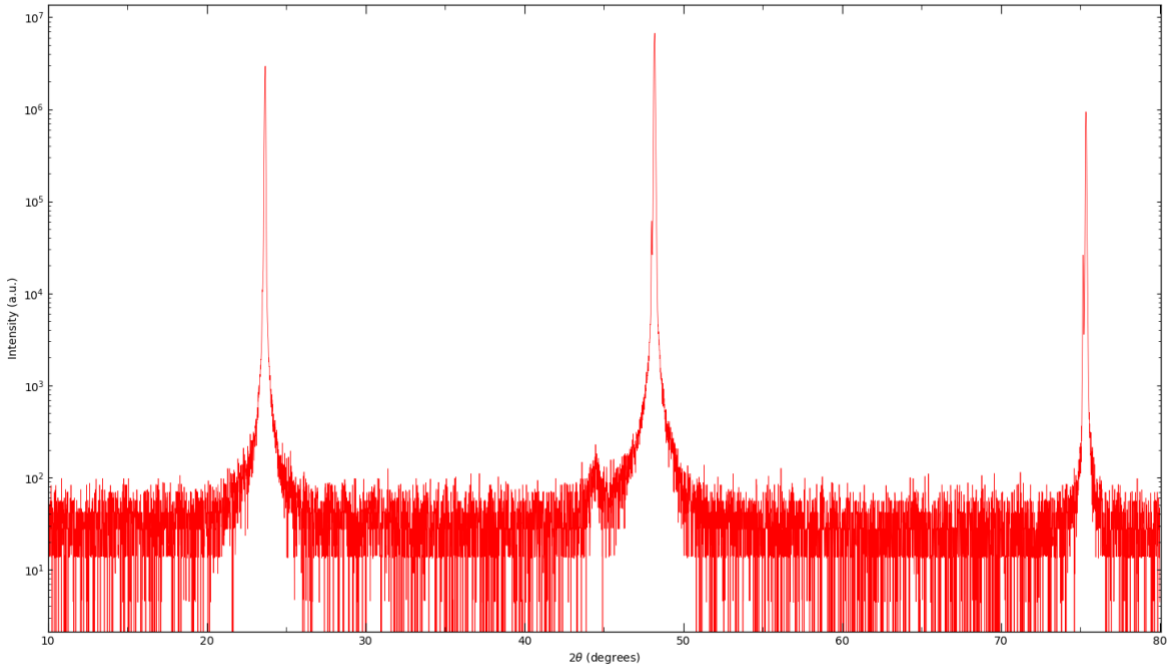

Figure A39: XRD 2θ plot of doped CSO sample grown at 200mTorr and 750°C on LAO.

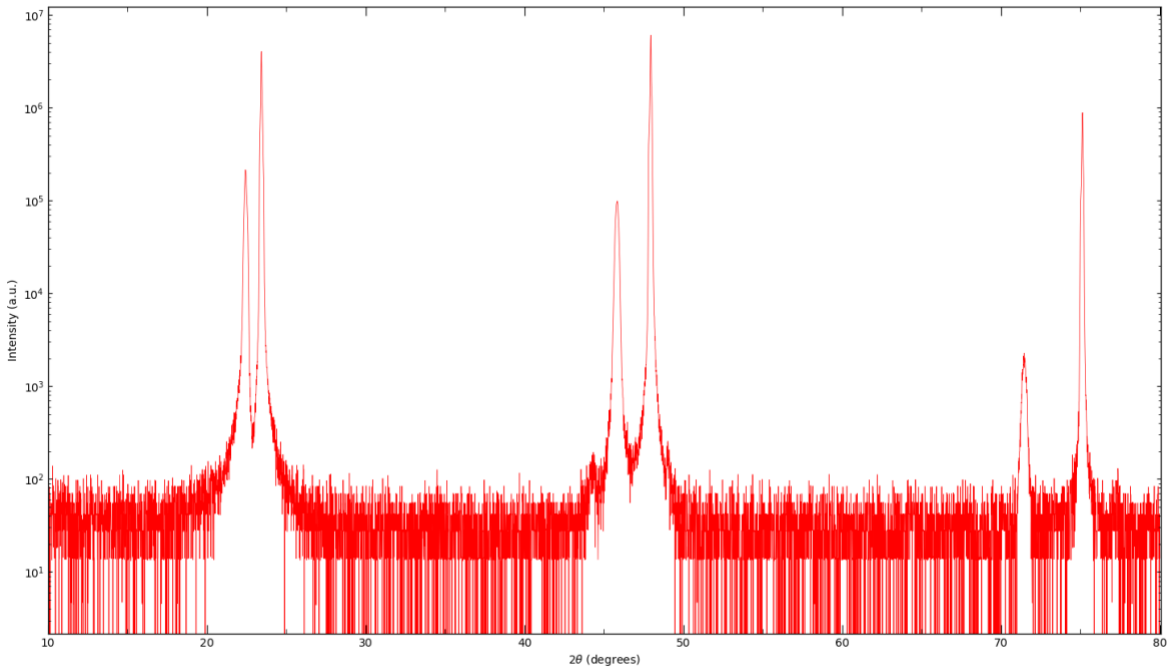

Figure 40: XRD 2θ plot of doped CSO sample grown at 100mTorr and 850°C on LAO.

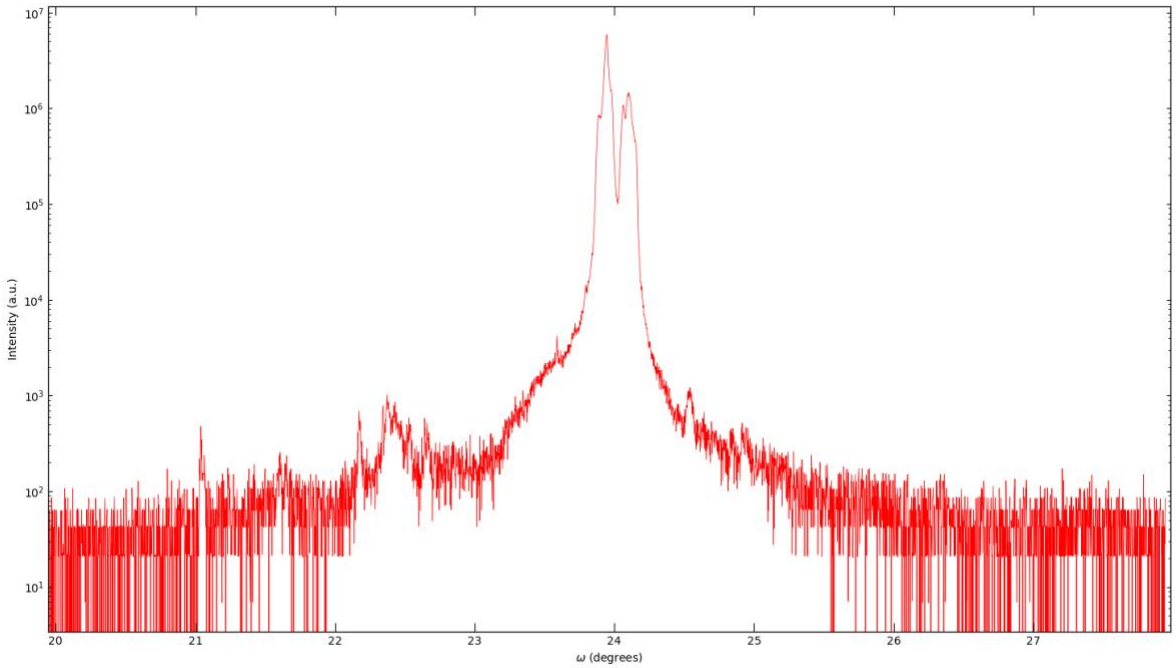

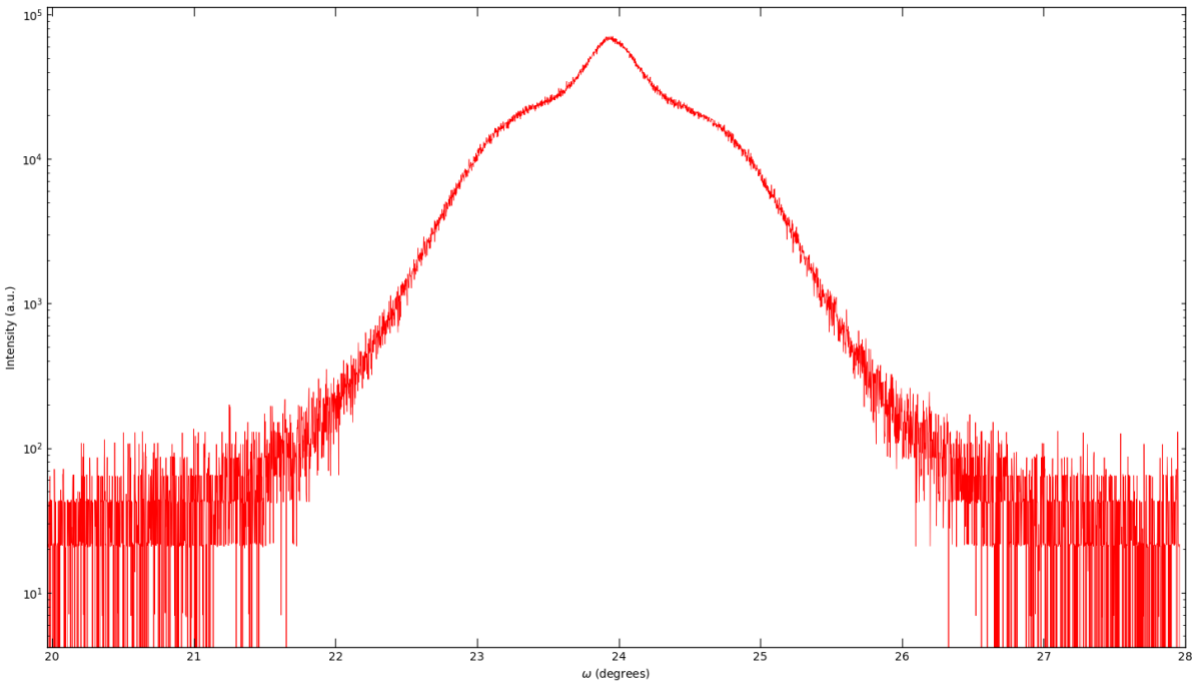

Figure A41: ω rocking curve of substrate (top) and film (bottom) of doped CSO sample grown at 100mTorr and 850°C on LAO. $FWHM_{film} = 0.538°$

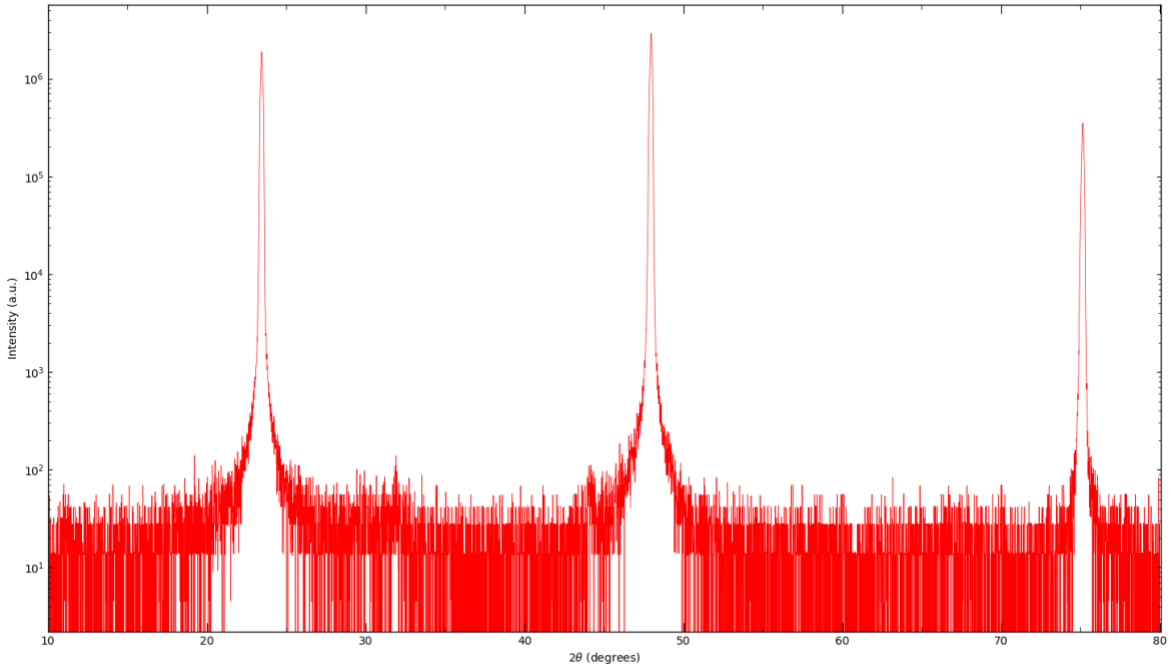

Figure A42: XRD 2θ plot of doped CSO sample grown at 150mTorr and 850°C on LAO.

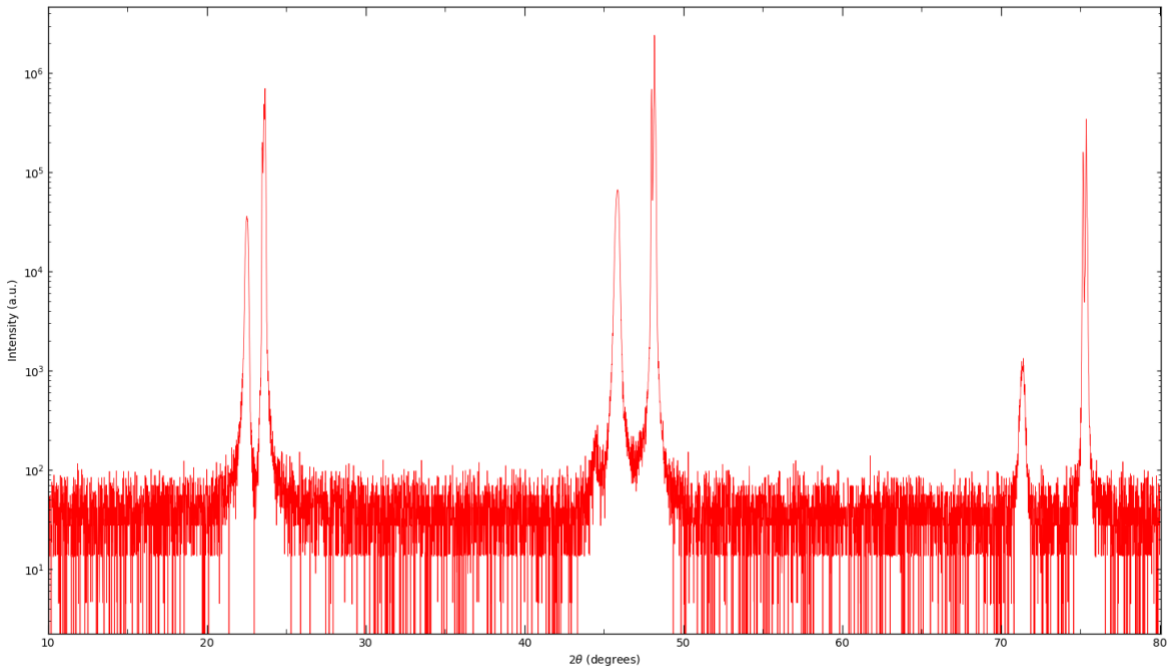

Figure A43: XRD 2θ plot of doped CSO sample grown at 200mTorr and 850°C on LAO.

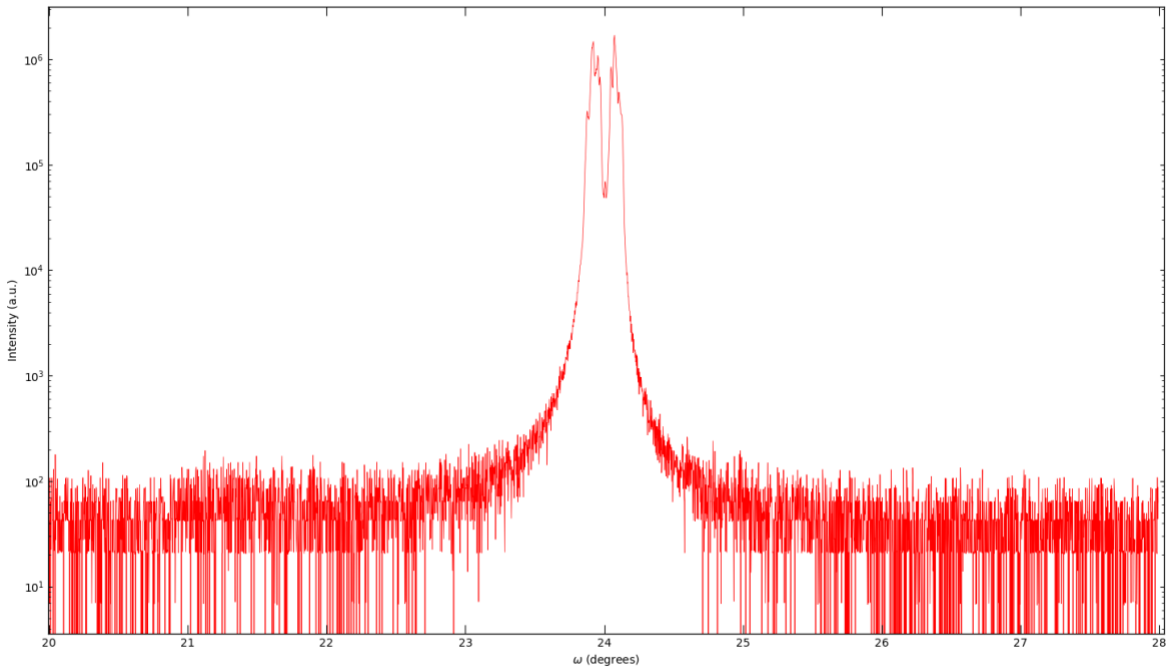

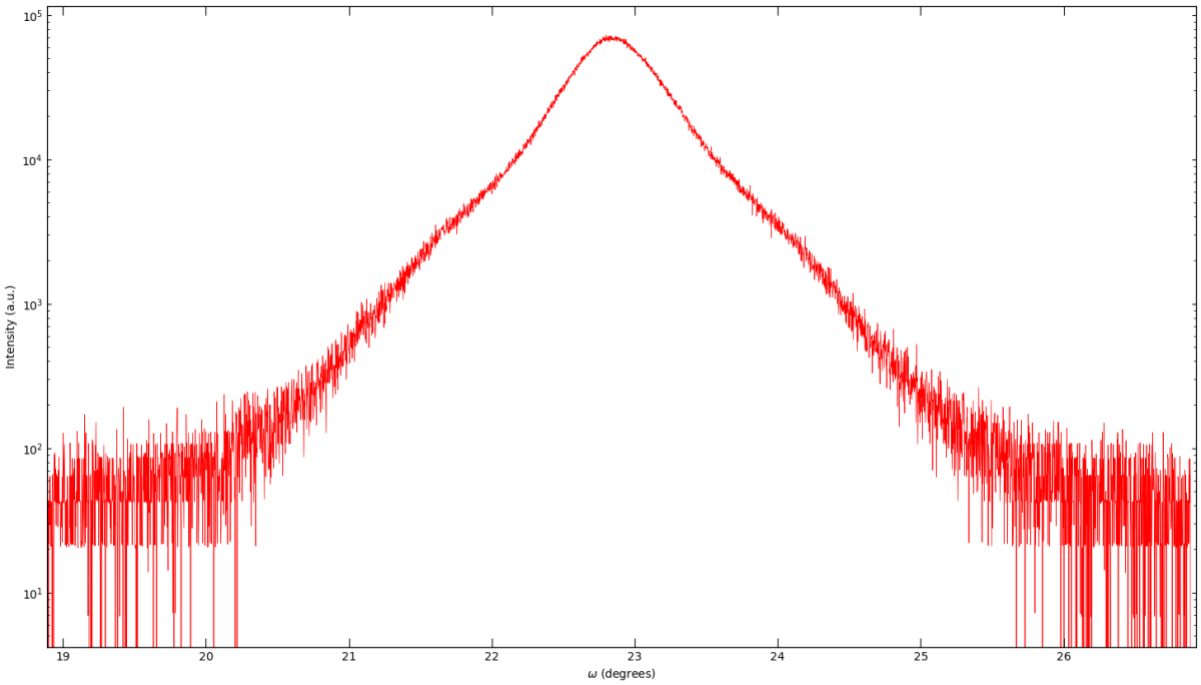

Figure A44: ω rocking curve of substrate (top) and film (bottom) of doped CSO sample grown at 200mTorr and 850°C on LAO. $FWHM_{film} = 0.650°$

The following 8 figures showcase the attempted depositions of the films that did not indicate film growth, of which two of the three were successful.

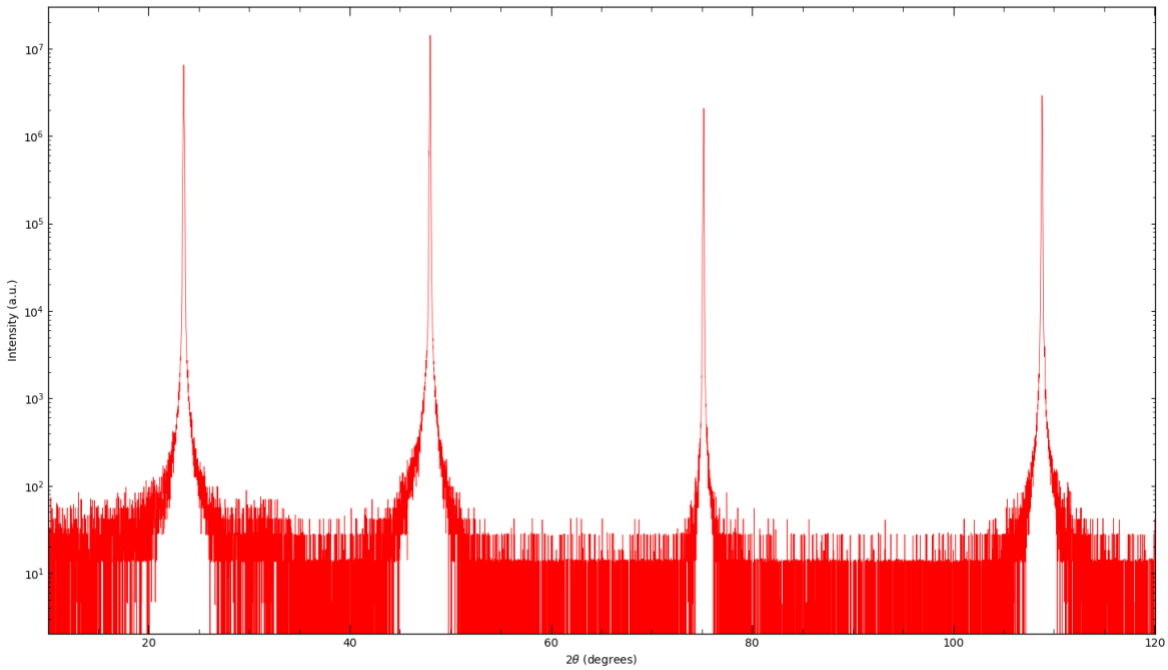

Figure A45: XRD 2θ plot of undoped CSO sample grown at 200mTorr and 850°C on LAO (unsuccessful).

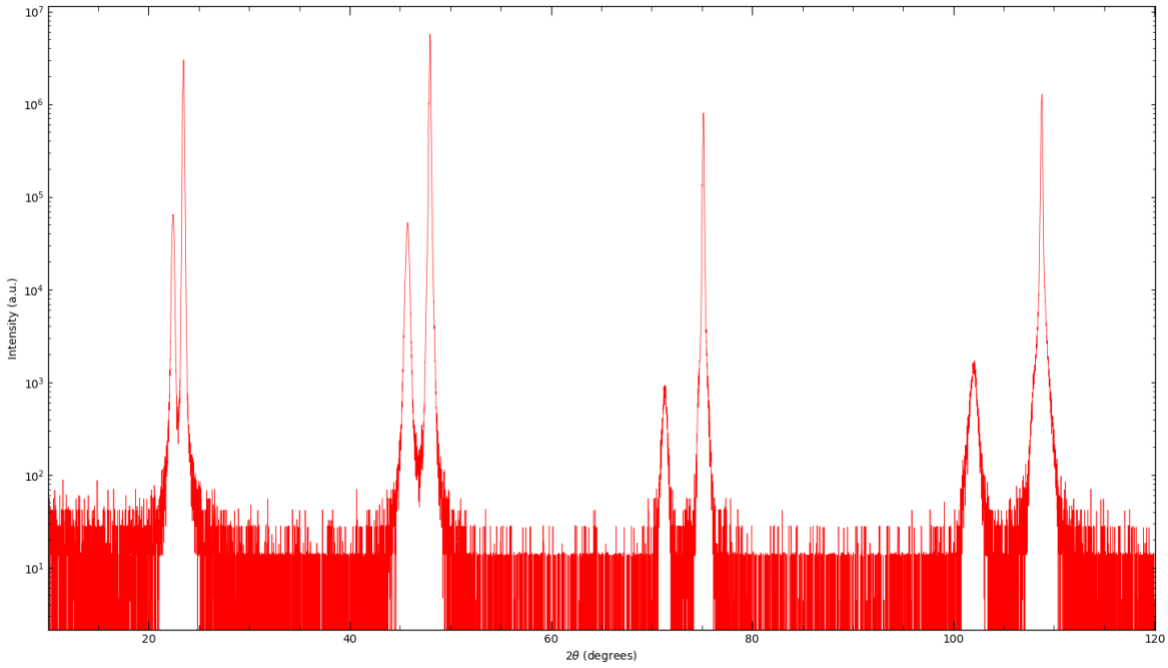

Figure A46: XRD 2θ plot of doped CSO sample grown at 150mTorr and 850°C on LAO.

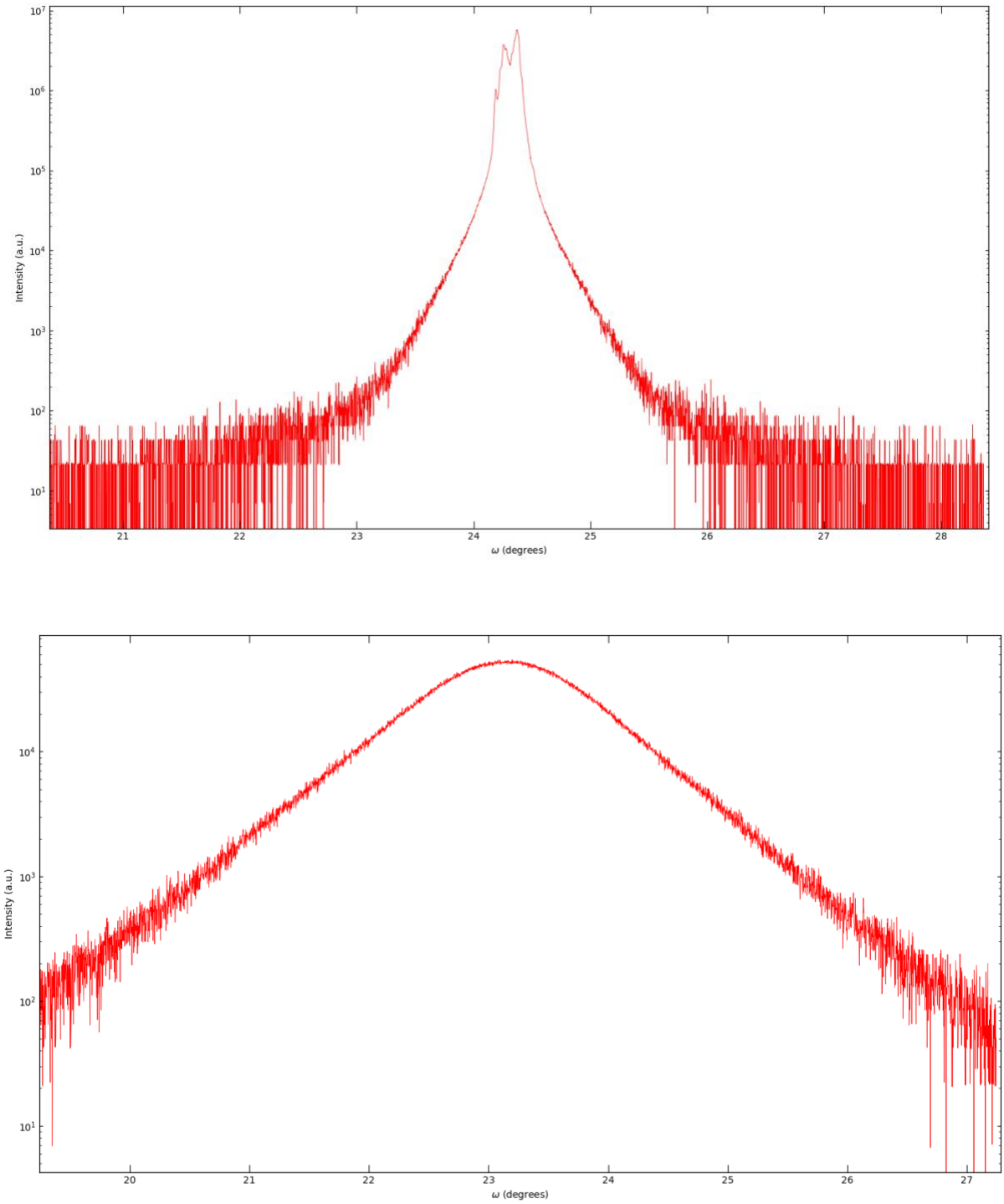

Figure A47: ω rocking curve of substrate (top) and film (bottom) of doped CSO sample grown at 150mTorr and 850°C on LAO. $FWHM_{film} = 1.432°$

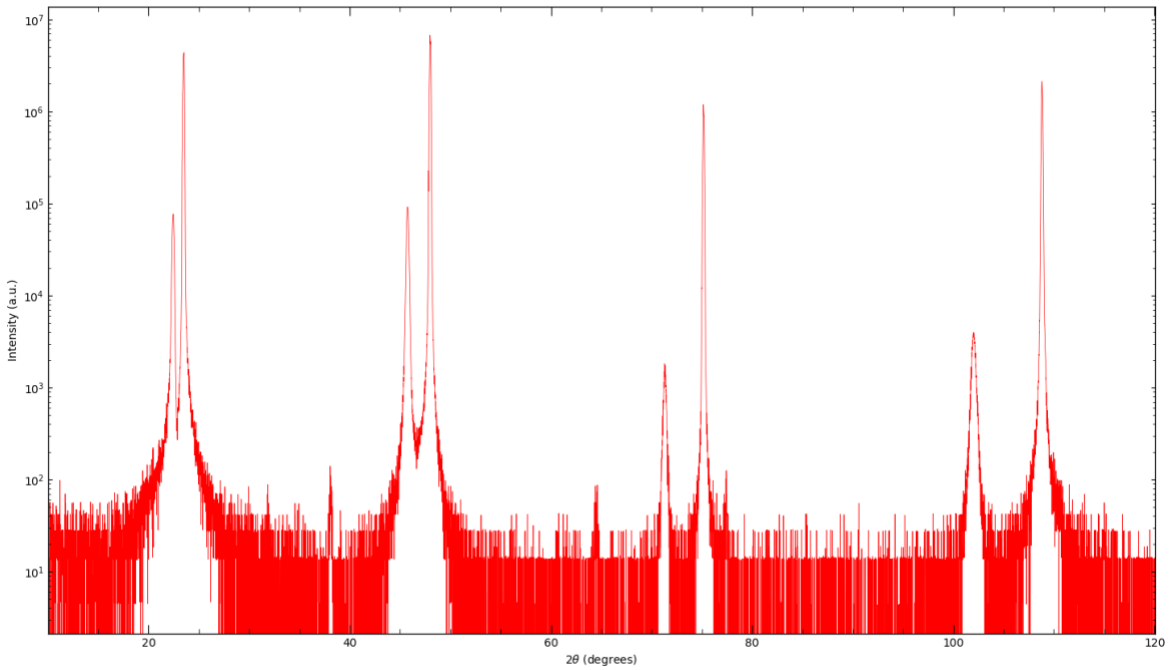

Figure A48: XRD 2θ plot of doped CSO sample grown at 200mTorr and 750°C on LAO.

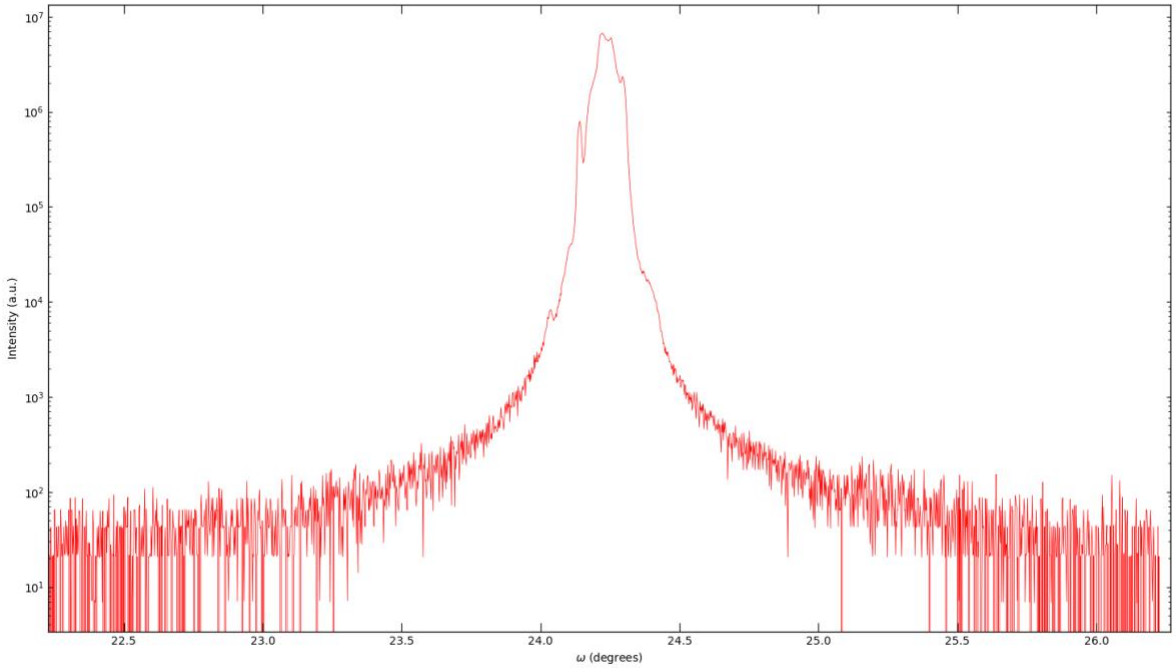

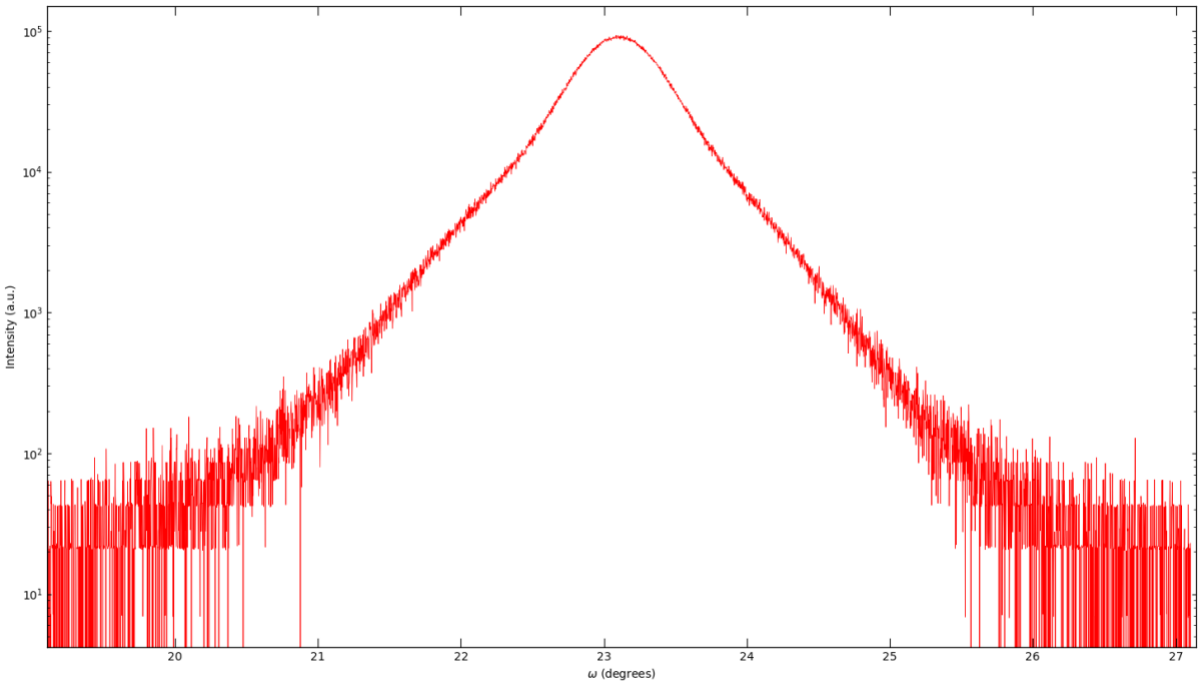

Figure A49: ω rocking curve of substrate (top) and film (bottom) of doped CSO sample grown at 200mTorr and 750°C on LAO. $FWHM_{film} = 0.670°$

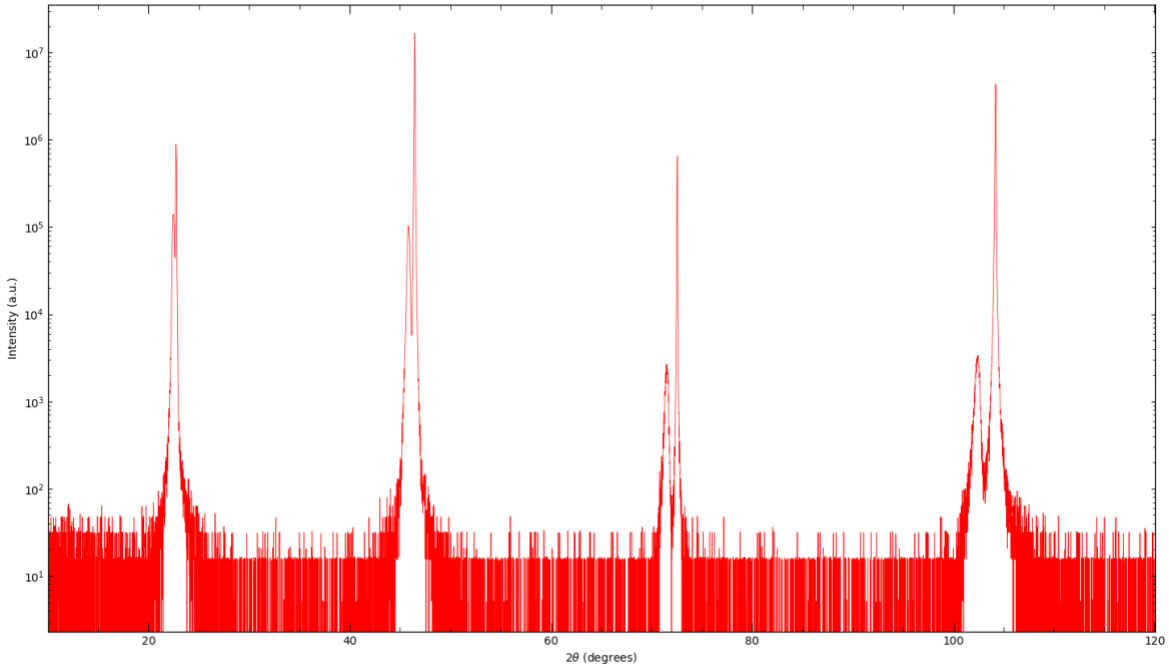

Figure A50: XRD 2θ plot of undoped CSO sample grown at 100mTorr and 850°C on STO.

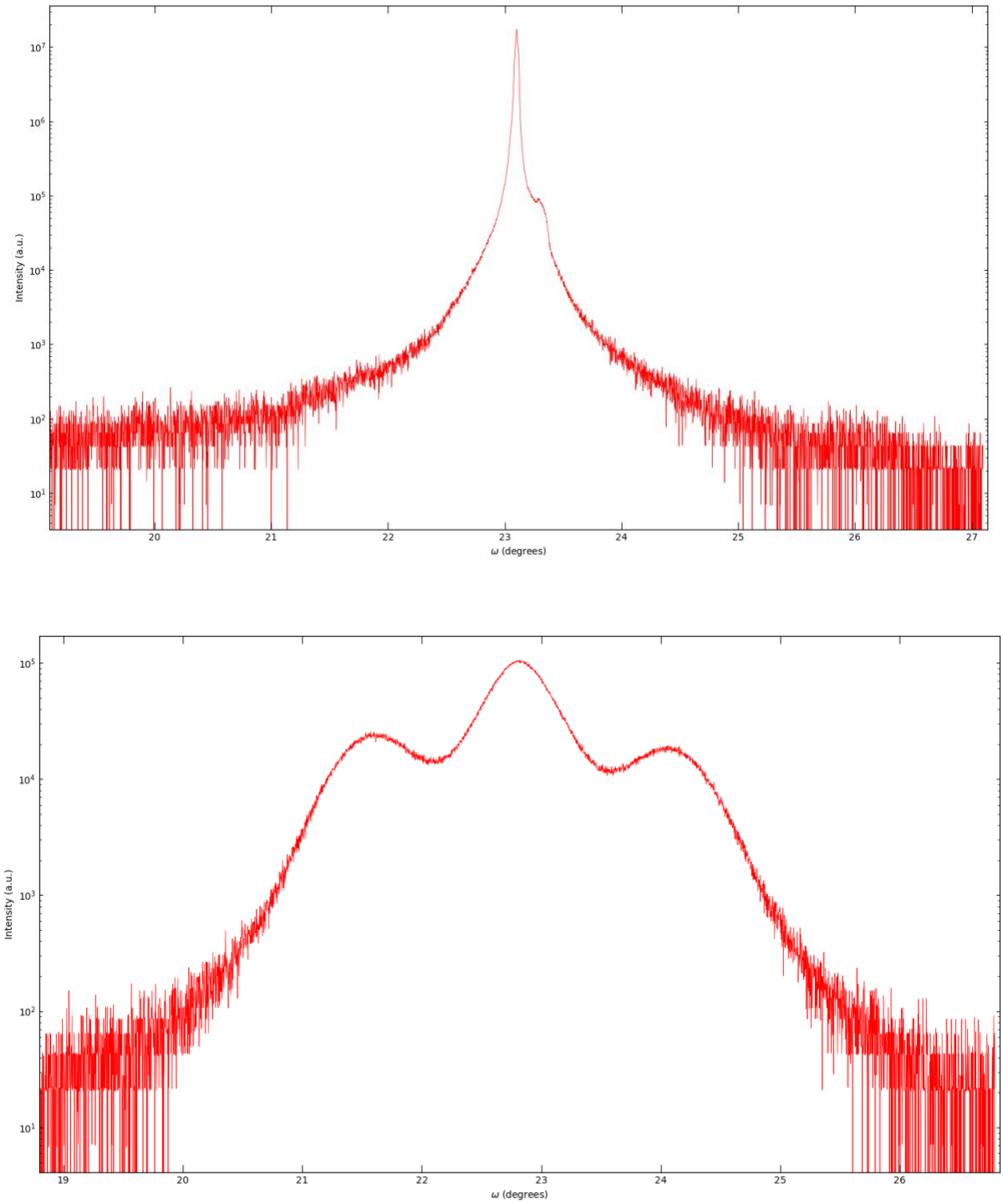

Figure A51: ω rocking curve of substrate (top) and film (bottom) of doped CSO sample grown at 100mTorr and 850°C on STO. $FWHM_{film} = 0.536°$

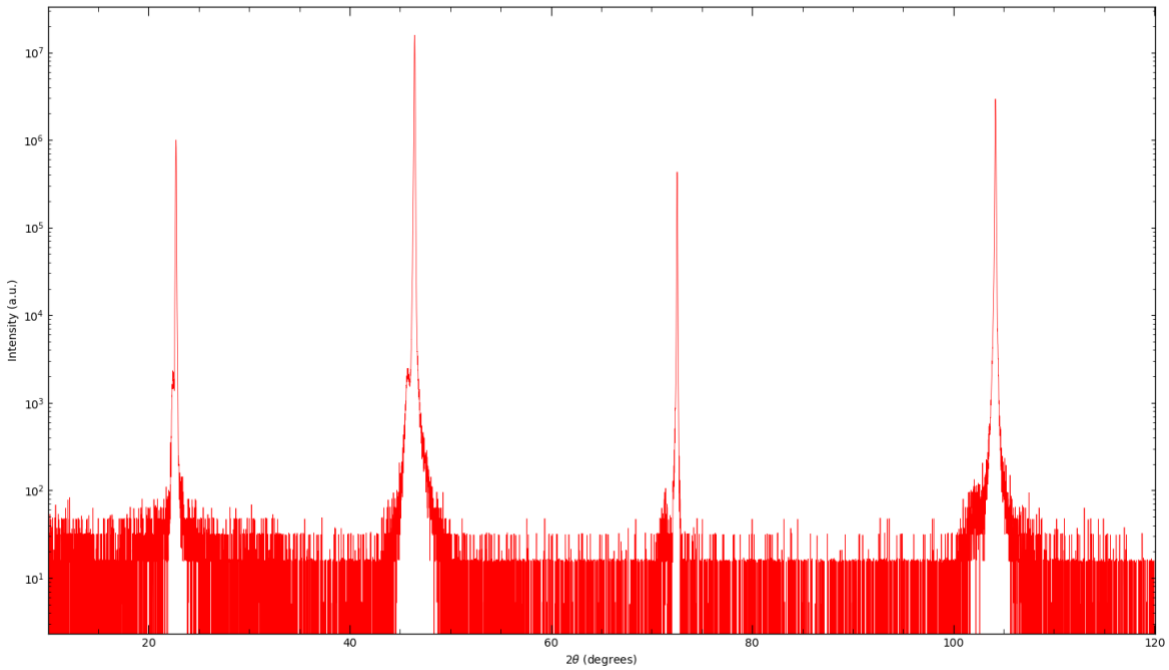

Figure A52: XRD 2θ plot of doped CSO sample grown at 100mTorr and 850°C on STO.

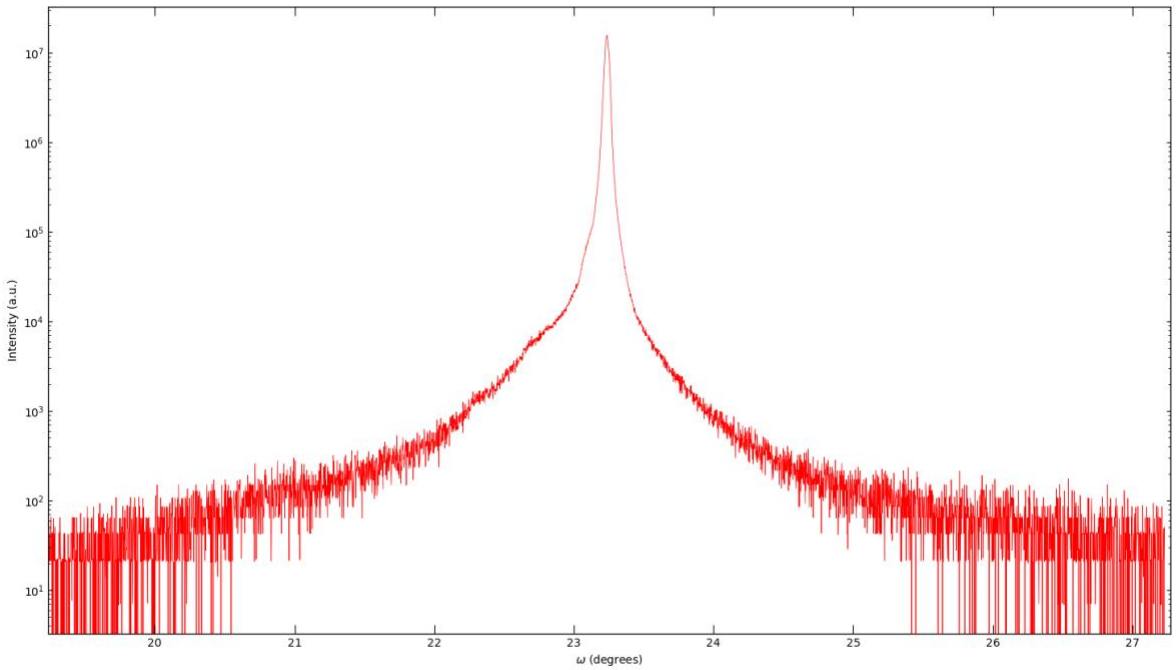

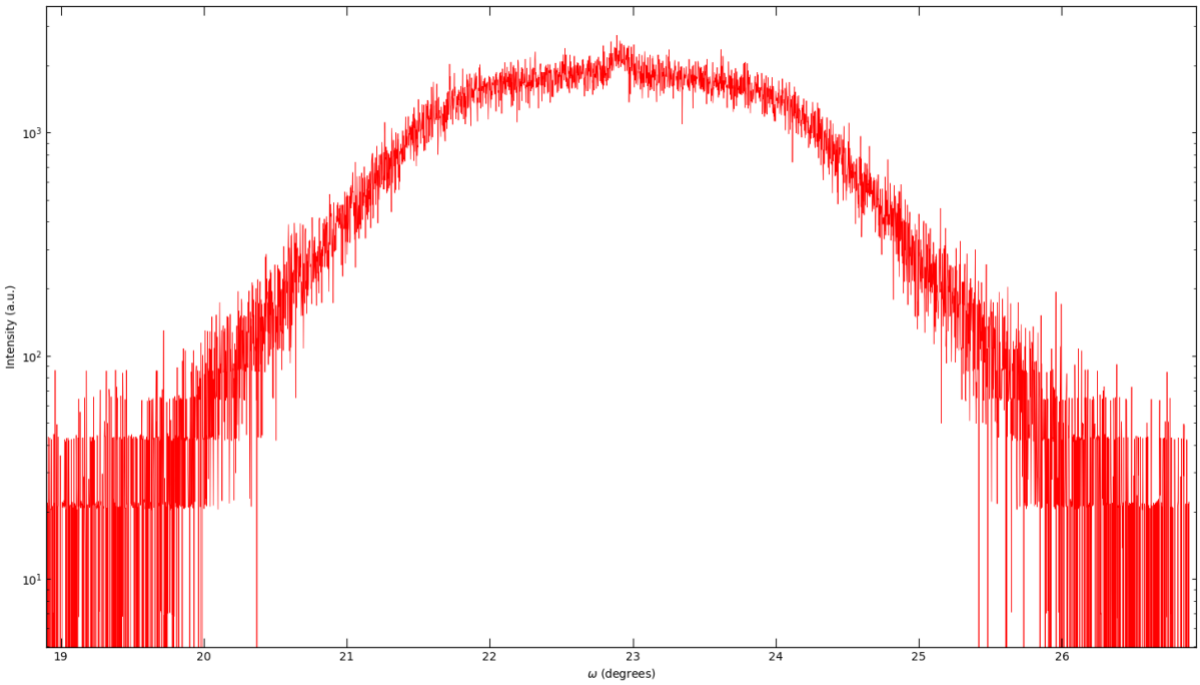

Figure A53: ω rocking curve of substrate (top) and film (bottom) of doped CSO sample grown at 100mTorr and 850°C on STO. $FWHM_{film} = 2.628°$

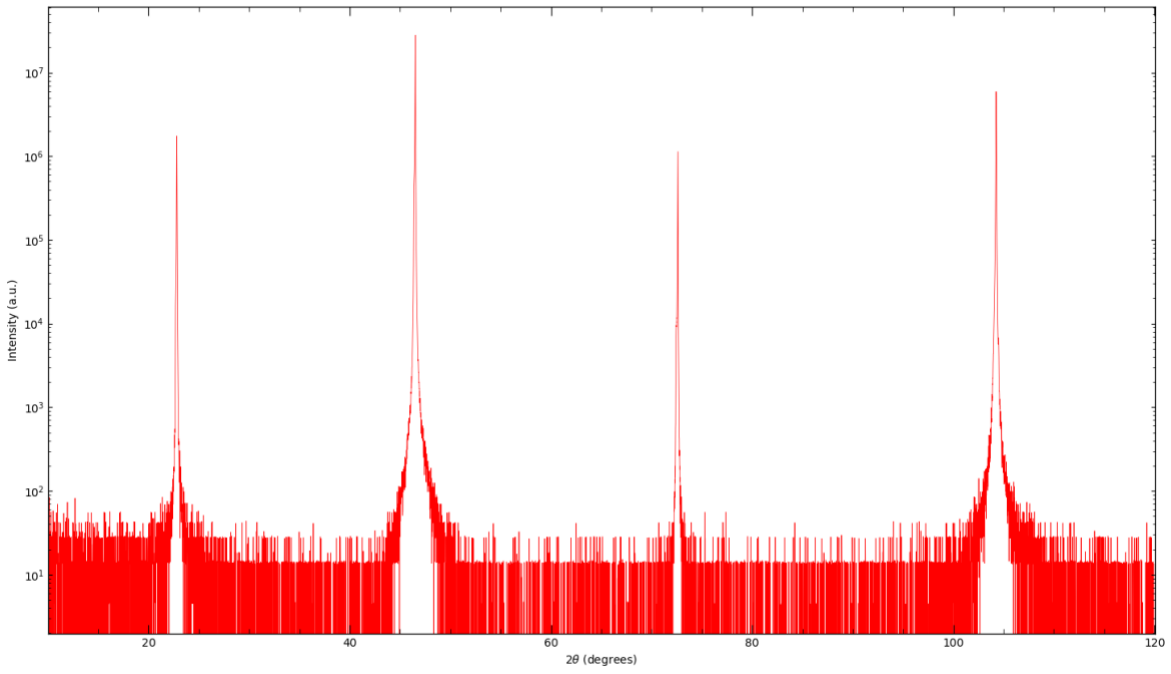

Figure A54: XRD 2θ plot of thin doped CSO sample grown at 100mTorr and 850°C on STO.

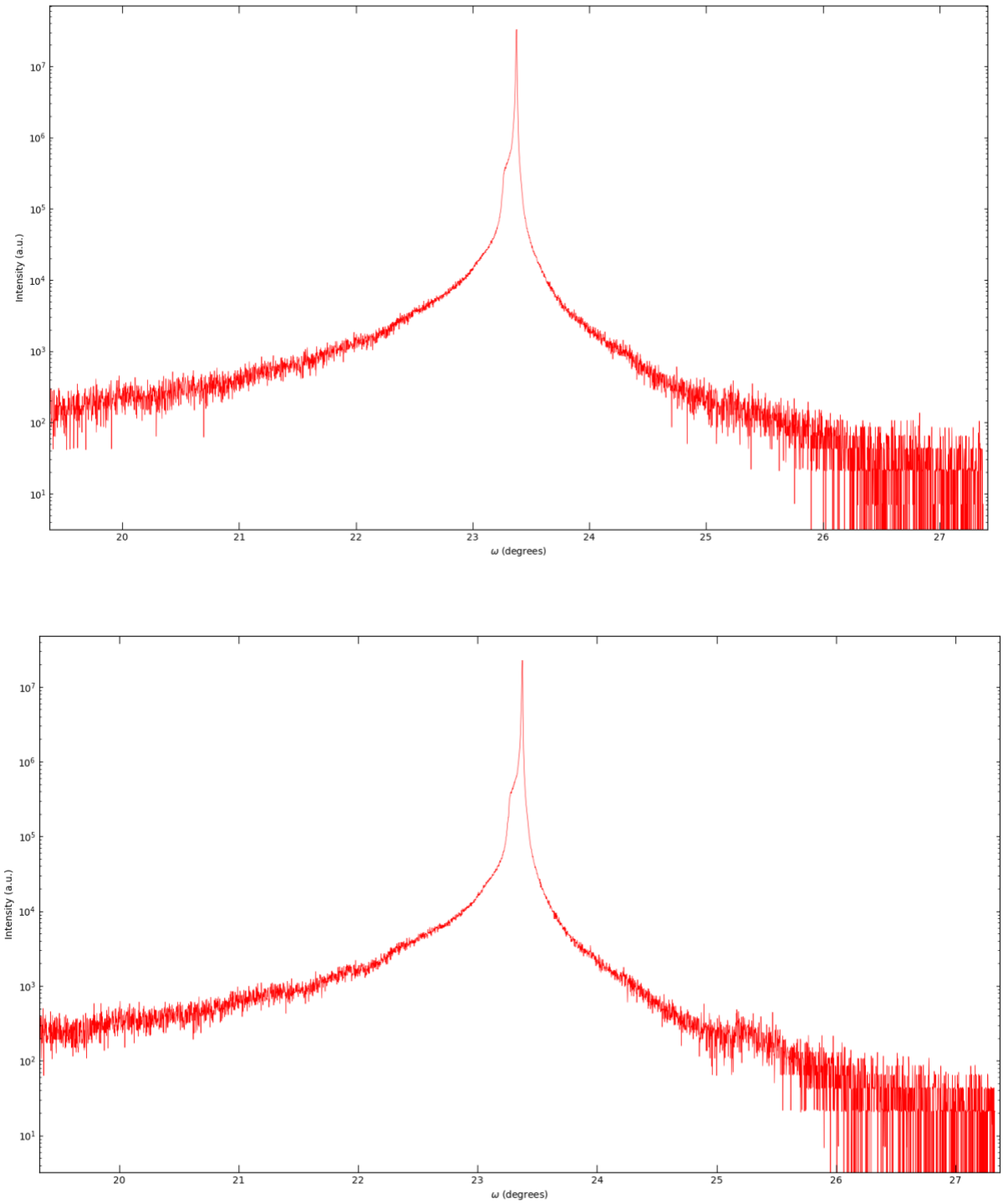

Figure A55: ω rocking curve of substrate (top) and film (bottom) of thin doped CSO sample grown at 100mTorr and 850°C on STO. $FWHM_{film} = 0.559°$

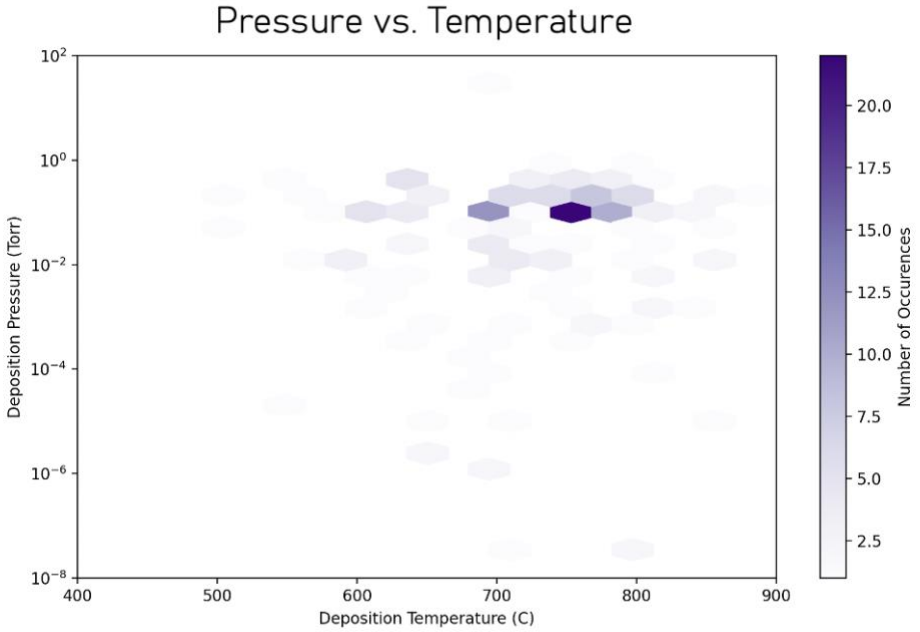

Figure A56: Deposition parameters of pressure vs. temperature of the various oxide systems found in Refs. [89-184]

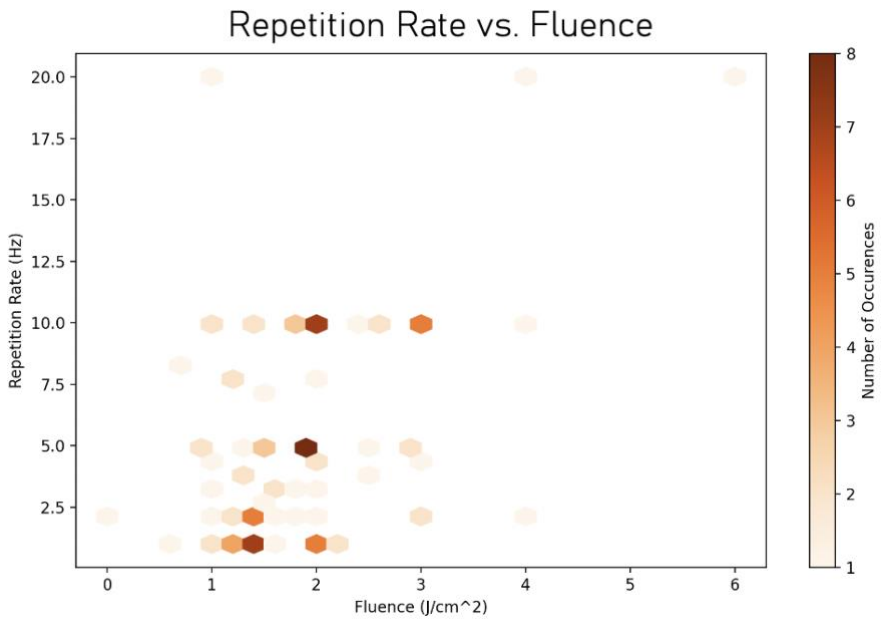

Figure A57: Deposition parameters of repetition rate vs. fluence of the various oxide systems found in Refs. [89-184]

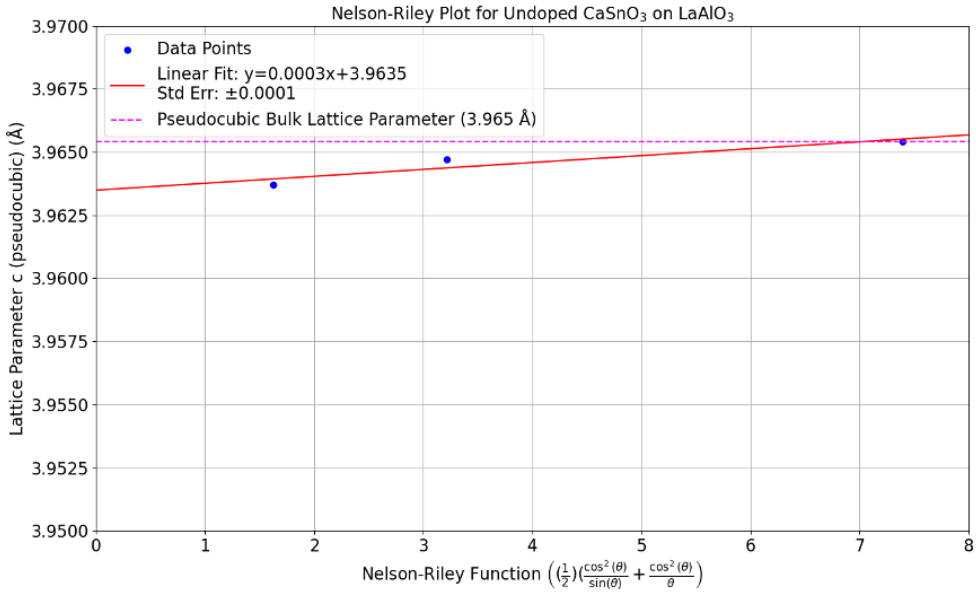

Figure A58: Lattice parameter plotted against Nelson-Riley function for the undoped $CaSnO_3$ film grown on LAO, indicating a lattice parameter of 3.9635 Å. The bulk constant 3.9635 Å is shown as the dotted magenta line.

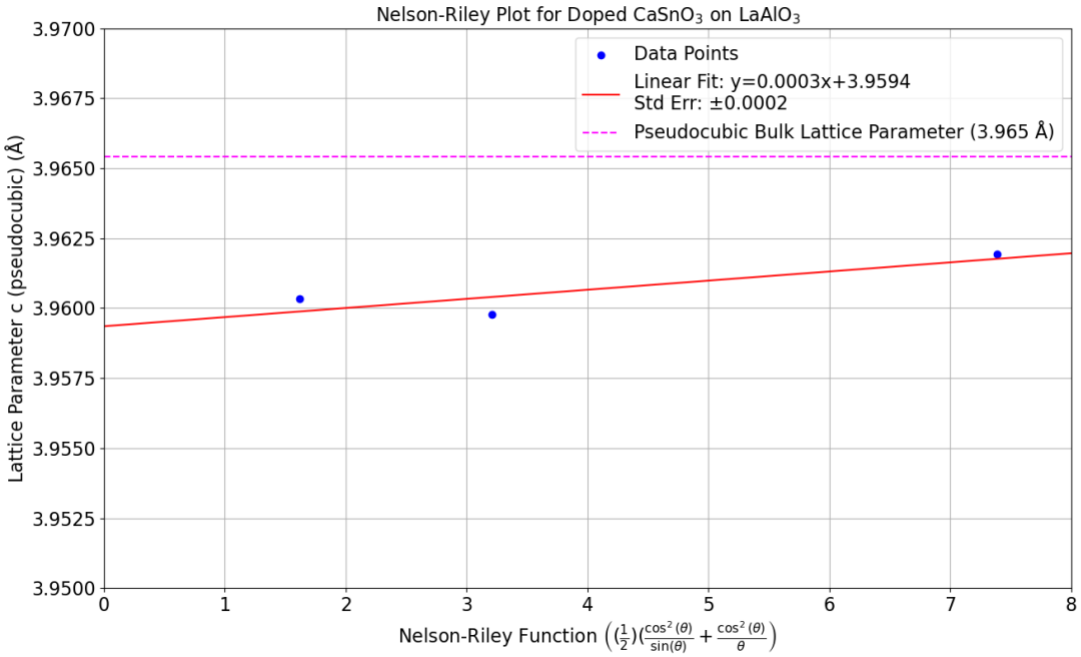

Figure A59: Lattice parameter plotted against Nelson-Riley function for the doped $CaSnO_3$ film grown on LAO, indicating a lattice parameter of 3.9594 Å. The bulk constant 3.9635 Å is shown as the dotted magenta line.

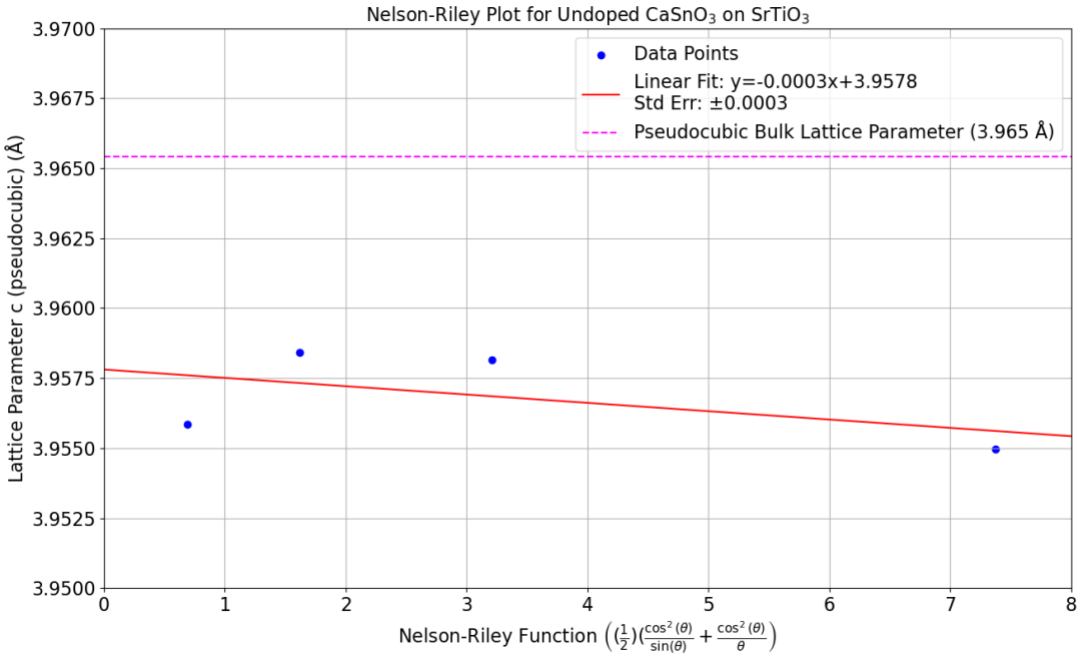

Figure A60: Lattice parameter plotted against Nelson-Riley function for the undoped $CaSnO_3$ film grown on STO, indicating a lattice parameter of 3.9578 Å. The bulk constant 3.9635 Å is shown as the dotted magenta line.

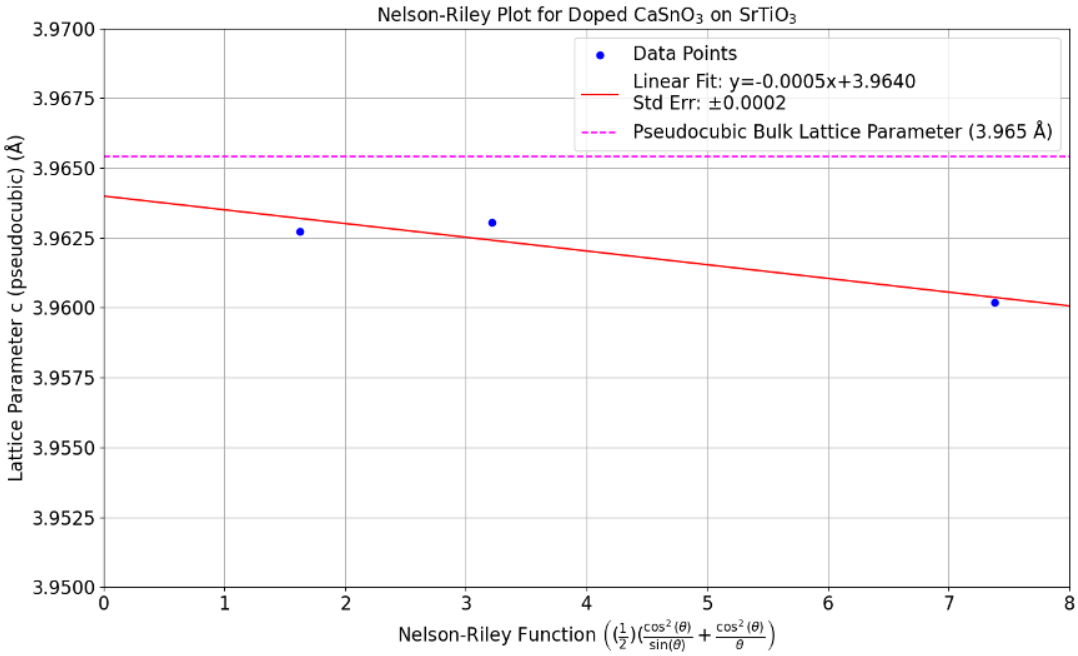

Figure A61: Lattice parameter plotted against Nelson-Riley function for the doped $CaSnO_3$ film grown on STO, indicating a lattice parameter of 3.9640 Å. The bulk constant 3.9635 Å is shown as the dotted magenta line.